From Ruby to Molecular Ruby: Excited State Understanding and Design

Katja Heinze* and Christoph Förster*

Department of Chemistry, Johannes Gutenberg University Mainz, Duesbergweg 10-14, 55128 Mainz, Germany

K.H.: katja.heinze@uni-mainz.de

C.F.: christoph.foerster@uni-mainz.de

ABSTRACT

The gemstone ruby, corundum (α-Al_2O_3)[1] with Al^{3+} ions partially substituted by Cr^{3+} ions (Al_2O_3:Cr^{3+}) possesses exceptional photophysical properties with an extremely long-lived (4270 μs) spin-flip phosphorescence at 694 nm with very high photoluminescence quantum yield (90%). The phosphorescent soluble molecular congener $[Cr(ddpd)_2]^{3+}$ called "*Molecular Ruby*", emitting at 738 and 775 nm also shows record values in the field of chromium(III) complexes in photoluminescence lifetime (1122 μs) and quantum yield (13.7%). The comparably lower photophysical parameters stress the huge challenge of designing high-performance photoluminescent *molecular* systems. This tutorial review discusses general design concepts of *Molecular Rubies*, which are transferable to other photoactive molecular complexes. An introductory theoretical frame is given, including crystal field, ligand field and molecular orbital theory of transition metal complexes, also highlighting photophysical processes in vertical (absorption and emission) and horizontal (internal conversion, intersystem crossing, inductive resonant energy transfer to high-energy oscillators) transitions. These challenges or disadvantages at first sight also include possibilities or levers to significantly tune specifically the photophysical properties and reactivity, such as emission energy and to enable applications in photocatalysis and sensing.

TABLE OF CONTENTS

I. INTRODUCTION

The prominent gemstone ruby, which is corundum (α-Al_2O_3)[1] with Al^{3+} ions partially substituted by Cr^{3+} ions (Al_2O_3:Cr^{3+}) [Fig. 1(a)], has inspired the design of photoactive transition metal complexes (TMCs), showing so-called spin-flip (SF) photoluminescence (PL) [Fig. 1(b)].[2] The chromium(III) center is the color center in this material. Spin-allowed excitation of the ground state (GS) of the chromium(III) ion ($^4A_{2g}$) to the interconfigurational ligand field excited state (ES, $^4T_{2g}$) of ruby at 551 nm results in the famous strong ruby SF phosphorescence at 694 nm from the lowest-energy intraconfigurational ligand field excited state (^2E_g) with an extremely long PL lifetime $\tau = 4270$ µs and a high PL quantum yield $\Phi_{em} = 90\%$ [Fig. 1(c), 1(d)].[3–7] The term 'spin-flip' specifies that the GS and ES electron configurations are the same, here $(t_{2g})^3$, but with one electron's spin formally flipped. This is pictorially illustrated by the microstates of the $^4A_{2g}$ and ^2E_g states [Fig. 1(d)]. *Hund*'s rule[8] can be invoked to qualitatively understand the destabilization of the ^2E_g over the $^4A_{2g}$ ground state. A small trigonal deviation in α-Al_2O_3 from octahedral (O_h) symmetry of the Cr^{3+} sites combined with spin-orbit coupling with concomitant splitting of the electronic states into two pairs of *Kramers* doublets splits the ruby SF emission band into two very sharp bands at 694.3 and 692.9 nm (R_1, R_2), respectively [Fig. 1(a), 1(c)].[3–6] The PL lifetime $\tau = 4270$ µs is hence the averaged lifetime of the thermally equilibrated population of the ^2E_g sublevels.[4,6] As 90% of the absorbed photons are converted to emitted photons of lower energy, nonradiative loss processes are practically negligible in this solid-state material. Indeed, population transfer from the initially excited $^4T_{2g}$ ligand field state to the ^2E_g states occurs efficiently via direct $^4T_{2g} \rightarrow {}^2E_g$ intersystem crossing (ISC, k_{ISC}) or via an indirect path (k_{ISC}') transiently populating the higher-energy $^2T_{1g}$ state followed by internal conversion (IC, k_{IC}') and vibrational relaxation (VR) processes within the doublet manifold [Fig. 1(d)]. While VR leads to energy dissipation, IC and ISC processes are (nonradiative) isoenergetic hopping processes between electronic states of identical and different spin multiplicities, respectively.[9,10] In this solid-state material ruby, all these ISC and IC processes are very efficient, while loss channels appear inefficient, resulting in the observed very high PL quantum yield.

Molecular chromium(III) complexes can show SF emission as well, however typically with only very poor PL quantum yields below 2% ($[Cr(phen)_2]^{3+}$) [Scheme 1, Table S1, supplementary material].[11–16] A breakthrough in molecular SF emitters was achieved, when our group reported the polypyridyl chromium(III) complex $[Cr(ddpd)_2]^{3+}$ (ddpd = *N*^{2},*N*^{6}-dimethyl-*N*^{2},*N*^{6}-di(pyridin-2-yl)pyridine-2,6-diamine) in 2015 [Fig. 1(b)]. $[Cr(ddpd)_2]^{3+}$ possesses an exceptionally intense sharp dual SF phosphorescence emission in the near-infrared (NIR) spectral region peaking at 738 ($^2E_g \rightarrow {}^4A_{2g}$) and 775 nm ($^2T_{1g} \rightarrow {}^4A_{2g}$), respectively. PL lifetimes $\tau = 898$ µs and 1136 µs and PL quantum yields of $\Phi_{em} = 11.0\%$ and 13.7% in aqueous and acetonitrile solution, respectively, mark record values for open-shell 3d TMCs in solution at room temperature [Fig. 1(c), Table S1, supplementary material].[2,17,18] Hence, inspired by the photophysical properties cognate to ruby, $[Cr(ddpd)_2]^{3+}$ was denominated "*Molecular Ruby*".[19–21] However decisive differences exist, despite the phenomenologically similar photophysical properties of ruby and the *Molecular Ruby*. These are predominantly based on the differences in the chemical environment, particularly the imposed ligand field strengths, the donor properties of the coordinating ligands, the site symmetry, the coordination sphere rigidity and the absence (ruby) or presence (*Molecular Ruby*) of high-energy oscillators in the vicinity of the chromium center. For example, the emission band width of ruby is much smaller than for *Molecular Ruby* [Fig. 1(c)], the emission energy of the *Molecular Ruby* is lower than that of ruby [Fig. 1(c)],[2,7] the emission intensity of the *Molecular Ruby* significantly increases at lower temperature[22] in contrast to that of ruby,[23] the emission energy shifts with increasing pressure much stronger in the *Molecular Ruby*[7] than in ruby[24–27] and the lowest-energy emissive state of $[Cr(ddpd)_2]^{3+}$ derives from a $^2T_{1g}$ microstate in contrast to the commonly accepted doublet state order for chromium(III) ions in (pseudo-)octahedral environments such as in ruby [Fig. 1(d)].[21,28] All these decisive experimental observations will be addressed and contextualized in this review to arrive at an understanding of the unique photophysical properties of *Molecular Ruby*-type complexes.

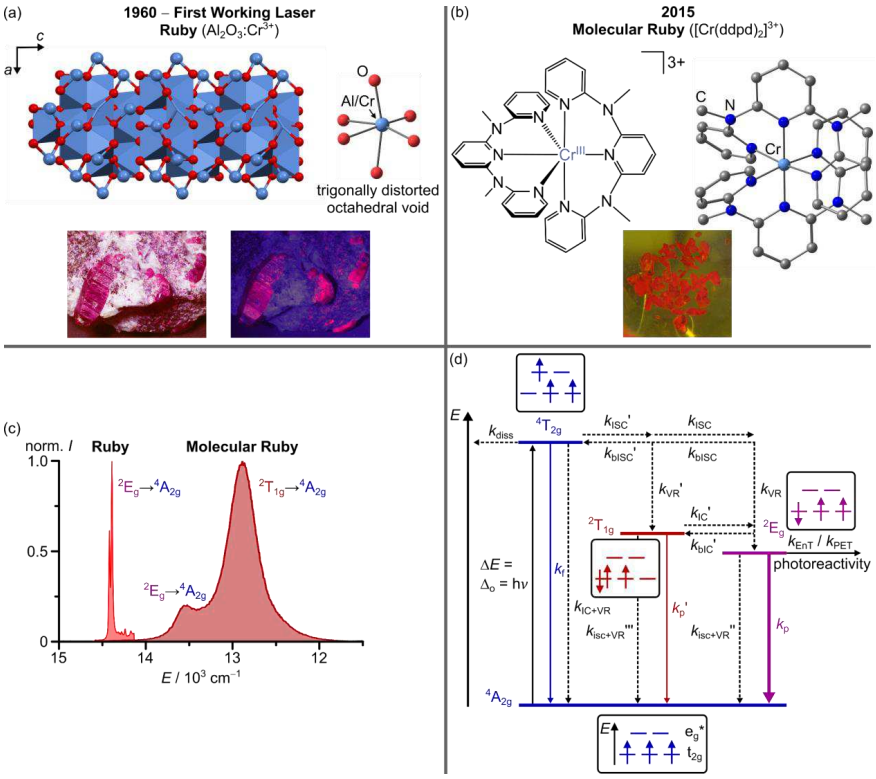

FIG. 1. (a) Excerpt of the corundum (α-Al_2O_3 space group $R\bar{3}c$) solid-state structure (view along the *b* axis) with filled octahedral voids and the trigonally distorted octahedral coordination geometry of the Al^{3+} and Cr^{3+} cations in the octahedral void (right), photographs of a mineral containing ruby crystallites (left), which show red phosphorescence under UV light (right). (b) Molecular structure of the *Molecular Ruby* $[Cr(ddpd)_2]^{3+}$ (hydrogen atoms are omitted) with a photograph of orange crystals of $[Cr(ddpd)_2][BF_4]_3$ in a yellow CH_3CN solution of the complex. Photograph reproduced with permission from Angew. Chem. Int. Ed. 54, 11572 (2015). Copyright 2015, John Wiley and Sons. (c) Phosphorescence spectra of ruby and the *Molecular Ruby* $[Cr(ddpd)_2]^{3+}$ in acetonitrile. (d) Simplified energy diagram showing quartet and doublet *Franck-Condon* (*FC*) state energies with exemplary microstates, illustrating relaxation pathways in a d^3-TMC of O_h symmetry after photoexcitation. Rate constants for various processes are indicated: ISC, k_{ISC}; back-ISC, k_{bISC}; internal conversion, k_{IC}; back-IC, k_{bIC}; fluorescence, k_f; phosphorescence, k_p; vibrational relaxation, k_{VR}; photoreactivity in energy transfer, k_{EnT} and photoinduced electron transfer, k_{PET}.

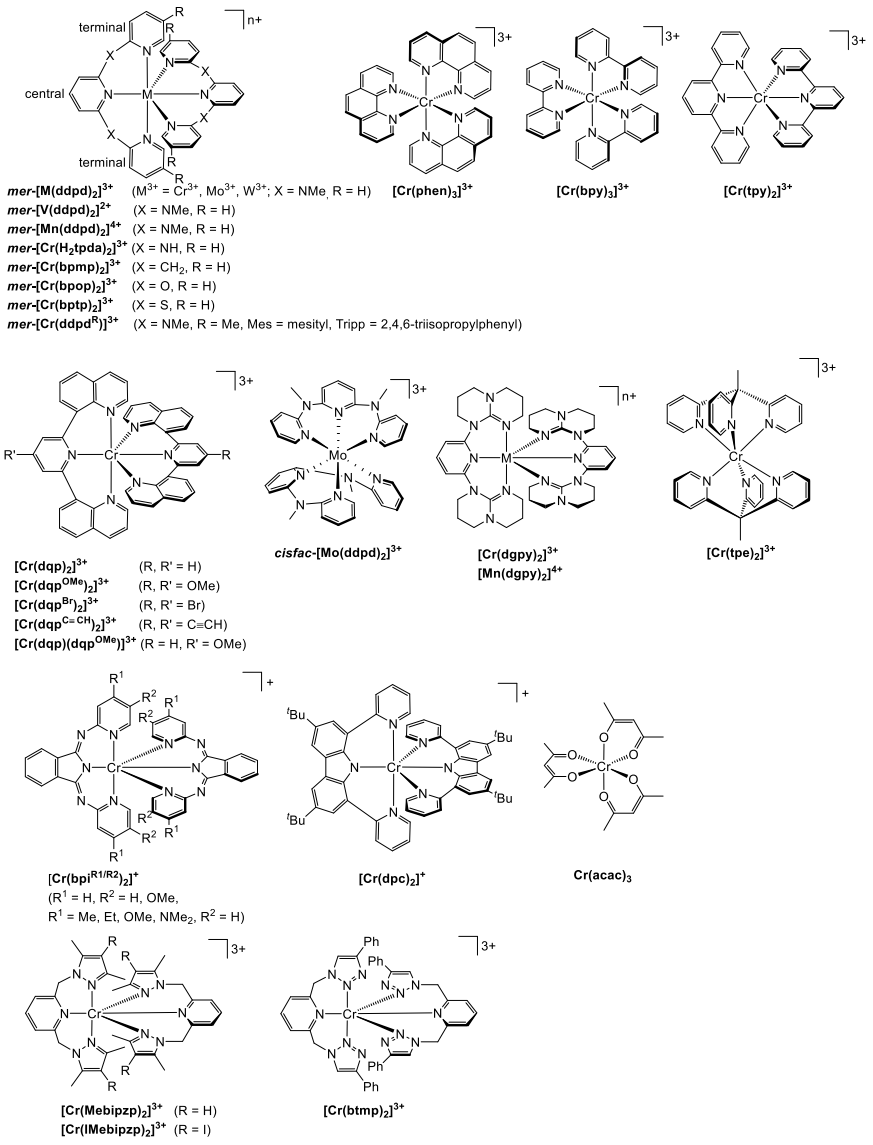

SCHEME 1. Molecular structures of pseudo-octahedral TMCs with specification of central and terminal pyridine donors of the meridional tripyridine ligands derived from ddpd.

Several reviews about the phenomenological photophysical properties and numerous applications of *Molecular Ruby*-type complexes are available.[16,19,21,28–34] Rather than giving a further updated overview over chromium(III) complex derivatives and specific applications of *Molecular Ruby*-type systems, this tutorial and pedagogical review aims to trace the way to develop and understand a molecular SF chromophore with photophysical properties in fluid solution akin to the solid-state material ruby. Compared to molecular complexes of

isoelectronic transition metal ions of the neighboring elements V^{2+}/Mn^{4+} and Mo^{3+}/W^{3+}, chromium(III) seems to mark the sweet spot for strong, long-lived SF PL and high (photo)chemical stability. Consequently, we will focus on d^3 systems, in particular pseudo-octahedral chromium(III) complexes. Although the NIR PL quantum yield of the *Molecular Ruby* is very high for a molecular chromophore ($\Phi_{em} = 13.7\%$)[18] [Table S1, supplementary material], it is still inferior to that of ruby ($\Phi = 90\%$)[5] suggesting additional loss processes in the flexible molecular chromophore in fluid solution [Fig. 1(d)]. Such loss channels comprise unimolecular nonradiative ES→GS deactivation processes (k_{IC+VR}, k_{ISC+VR}'', k_{ISC+VR}''') and $^2T_{1g}/^2E \rightarrow {}^4T_{2g}$ bISC (k_{bISC}, k_{bISC}'), intramolecular processes (ligand dissociation, k_{diss} and energy transfer EnT, k_{EnT}) and bimolecular photoreactivity (energy transfer EnT, k_{EnT} and photoinduced electron transfer PET, k_{PET}) [Fig. 1(d)].[9,10,16,28] While ruby cannot engage in bimolecular reactions, the bimolecular reactivity of *Molecular Ruby*-type systems in fluid solution enables applications such as sensing,[7,22,35,36] photo(redox) catalysis[17,37–43] and triplet-triplet annihilation upconversion[44] unattainable for ruby.[28,31] Further applications are in NIR light-emitting electrochemical cells[45] or organic light-emitting diodes.[46] In principle, absorption energy, absorption coefficient, emission energy, ES lifetimes and quantum yields can be tuned by ligand design[20,47–58] in the molecular systems, which is much more challenging for solid-state systems,[59] setting *Molecular Ruby*-type systems apart from ruby itself.

This tutorial review starts with a section on the relevant energy levels of the d^3 electron configuration as seen from crystal and ligand field (LF, CF) theory. The view on the LF states is supplemented by molecular orbital (MO) theory that also includes charge transfer (CT) ESs. This section will make use of quantum chemical methods, namely (time-dependent) density functional theory ((TD)DFT) and multi-reference complete-active space self-consistent field (CASSCF) calculations, to describe and illustrate the energetics of LF and CT ESs arising from the d^3 electron configuration of series of isoelectronic pseudo-octahedral complexes of V^{2+}, Cr^{3+}, Mn^{4+} and Cr^{3+}, Mo^{3+}, W^{3+} central ions. This *Franck-Condon* (*FC*) picture of the electronic states is then refined to adiabatic potential energy surfaces (PESs) along significant excited state distortions, especially the *Jahn-Teller* (*JT*) distortion of interconfigurational LF states. These PESs form the basis for the discussion of relevant radiative (vertical), nonradiative (horizontal) and thermally activated photophysical processes in general and in complexes with d^3 electron configuration in particular. The two major loss channels in molecular chromium(III) complexes are discussed in the frameworks of PES crossings invoked by excited state distortions and of the inductive-resonant mechanism (IRM) of nonradiative transitions, which involve high-energy oscillators close to the chromium center. With these pieces of information put together covering the entire excited state dynamics from absorption of a photon to the recovery of the ground state, the reader will be able to comprehend the unique photophysical properties of *Molecular Ruby*-type systems with respect to other isoelectronic d^3 metal complexes and the solid material ruby.

II. ENERGY LEVELS OF THE d^3 CONFIGURATION IN THE CRYSTAL FIELD, LIGAND FIELD AND MOLECULAR ORBITAL THEORY MODELS (FRANCK-CONDON PICTURE)

Both CF theory and LF theory are topics of classic[60–63] and modern[64–67] textbooks of inorganic and coordination chemistry. CF theory, as basis of the more elaborate LF theory, deals solely with the metal d orbitals and the respective d electrons in the one-electron approximation, while the ligands are simplified as negative point-charges. In a CF of O_h symmetry, the degeneracy of the five d orbitals is partially lifted forming a set of triply degenerate t_{2g} (d_{xy}, d_{xz}, d_{yz}) and a set of doubly degenerate e_g (d_{x2-y2}, d_{z2}) orbitals [Fig. 2(a)]. The latter orbitals are often highlighted with an asterisk * (e_g*), implying antibonding character, a notation, which stems from MO theory (vide infra). The index 'g' denotes a symmetric behavior towards the inversion center, which applies to all pure d orbitals. The energy difference between the t_{2g} and e_g* orbital sets is called crystal field splitting $\Delta_o = 10\ Dq$ [Fig. 2(a)]. In this purely electrostatic CF model, the product *Dq* depends on the radial part of the d electron wavefunctions, the charges of the ligands and metal centers and the metal-ligand distances.

While the CF model suffices to the interpret the electronic absorption spectra of TMCs with d^1 and d^9 electron configurations, d electron-electron interaction depends on the relative orbital occupation for systems with more than one d electron (or one d hole). For example, this holds for the d^3 electron configuration $(t_{2g})^3(e_g*)^0$ of the Cr^{3+} ion. Spin-allowed interconfigurational electronic transitions in the d^3 case result in the $(t_{2g})^2(e_g*)^1$ electron configuration [Fig. 2(a)]. However, these electronic transitions with $\Delta E = h\nu$ involving six microstates in total cannot be described by the CF splitting Δ_o alone as the energies also depend on the electron-electron repulsion in the respective microstates. To gain a qualitative pictorial understanding of this observation, we inspect two

transitions involving the d_{xy} orbital of the t_{2g} set and the two e_g* orbitals, namely the $d_{xy}\rightarrow d_{x2-y2}$ and $d_{xy}\rightarrow d_{z2}$ transitions [Fig. 2(a)].[67] For the $d_{xy}\rightarrow d_{x2-y2}$ transition, the electron density is merely redistributed in the *xy* plane by a 45° rotation compared to the GS with $(t_{2g})^3$ electron configuration as illustrated by the difference electron density plot $\rho(d_{x2-y2})-\rho(d_{xy})$ [Fig. 2(b)]. On the other hand, the $d_{xy}\rightarrow d_{z2}$ excitation shifts electron density from the *xy* plane to the electron-rich *z* direction with singly occupied d_{xz} and d_{yz} orbitals already pointing in this direction as the difference electron density plot $\rho(d_{z2})-\rho(d_{xy})$ illustrates [Fig. 2(b)]. Consequently, the $(d_{xz})^1(d_{yz})^1(d_{x2-y2})^1$ microstate is lower in energy than the $(d_{xz})^1(d_{yz})^1(d_{z2})^1$ microstate due to differences in the d interelectronic repulsion. In this many-electron picture of the $(t_{2g})^2(e_g*)^1$ electron configuration, three microstates belong to triply orbitally-degenerate lower- and higher-energy states each, denoted by their *Mulliken* symbols $^4T_{2g}$ and $^4T_{1g}$ with the left superscript giving the (quartet) spin multiplicity M ($M = 2S + 1$, with the total spin $S = 3/2$). Experimentally, two absorption bands are thus observed for the spin-allowed one-electron transitions $^4A_{2g}\rightarrow{}^4T_{2g}$ and $^4A_{2g}\rightarrow{}^4T_{1g}$ at energies $\Delta_1 E$ and $\Delta_2 E$, respectively [Fig. 2(a)].

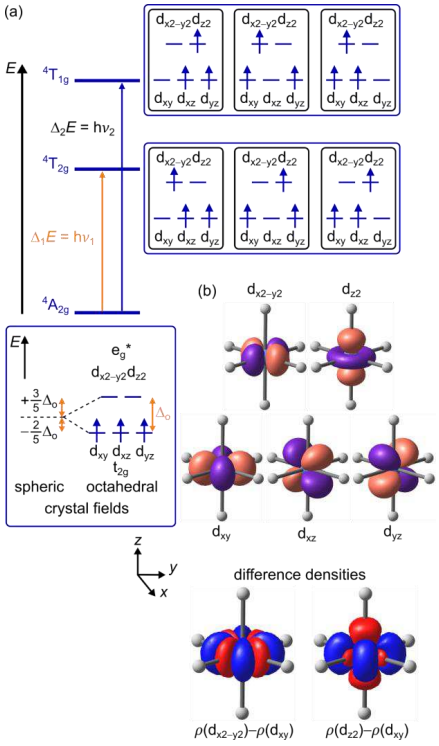

FIG. 2. (a) Schematic energy level diagram for an octahedral d^3 TMC (O_h) with microstates for spin-allowed one electron transitions ($^4A_{2g}\rightarrow{}^4T_{2g}$ and $^4A_{2g}\rightarrow{}^4T_{1g}$) and (b) CF orbitals (isosurface value 0.1 a.u.) and selected difference densities ρ (isosurface value 0.02 a.u.; blue = electron density depletion, red = electron density gain) to highlight the electron redistribution in two LF transitions.

The refinement of CF theory leads to LF theory considering both the LF strength *and* the d interelectronic interaction in a perturbative approach. The *strong field approximation* assumes a comparably strong ligand field, which is perturbed by a weaker d electron-electron interaction. Hence, CF theory represents a limiting case of the *strong field approximation* with a vanishing d electron interaction. On the other side, the *weak field approximation* starts from free ion terms, i.e. in the absence of a crystal field. These free ion terms are obtained from the *Russel-Saunders* coupling scheme as a combination of the total angular momentum *L* with the total spin *S* implying a strong d electron interaction. Then the free ion terms are perturbed by a weak ligand field. The d

electron ion term energies are parametrized by the so-called *Racah* parameters A, B and C. Table 1 summarizes the ion term energies for a d^3 ion [Eq. (1), (2)]. While parameter A represents a general increase in term energy, B and C can be understood as interelectronic repulsion parameters [Table 1].[60,61,66]

TABLE 1. Selected free ion term energies and ligand field term energies described by *Racah* parameters A, B and C and ligand field splitting $\Delta_o = 10\ D_q$ for d^3 ions.[61]

free ion term energies	ligand field term energies
$E(^4F) = 3A - 15B$ (1)	$E(^4T_{2g}) - E(^4A_{2g}) = \Delta_o$ (3)
	$E(^4T_{1g}) - E(^4A_{2g}) = 1.5\Delta_o + 7.5B - 0.5\sqrt{225B^2 + {\Delta_o}^2 - 18\Delta_o B}$ (4)
$E(^2G) = 3A - 11B + 3C$ (2)	$E(^2E_g) - E(^4A_{2g}) = 9B + 3C - 50\frac{B^2}{\Delta_o}$ (5)
	$E(^2T_{1g}) - E(^4A_{2g}) = 9B + 3C - 24\frac{B^2}{\Delta_o}$ (6)
	$E(^2T_{2g}) - E(^4A_{2g}) = 15B + 5C - 176\frac{B^2}{\Delta_o}$ (7)

They are introduced as mathematical tool to describe the (unknown) two-electron Coulomb and exchange integrals of the radial part of *Slater*-type wavefunctions representing the d electrons. Energies of ESs with identical spin multiplicity are calculated from the parameters A and B only. ESs of different spin multiplicity require the additional parameter C, which considers the vanishing exchange integrals between spin orbitals of different spin. Combination of these mathematical approaches leads to the so-called *Tanabe-Sugano* diagrams. These diagrams display the energies and term symbols of LF states in O_h notation originating from the respective free ion d electron configurations. *Tanabe-Sugano* diagrams depict the LF term energies E versus the LF splitting Δ_o, both given in the unit of the *Racah* parameter B at a fixed C/B ratio, often with $C/B \approx 4$. This ratio originates from the observation that C/B is assumed to be nearly constant with values between 4–5 for all central ions and a ratio of $C/B = 3.97$ is almost independent on the nuclear charge of *Slater*-type wavefunctions [Table 2].[61,68] Fig. 3 shows the *Tanabe-Sugano* diagram for the d^3 electron configuration with quartet and doublet terms shown in blue and red/purple, respectively.[68,69] Exemplary relevant microstates are depicted as well.

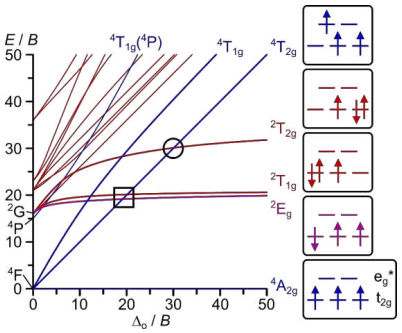

FIG. 3. *Tanabe-Sugano* diagram for octahedral TMCs (O_h point group notation) with d^3 electron configuration ($C/B = 4$). Quartet/doublet ES crossing points are highlighted with a square and a circle, respectively, and exemplary microstates of relevant LF states are shown on the right side of the diagram.

TABLE 2. Free ion *Racah* parameters B_{ion} and C_{ion} for selected ions in cm^{-1}.[61]

	ion	B_{ion}	C_{ion}	C_{ion}/B_{ion}
$3d^3$	Sc^+	480	n.g.[a]	-
	V^{2+}	766	2855	3.72
	Cr^{3+}	918	3850	4.19
	Mn^{4+}	1064	(4919)[68]	4.62
$4d^3$	Mo^{3+}	610	n.g.[a]	-
[a] not given				

Energies of interconfigurational states, such as $^4T_{2g}$ and $^4T_{1g}$ states, scale with the ligand field splitting Δ_o, [Eq. (3), (4)], while the intraconfigurational states of the d^3 configuration ^2E_g, $^2T_{1g}$ and $^2T_{2g}$ depend only weakly on the ligand field splitting Δ_o [Table 1, Eq. (5)–(7), Fig. 3].[61] This different behavior of intra- and interconfigurational terms leads to crossing points of the lowest-energy quartet state $^4T_{2g}$ with the lowest-energy doublet states ^2E_g, $^2T_{1g}$ and $^2T_{2g}$ at distinct ligand field splittings Δ_o as indicated in the *Tanabe-Sugano* diagram in Fig. 3 by a square and a circle, respectively. Potential energy curves corresponding to electronic states of the same irreducible representation and spin multiplicity cannot cross (non-crossing rule). This avoided crossing leads to term energies with nonlinear behavior with respect to Δ_o, as can be seen, for example, for the $^4T_{1g}$ states of the d^3 electron configuration [Table 1, Eq. (4), Fig. 3]. Similarly, the ^2E_g, $^2T_{1g}$ and $^2T_{2g}$ states of the d^3 electron configuration show nonlinear behavior due to avoided crossings [Table 1, Eq. (5)–(7), Fig. 3]. In summary, LF theory describes term energies of TMCs by the *Racah* parameters A, B and C and the LF splitting Δ_o.[61,68,69] When only energy differences are required, the A parameter vanishes [Table 1], and when a fixed C/B ratio is assumed, term energies can be described by the two parameters B and Δ_o only [Table 1].

As Δ_o and B influence the LF term energies, we will inspect these in more detail, starting with Δ_o. The LF splitting Δ_o empirically depends on the coordinated ligands (spectrochemical series of the ligands) and the central ions (spectrochemical series of the central ions) as summarized in Table 3. The order of ligands is largely independent of the central ion and analogously the order of the metal ions is largely independent of the ligand. Minor deviations from the general series given in Table 3 are, however, possible.[60–67] In some cases, the spectrochemical series of the ligands seems to contradict the purely electrostatic model assumed in CF/LF theory. For example, the charged, small fluorido ligand should induce a much stronger LF than the neutral CO ligand from an electrostatic point of view. This apparent contradiction is resolved by MO theory, considering σ and π bonding effects of the ligands (vide infra), and not merely a point charge of the ligands. π donating ligands (e.g. Cl^-, NO_2^-) are found on the left side, pure σ donor ligands (e.g. CH_3CN, NH_3, en) in the center and π accepting ligands (e.g. CN^-, CO) on the right end of this series. Pyridines and especially conjugated polypyridines are medium to strong ligands like aliphatic amines [Table 3(a)].

TABLE 3. Empirical spectrochemical series of the ligands (a) and central ions (b).[61,66,67] Donor atoms of ambidentate ligands are underlined. Metal ions with d^3 electron configurations relevant to this review are highlighted in bold.

(a)	$I^- < Br^- < \underline{S}CN^- < Cl^- < \underline{N}O_2^- < N^{3-} < F^-$ < urea < OH^- < ox^{2-} < O^{2-} < H_2O < $\underline{N}CS^-$ < CH_3CN < py ≈ NH_3 < en < bpy ≈ phen < $\underline{N}O_2^-$ < PPh_3 < $\underline{C}N^-$ < CO
(b)	$Mn^{2+} < Ni^{2+} < Co^{2+} < Fe^{2+} <$ **V^{2+} ($3d^3$)** < $Fe^{3+} <$ **Cr^{3+} ($3d^3$)** < $V^{3+} < Co^{3+} < Ru^{2+} <$ **Mn^{4+} ($3d^3$)** < **Mo^{3+} ($4d^3$)** < $Rh^{3+} < Ru^{3+} < Pd^{4+} < Ir^{3+} < Pt^{4+}$

The LF splitting Δ_o increases with the oxidation state of the central ion (e.g. $Mn^{2+/4+}$, $Co^{2+/3+}$, $Fe^{2+/3+}$, $V^{2+/3+}$) and with increasing ionic charge within an isoelectronic series (e.g. the $3d^3$ ions V^{2+}, Cr^{3+}, Mn^{4+}) [Table 3(b)]. These trends can be explained in the framework of CF theory: decreasing ionic radii leads to shorter metal-ligand distances *d* strongly increasing the LF splitting as Δ_o scales with d^{-5}.[60,65] Thanks to the smaller lattice parameter of Al_2O_3,[1] defined by the smaller ionic radius of Al^{3+} (67.5 pm), the Cr–O distances in ruby, for example, are shorter than in isostructural Cr_2O_3 itself with the larger Cr^{3+} ion (75.5 pm).[70] The large Cr^{3+} ion forced into the small octahedral void of corundum leads to a larger ligand field splitting and thus a blue-shifted $^4A_{2g} \rightarrow {}^4T_{2g}$ absorption band, with Cr_2O_3 and ruby being of green and red color, respectively, despite the identical $[CrO_6]$ coordination environment.[6,71,72] Similarly, hydrostatic pressure compresses the Cr–O bonds of $[Cr(urea)_6]^{3+}$ and the Cr–N bonds of the *Molecular Ruby*, which increases the LF splittings in these complexes.[36,73]

Within a group triad (e.g. the d^6 ions Co^{3+}, Rh^{3+}, Ir^{3+}), the ligand field splitting Δ_o increases as well [Table 3(b)]. This effect cannot be understood by a purely electrostatic model but requires metal-ligand bonding as described by MO theory (vide infra). While the 3d orbitals are very compact, the 4d and 5d orbitals are much more expanded leading to a better metal-ligand orbital overlap and thus a larger Δ_o at constant M–L distance.[60,65,66] The so-called *primogenic effect* describes the small radial expansion of the first wavefunctions without radial nodes (1s, 2p, 3d and 4f).[74,75] The radial nodal structure and contraction of the 3d orbitals, for example, leads to an increased *Pauli* repulsion of the filled 2s and 2p orbitals of the 3d TM central ion with the occupied ligand donor orbitals. This results in comparably longer metal-ligand bonds with a smaller overlap of the metal d orbitals with the ligand orbitals. Consequently, σ antibonding e_g* and weakly bonding t_{2g} orbitals are lower and higher in

energy, respectively, furnishing a smaller LF splitting Δ_o for 3d TMCs. The small LF splitting intrinsic to 3d TMCs can lead to high-spin configurations with weak-field ligands, while the low-spin configuration prevails in 4d and 5d TMCs essentially independent from the ligand strenghs. Excited states of 3d TMs with higher spin multiplicities are also lower in energy as compared to those of heavier 4d/5d TMs.

Beyond ligand field splitting Δ_o, the *Racah* parameters B and C modulate LF state energies [Tables 1, 2].[61] Both parameters increase with the oxidation state (e.g. $V^{2+} < V^{3+}$) and with the ionic charge for isoelectronic ions (e.g. $V^{2+} < Cr^{3+} < Mn^{4+}$). These trends can be traced back to d orbital contraction with increasing charge and consequently a stronger d electron repulsion. Apart from these purely electrostatic effects, metal-ligand bonding affects B and C as well. With increasing metal-ligand covalence, the largely metal-centered t_{2g} and e_g* orbitals acquire contributions from ligand-centered orbitals. Hence, d electrons can partially delocalize onto the ligands. This leads to a radial expansion of the molecular orbitals, or in other words, an expansion of the electron clouds. The "average" distance between d electrons increases, decreasing the d interelectronic repulsion. This effect is termed *nephelauxetic effect* (cloud-expansion effect).[76] Compared to the free ion values B_{ion} and C_{ion}, the *Racah* parameters B and C of TMCs are lowered by this cloud-expansion. *Nephelauxetic effects* of ligands and central ions are arranged in the empirical *nephelauxetic series of ligands and central ions*,[76] respectively [Table 4].[61,66] The *nephelauxetic parameter* β gives a measure for the covalency of the metal-ligand bonds [Eq. (8)]. A smaller value of β indicates a dominating covalent character of the metal-ligand bond, while a larger value describes a more ionic character.[60–67,77] According to the empirical *nephelauxetic series*, β follows the decreasing electronegativity of the donor atom of the ligands ($F^- > H_2O > NH_3 > CN^-$) [Table 4(a)], the increasing charge of isoelectronic central ions in one period (e.g. $V^{2+} > Cr^{3+} > Mn^{4+}$) and increases within one group ($Cr^{3+} < Mo^{3+}$) [Table 4(b)].[61,66,76] The LF parameters of TMCs can be experimentally determined from the energies of the MC transitions in electronic absorption spectra. For d^3 TMCs, Δ_o is directly obtained from the energy of the $^4A_{2g} \rightarrow {}^4T_{2g}$ transition [Eq. (3)]. B can be obtained from the energy of the $^4A_{2g} \rightarrow {}^4T_{1g}$ transition [Eq. (4)] with the help of mathematical programs or directly from the energy differences of the $^4A_{2g} \rightarrow {}^2E_g$ and $^4A_{2g} \rightarrow {}^2T_{1g}$ transitions [Eq. (5), (6)]. With the knowledge of Δ_o and B, C can be extracted from the ^2E_g state energy [Eq. (5), Tables 1,[61] 5[50,77–82]].

$$\beta = \frac{B}{B_{ion}} \quad (8)$$

TABLE 4. Empirical *nephelauxetic series* of ligands (a) and central ions (b) ordered with decreasing β (increasing *nephelauxetic effect*).[61,66] Donor atoms of ambidentate ligands are underlined. Metal ions with d^3 electron configuration relevant to this review are given in bold.

(a)	$F^- > H_2O >$ urea $> NH_3 >$ en $>$ ox$^{2-} >$ N̲CS$^- > Cl^- > CN^- > Br^- > I^-$
(b)	$Mn^{2+} \approx$ **V^{2+} ($3d^3$)** $> Ni^{2+} \approx Co^{2+} >$ **Mo^{3+} ($4d^3$)** $>$ **Cr^{3+} ($3d^3$)** $> Fe^{3+} > Ir^{3+} \approx Rh^{3+} > Co^{3+} >$ **Mn^{4+} ($3d^3$)** $\approx Pt^{4+}$

The *nephelauxetic* shift for C is larger as for B with $\Delta C > \Delta B$ with C being more sensitive to changes in metal-ligand covalency.[83] In principle, the ratio Δ_o/B, corresponding to the unit of the *x*-axis in *Tanabe-Sugano* diagrams, enables a comparative classification of TMCs with the help of the diagrams. Importantly, this only holds for TMCs with similar C parameters. However, as C/B ratios can strongly differ, as exemplary shown in the series of selected d^3 TMCs [Table 5, Scheme 1],[50,77–82] the *nephelauxetic parameter* β alone might be insufficient without the parameter C to predict SF energies ($^2E_g/^2T_{1g}$) of chromium(III) complexes [Table 1]. Nevertheless, $[CrF_6]^{3-}$ possesses a weak LF splitting placing the $^4T_{2g}$ state below the ^2E_g state, i.e. to the left side of the first quartet/doublet crossing point $^4T_{2g}/^2E_g$ in the *Tanabe-Sugano* diagram [Table 5, Fig. 3, square], while $[Cr(CN)_6]^{3-}$ possesses a very strong LF splitting placing the $^4T_{2g}$ state even above the $^2T_{2g}$ state, i.e. to the right side of the second quartet/doublet crossing point $^4T_{2g}/^2T_{2g}$ in the *Tanabe-Sugano* diagram [Table 5, Fig. 3, circle]. The LF splittings of $[Cr(NH_3)_6]^{3+}$ and $[Cr(tpy)_2]^{3+}$ are medium strong placing these complexes above the first quartet/doublet crossing point $^4T_{2g}/^2E_g$ in the *Tanabe-Sugano* diagram, while $[Cr(bpy)_3]^{3+}$ and $[Cr(ddpd)_2]^{3+}$ can be classified as TMCs with very strong ligand field splittings placing these complexes close to the second quartet/doublet crossing point $^4T_{2g}/^2T_{2g}$ in the *Tanabe-Sugano* diagram [Table 5, Fig. 3, Scheme 1]. Although both $[Cr(tpy)_2]^{3+}$ and $[Cr(ddpd)_2]^{3+}$ possess six pyridine donors, their LF splittings are unexpectedly very different [Table 5]. The Cr–N bond lengths in these complexes are rather similar, disqualifying these as underlying reason for the different Δ_o, which has been invoked for Al_2O_3:Cr and Cr_2O_3 (vide supra). However, the N–Cr–N bite angles strongly differ due to the five- and six-membered chelate rings in M(tpy) and M(ddpd) units,[2,18,84–86] which results

in differently strong metal-ligand orbital overlap. Hence, this observed difference in ligand field strength must be accounted for by MO theory (vide infra).

TABLE 5. Ligand field parameters (cm^{-1}) of selected (pseudo-)octahedral d^3 TMCs of chromium(III), vanadium(II), manganese(IV), molybdenum(III) and ruby.

Complex	$[CrF_6]^{3-}$ [77]	$[Cr(H_2O)_6]^{3+}$ [77]	$[Cr(NH_3)_6]^{3+}$ [77]	$[Cr(CN)_6]^{3-}$ [78]	$[Cr(bpy)_3]^{3+}$ [79]	$[Cr(tpy)_2]^{3+}$ [80]	$[Cr(ddpd)_2]^{3+}$ [50,81]
Δ_o ($^4T_{2g}$)	14900	17400	21500	26700	23400 [a]	18800	22500 [a,b]
$^4T_{1g}$	22700	24600	28400	32600	28900 [a]	-	
^2E_g	15700	15000	15200	12500	13800 [a]	12900	14000 [a]
$^2T_{1g}$	-	-	-	13100	14400 [a]	13800 [a]	13600 [a]
B	907	726	652	530	496	790	- [c]
C	3430	3320	3450	2740	3280	2480	- [c]
C/B	3.78	4.58	5.30	5.17	6.61	3.14	- [c]
β	0.99	0.79	0.71	0.58	0.54	0.86	- [c]
C/C_{ion}	0.89	0.86	0.90	0.71	0.85	0.65	- [c]
Δ_o/B	25.1	24.0	33.0	50.3	47.2	23.8	- [c]
Complex	$[MnF_6]^{2-}$ [77]	$[V(H_2O)_6]^{2+}$ [77]	$Al_2O_3:Cr^{3+}$ [6 e]	$Cs_2NaYCl_6:Mo^{3+}$ "$[MoCl_6]^{3-}$" [82]			
Δ_o ($^4T_{2g}$)	21700	12300	18100	18800			
$^4T_{1g}$	28200	18500	24600	23200			
^2E_g	16300	(13100) [d]	14400	9291			
$^2T_{1g}$				9672 [a]			
B	599	686	630	487			
C	3900	-	3280	1487			
C/B	6.51	-	5.20	3.05			
β	0.56	0.90	0.69	0.80			
C/C_{ion}	0.79	-	0.85	-			
Δ_o/B	36.3	18.0	28.7	38.6			

[a] averaged value of split bands, [b] from Magnetic Circular Dichroism (MCD) spectroscopy, [c] indeterminable due to different $^2E_g/^2T_{1g}$ order, [d] uncertain, [e] values obtained from resonant inelastic X-ray scattering: B = 573 cm^{-1}, C = 3460 cm^{-1}, C/B = 6.04.[87]

Determining all LF parameters of octahedral TMCs from absorption spectroscopy can become demanding (if not even meaningless in extreme cases), if the complex symmetry strongly deviates from O_h symmetry. Symmetry lowering lifts the t_{2g} and/or e_g* orbital degeneracies, subsequently removing the degeneracy of excited states belonging to E and T irreducible representations. Additionally, intense charge-transfer (CT) or ligand-centered bands can obscure the weak interconfigurational LF and very weak SF absorption bands, making the direct identification of the LF energies by absorption spectroscopy virtually impossible (vide infra). Magnetic Circular Dichroism (MCD)[81,88] or Resonant Inelastic X-ray Scattering (RIXS)[87] offer alternative experimental options to determine energies of ligand field excited states.[89,90] However, these techniques are not commonly available.

Quantum chemical calculations on a suitably high level of theory can deliver energies of LF excited states and derived LF parameters. In the simplest conceivable active space for d^3 chromium(III) complexes, five d orbitals and three d electrons are considered (CASSCF(3,5)). Electron correlation effects can be included by second-order *N*-electron valence state perturbation theory (NEVPT2) correction (CASSCF(3,5)-NEVPT2).[91] Combination with ab initio LF theory (AILFT)[92,93] gives access to calculated LF parameters. Even though the absolute energies calculated by this method are often too high, trends of the experimental LF parameters are well reproduced with this method using DFT optimized GS geometries of chromium(III) complexes [Scheme 1; Tables 5, S2, supplementary material].[53] For example, the trends for LF splitting and *Racah* parameters *B* and *C* for $[Cr(CN)_6]^{3-}$ and $[Cr(NH_3)_6]^{3+}$ are correctly reproduced by this simple approach. These calculations also deliver LF parameters for systems with lower symmetry, for example the polypyridine complexes $[Cr(tpy)_2]^{3+}$, $[Cr(bpy)_3]^{3+}$ and $[Cr(ddpd)_2]^{3+}$ [Table S2, supplementary material]. To obtain more accurate excited state energies, the active space should be expanded according to *Roos*,[91,94] encompassing the five 3d orbitals (t_{2g}/e_g*), the two σ bonding e_g counterparts and a 4d shell (double shell effect) giving a CASSCF(7,12) active space for the *Molecular Ruby* $[Cr(ddpd)_2]^{3+}$ [Fig. S1, supplementary material]. In this system, the t_{2g} orbitals are essentially π non-bonding and the ligand-centered counterparts are weakly correlated and can thus be neglected. The number of states (seven quartet ($^4A_{2g}$, $^4T_{2g}$,

$^4T_{1g}$) and eight doublet roots (^2E_g, $^2T_{1g}$, $^2T_{2g}$)) calculated by CASSCF is chosen so that a balanced population in the t_{2g} and the e_g* orbital sets is obtained, allowing to correlate the excited state energies (multi-electron picture) with the active space orbital energies (one-electron picture). CASSCF(7,12) calculations – augmented by the NEVPT2 correction – (with different numbers of roots) give quite accurate quartet and doublet energies with respect to experimental data and even allow differentiating *Molecular Rubies* with very subtle structural changes in the ligand backbone.[50,51] Even very small variations of the energy of interconfigurational excited states of $[Cr(ddpd)_2]^{3+}$ with hydrostatic pressure could be successfully reproduced by this method with CASSCF(13,10)-NEVPT2 calculations, which include π bonding effects that operate at high pressure and short Cr–N distances.[36]

Analogous DFT/CASSCF(7,12)-NEVPT2 calculations on $[Cr(CN)_6]^{3-}$, $[Cr(bpy)_3]^{3+}$, $[Cr(tpy)_2]^{3+}$ reveal an increasing deviation of the local $[CrL_6]$ coordination sphere from octahedral symmetry as reflected in different Cr–L bond lengths and L–Cr–L bond angles differing from 90 and 180° [Table S3, supplementary material]. These changes in nuclear symmetry are reflected in the splitting of E and T states, which are doubly and triply degenerate in O_h symmetry [Fig. 4(a)]. The average interconfigurational LF and SF state energies still correspond to the O_h LF picture. However, for the understanding of photophysical properties of a particular complex, the exact ES order and splitting become important.

The ES order obtained from the calculations (multi-electron picture) [Fig. 4(a)] can be traced back to the energy order of the active space orbitals (single-electron picture), which in turn is determined by the complex geometry [Fig. 4(b), Table 5]. In the relevant ES energy region shown in Fig. 4(b), lifting the t_{2g} orbital degeneracy splits both SF and interconfigurational LF states as exemplified for $[Cr(bpy)_3]^{3+}$ and $[Cr(ddpd)_2]^{3+}$, while lifting the e_g* orbital degeneracy exclusively acts on the ^4T states as seen for $[Cr(tpy)_2]^{3+}$ and $[Cr(ddpd)_2]^{3+}$ [Fig. 4]. This splitting of the $^4T_{2g}$ state is very pronounced for $[Cr(tpy)_2]^{3+}$ giving a significantly lowered $^4B_1$ state, expressed in Δ_{min} and a ^4E state at higher energy (D_{2d} point group). This splitting strongly diminishes the energy gap $\Delta E_{^4T2g/SF}$ between the $^4T_{2g}$-derived lowest-energy quartet state and the lowest SF states, which profoundly impacts the photophysics (vide infra). Furthermore, the $E(^2E_g) < E(^2T_{1g})$ SF state ordering expected from *Tanabe-Sugano* diagrams based on O_h symmetry can be inverted, when the ^2E_g and $^2T_{1g}$ levels split to a different extent due to symmetry lowering [Fig. 4, 5]. Inspection of the energies of the lowest-energy microstates $^2E_g(1)$ and $^2T_{1g}(1)$ of $[Cr(ddpd)_2]^{3+}$ shows that the energy gain from double occupation of an orbital (b_3) at lower energy compensates the required spin-paring energy [Fig. 5]. CASSCF(13,10)-NEVPT2 calculations reproduce the experimentally observed stronger impact of hydrostatic pressure on the $^2T_{1g}(1)$ state energy of $[Cr(ddpd)_2]^{3+}$ as compared to the $^2E_g(1)$ state energy.[36]

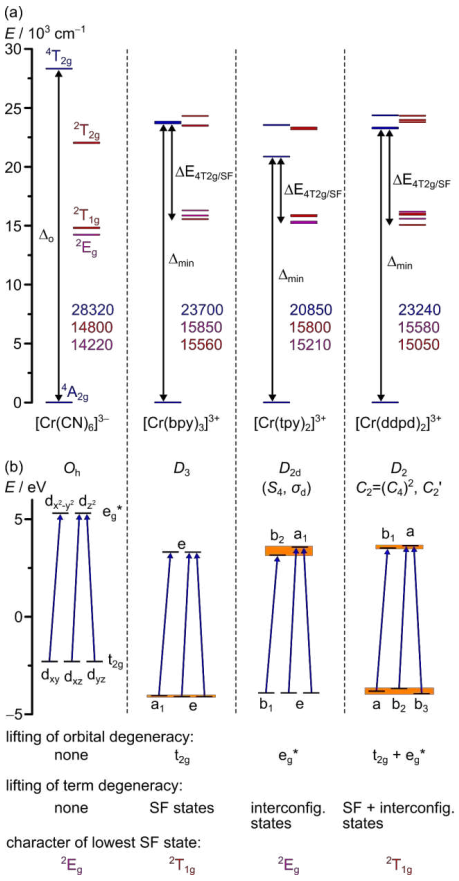

FIG. 4. (a) Energy diagram of electronic states, derived from CASSCF(7,12)-NEVPT2 calculations at the DFT optimized GS geometries of selected chromium(III) complexes with energies (in cm^{-1}) of the lowest-energy $^4T_{2g}$, $^2T_{1g}$ and ^2E_g derived states (blue, red and purple) and (b) idealized point groups of the complexes with energies of the 3d-derived active orbitals. Blue arrows indicate the transitions of the $^4T_{2g}$-derived states. Orange boxes highlight the splitting of t_{2g} and e_g* orbitals, which are degenerate in O_h (supplementary material).

Consequently, analysis of the LF and the influence of the *nephelauxetic effect* based on experimental data of TMCs with symmetry lower than O_h should be done carefully in combination with CASSCF calculations by considering symmetry-related splittings of orbitals and ESs and an energy order of ESs that may differ from the one displayed in *Tanabe-Sugano* diagrams, which are based on O_h symmetry. CASSCF calculations are thus a valuable tool to reveal structure-property relationships for chromium(III) complexes *a posteriori* and furthermore to predict suitably designed ligands for chromium(III)-based chromophores *a priori*.[50,51,53] Mixed-ligand chromium(III) complexes using ddpd, bpmp, bptp and dqp ligands [Scheme 1] possess SF energies averaged from the homoleptic complexes, i.e. averaged nephelauxetic effects [Table S1, supplementary material].[50,51,53,56,95,96]

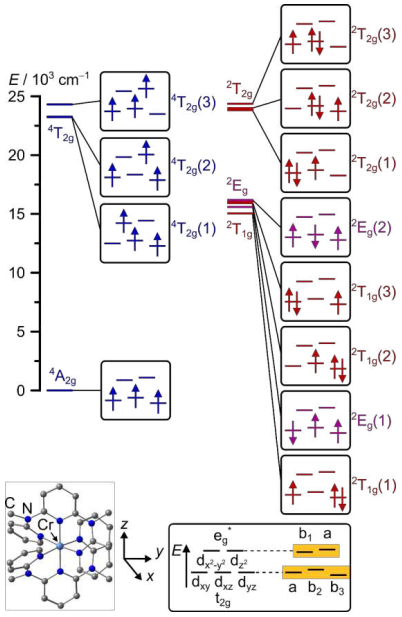

Fig. 5. Energy diagram of metal centered electronic states derived from CASSCF(7,12)-NEVPT2 calculations at the DFT optimized GS geometry of $[Cr(ddpd)_2]^{3+}$ with dominating electron configurations in the microstates illustrating the actual order and splitting of the states (hydrogen atoms are omitted, supplementary material, adapted with permission from Advances in Inorganic Chemistry. Photochemistry and Photophysics of Earth-Abundant Transition Metal Complexes, edited by R. van Eldik, Vol. 83, p. 111 (2024). Copyright 2024, Elsevier.)

In the electrostatic CF and LF models, we have focused on the d orbitals and d electrons, while neglecting ligand-based orbitals and metal s and p orbitals. This led to unexpected relative orderings of some charged and uncharged ligands in the spectrochemical series, e.g. fluoride and carbon monoxide [vide supra, Table 3(a)].[60–67] The LF strengths of tpy and ddpd ligands strongly differ by 3700 cm^{-1}, when coordinated to chromium(III) [Table 5], which is unexpected from CF/LF theory. Furthermore, charge-transfer excited states involving occupied and virtual ligand orbitals are not covered by CF and LF theories. MO theory operating on a basis set involving ligand orbitals of suitable symmetry as well as metal d, s and p valence orbitals can explain the spectrochemical series as well as provide a means to include lower-symmetry effects and CT ESs.

In O_h symmetry, six σ and six σ^* MOs of a_{1g}, t_{1u} and e_g (a_{1g}^*, t_{1u}^* and e_g^*) character form from metal s, p and d orbitals and six symmetry-adapted linear combinations (SALCs) of ligand orbitals (a_{1g}, t_{1u} and e_g) [Fig. 6(a)].[10,97] Ligands with low-lying SALCs of unoccupied orbitals ($t_{2g}(\pi_L^*)$) can form π bonding MOs (π backbonding) and π antibonding MOs with the metal t_{2g} orbitals [t_{2g}, t_{2g}^*, Fig. 6(a)]. Analogously, ligands with high-energy SALCs of occupied π orbitals ($t_{2g}(\pi_L)$) can form metal-ligand π bonding MOs (π bonding) and π antibonding MOs. The t_{2g} and e_g^* orbitals highlighted in the resulting molecular orbital diagram are of high TM character and qualitatively correspond to the LF orbitals with the LF splitting Δ_o in LF theory. It is interesting to note that CF/LF and MO theories arrive at a similar frontier orbital ordering of the t_{2g} and e_g^* orbitals, yet based on different physical origins, namely electrostatic repulsion and covalent interactions, respectively.

SALCs of occupied π orbitals with symmetries different from t_{2g}, namely $t_{1u}(\pi_L)$, $t_{2u}(\pi_L)$ and $t_{1g}(\pi_L)$ can engage in ligand-to-metal CT (LMCT) transitions, while SALCs of empty π^* orbitals with symmetries different from t_{2g}, namely $t_{1u}(\pi_L^*)$, $t_{2u}(\pi_L^*)$ and $t_{1g}(\pi_L^*)$ can contribute to metal-to-ligand CT (MLCT) transitions [Fig. 6(a), 6(b)]. Typically, all resulting MOs are formally divided into (rather) ligand or (rather) metal-centered moieties and the resulting ESs are further categorized in CT states (LMCT, MLCT, ligand-to-ligand CT (LLCT), intervalence CT (IVCT)

in mixed-valent systems) and more localized transitions, namely LF or metal-centered (MC) and ligand-centered (LC) transitions [Fig. 6(b)].[9,10,98] The relative order and occupation of MOs (one-electron picture) determines the order of the ESs (many-electron picture). Hence, from this line of argumentation, energies of ESs can be modulated via GS MO energies. This energy modulation can in principle be achieved by variation of the ligands, the central atoms and the coordination geometry. We will see, however, that this convenient categorization has limitations, when the MOs involved in the electronic transitions are strongly mixed in a more covalent bond situation and not of relatively pure metal or ligand character in a more ionic bonding situation.

First, we look at the influence of metal-ligand σ and π bonding on the LF splitting (ligand and metal effects) and then we discuss CT states within MO theory. Ligands are typically σ donors, which can additionally possess orbitals for π bonding or π backbonding. Pure σ donors (central part of the spectrochemical series, e.g. NH_3, Table 3(a)) only form σ bonding and σ antibonding molecular orbitals [Fig. 6(c)], while the metal t_{2g} orbitals remain nonbonding. The LF splitting arises from the increased energy of the e_g* orbitals. π donor ligands [Fig. 6(c)], such as Cl^-, increase the energy of the metal t_{2g} orbitals diminishing the LF splitting (left region of the spectrochemical series). On the other hand, π acceptor ligands, such as CO, decrease the energy of the metal t_{2g} orbitals increasing the LF splitting (right region of the spectrochemical series) [Fig. 6(c)]. Hence, the σ donor and π donor/acceptor character of the ligands deliver two chemical screws to tune the LF splitting Δ_o, although these ligand properties are not entirely independent. The MO diagram further implies that σ bonding affects the LF splitting Δ_o stronger than π effects.

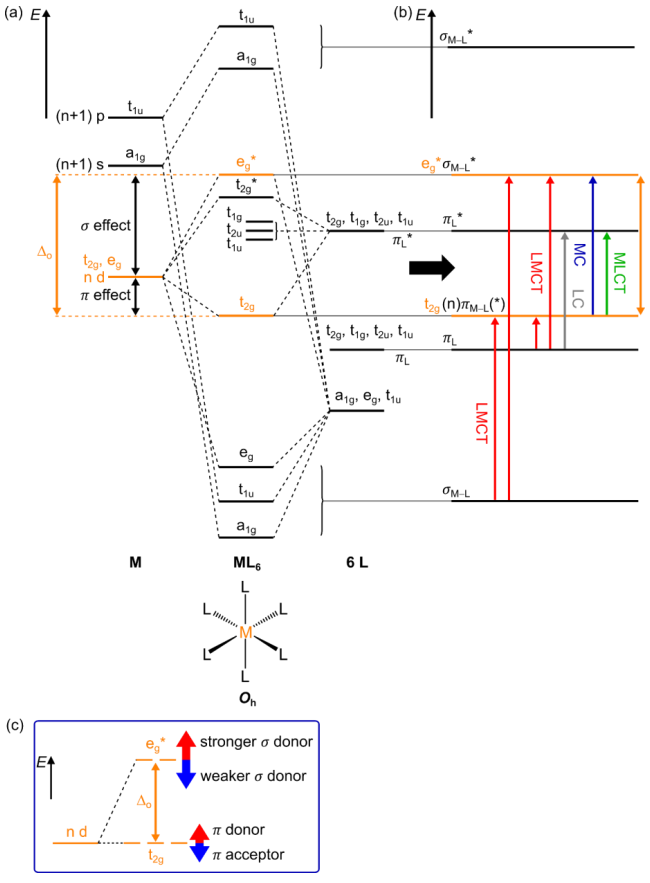

FIG. 6. (a) Molecular orbital diagram for octahedral ML_6 complexes with π backbonding and (b) categorization of derived electronically ESs and (c) influence of σ and π bonding on Δ_o.

Effects of the central metal will be discussed with the aid of two instructive isoelectronic series of d^3 metal ions, namely V^{2+}, Cr^{3+}, Mn^{4+} and Cr^{3+}, Mo^{3+}, W^{3+}. Although numerous Cr^{III}-based SF emitters are reported in the literature,[11–16,28,31–34,99] isoelectronic $3d^3$, i.e. V^{2+} and Mn^{4+} and $4d^3/5d^3$, e.g. Mo^{3+} and W^{3+}, SF emitters are very rare.[16] Complete V^{2+}, Cr^{3+}, Mn^{4+} and Cr^{3+}, Mo^{3+}, W^{3+} experimental series with identical ligands are unfortunately unavailable. However, a few pairs (V^{2+}, Cr^{3+}; Cr^{3+}, Mo^{3+}) have been reported using the ddpd ligand, although with different topologies in some cases (*cisfac*-$[Mo(ddpd)_2]^{3+}$ instead of *mer*-$[Mo(ddpd)_2]^{3+}$) [Scheme 1, Table S1, supplementary material].[100,101] To elucidate the unique role of chromium(III) as color center, we consider isoelectronic and isostructural series $[M(ddpd)_2]^{n+}$ (M = V^{II}, Cr^{III}, Mn^{IV} and Cr^{III}, Mo^{III}, W^{III} with the aid of CASSCF and TDDFT calculations, for MC and CT states, respectively [Fig. 7, 8] (supplementary material).

In the series of isoelectronic 3d complexes *mer*-$[M(ddpd)_2]^{n+}$ of V^{2+}, Cr^{3+} and Mn^{4+}, the CASSCF calculated LF strength Δ_o [Fig. 7(a)] increases with the charge of the central ion as expected from the spectrochemical series of central ions [Scheme 1, Table 3(b)]. Expectedly, the calculated SF state energies increase in this series with increasing *Racah* parameters B and C of the central ions [Table 2], which is not compensated by the increasing nephelauxetic effect from V^{2+} to Mn^{4+} [Table 4]. Interestingly, the slightly different pyridine donors of the ddpd ligand (terminal vs. central pyridine, Scheme 1) split the t_{2g} orbitals with the d_{xz} orbital being slightly above the

d_{xy} and d_{yz} orbitals. This orbital splitting increases from V^{2+} to Mn^{4+}, suggesting a stronger π bonding interaction of the increasingly charged central metal to the more electron-rich central pyridine of the polypyridine ligand. This pronounced splitting of the t_{2g} orbitals inverts the $^2E_g(1)/^2T_{1g}(1)$ levels for $[Cr(ddpd)_2]^{3+}$ and $[Mn(ddpd)_2]^{4+}$ as compared to $[V(ddpd)_2]^{2+}$ and the expected order in ideal O_h symmetry [Fig. 3, 7(a)]. According to the calculations, the overall d orbital energies (t_{2g}, e_g) strongly decrease with increasing charge, while the energies of the more ligand-centered π and π^* orbitals decrease to a lesser extent. Consequently, low-energy MLCT and LMCT transitions are expected for $[V(ddpd)_2]^{2+}$ and $[Mn(ddpd)_2]^{4+}$, respectively, while for $[Cr(ddpd)_2]^{3+}$ the corresponding MLCT and LMCT energies should be higher [Fig. 7(b)]. TDDFT calculations and charge transfer number analyses on $[V(ddpd)_2]^{2+}$, $[Cr(ddpd)_2]^{3+}$ and $[Mn(ddpd)_2]^{4+}$ reveal that the lowest-energy quartet ESs indeed possess large MLCT and LMCT character for $[V(ddpd)_2]^{2+}$ and $[Mn(ddpd)_2]^{4+}$, respectively, while the lowest energy transitions of $[Cr(ddpd)_2]^{3+}$ possess more mixed character [Fig. S2, supplementary material]. This prediction from TDDFT calculations and charge transfer number analysis matches the experimental observations for $[V(ddpd)_2]^{2+}$,[100] $[Cr(ddpd)_2]^{3+}$ [2,18,21,81] and a comparable manganese(IV) complex $[Mn(dgpy)_2]^{4+}$ [Scheme 1].[102,103] However, the simplified discrimination between MLCT, LMCT, LLCT, LC and MC states is not strictly valid when M–L bonding becomes more covalent.

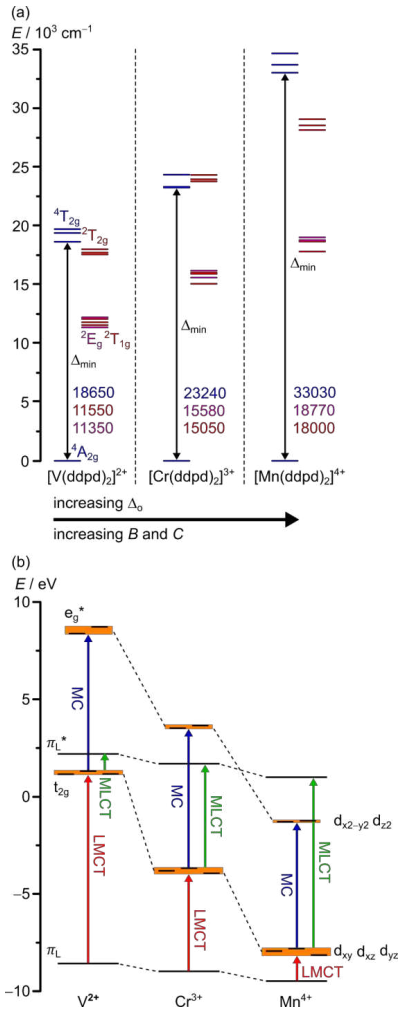

FIG. 7. (a) Energy diagram of LF states, derived from CASSCF(7,12)-NEVPT2 calculations at the DFT optimized GS geometries of *mer*-$[M(ddpd)_2]^{n+}$ complexes of $3d^3$ ions ($M^{n+} = V^{2+}$, Cr^{3+}, Mn^{4+}) with energies (cm^{-1}) of the lowest $^4T_{2g}$, $^2T_{1g}$ and ^2E_g states and (b) energies of the 3d-derived active orbitals and highest occupied and lowest unoccupied ligand-centered π and π^* orbitals (supplementary material).

The lowest quartet ESs in $[V(ddpd)_2]^{2+}$ are essentially of ^{4}MLCT character with varying amounts of MC state admixture [Fig. S2(a), supplementary material].[100] The two lowest quartet ESs of $[Cr(ddpd)_2]^{3+}$ are predominantly of ^{4}LMCT character, followed by states, which can be characterized as ^{4}MC states (states 3, 4 and 6)[Fig. S2(b), supplementary material].[2,51] The electronic spectrum of the experimentally unknown $[Mn(ddpd)_2]^{4+}$ complex should be dominated by allowed transitions to ^{4}LMCT states [Fig. S2(c), supplementary material]. Such intense low-energy absorption bands have indeed been observed in the manganese(IV) complex $[Mn(dgpy)_2]^{4+}$. This complex shows a corresponding weak phosphorescence from a ^{2}LMCT state with small ^{2}MC admixture [Scheme 1, Table S1, supplementary material].[102,103]

As expected from the spectrochemical series of central ions [Table 3(b)], the calculated, photophysical relevant LF splitting Δ_{min} (as indicated by the minimal energy gap between the lowest-energy ^4T microstate and the $^4A_{2g}$ ground state) increases from Cr^{3+} to W^{3+} in the nd^3 series *mer*-$[M(ddpd)_2]^{3+}$ with $M^{3+} = Cr^{3+}$, Mo^{3+}, and W^{3+} [Fig. 8)]. The calculated increase from Mo^{3+} to W^{3+} is less pronounced than that from Cr^{3+} to Mo^{3+} [Fig. 8a]. The decreasing *Racah* parameter B in this series lowers the energy of the SF states [Table 2, Fig. 8]. The splitting of the t_{2g} and importantly of the e_g* orbital sets increases from Cr^{3+} to W^{3+}. This splitting together with the decreasing interelectronic repulsion places one $^4T_{1g}(1)$ microstate below the $^4T_{2g}$ states in *mer*-$[W(ddpd)_2]^{3+}$ [Fig. 8]. The d orbital energies increase from Cr^{3+} to W^{3+} together with the LF splitting. The higher LF splitting of Mo^{3+} places ^{4}LMCT states as lowest-energy ESs with approximately constant energy of the ligand π donor orbital. Indeed, the lowest-energy quartet ES of *cisfac*-$[Mo(ddpd)_2]^{3+}$ is of ^{4}LMCT character [Table S1, supplementary material].[101] Furthermore, the higher d orbital energies in W^{3+} complexes should lead to spin-allowed low-energy ^{4}MLCT transitions [Fig. S3, supplementary material].

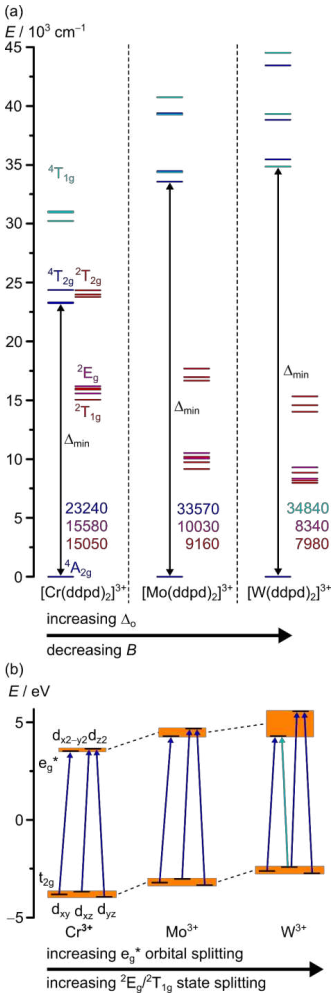

FIG. 8. (a) Energy diagram of electronic states, derived from CASSCF(7,12)-NEVPT2 calculations at the DFT optimized GS geometries of *mer*-$[M(ddpd)_2]^{3+}$ complexes of d^3 ions (M^{3+} = Cr^{3+}, Mo^{3+}, W^{3+}) with energies (in cm^{-1}) of the lowest $^4T_{2g}$, $^2T_{1g}$ and ^2E_g states and (b) energies of the d-derived active orbitals. The blue and turquoise arrows indicate transitions to $^4T_{2g}$ and $^4T_{1g}$ derived states, respectively (supplementary material).

The preceding section gave a detailed view on the ES landscape of pseudo-octahedral d^3 TMCs, including the effects of LF splitting, electron-electron repulsion, symmetry-lowering and the presence of CT states. However, this static picture as illustrated in *Tanabe-Sugano* or *Jablonski*-type diagrams [Fig. 3, 4a, 5, 7a, 8a] valid for the *FC* geometry neglects the effects of nuclear motion on ES energies, which occur due to the change in electron density after photon absorption. The following section hence includes nuclear motion in ESs as described by adiabatic potential energy surfaces (APESs). As often only a few nuclear degrees of freedom become relevant for the ES dynamics, projection of a combination of respective normal modes on a single axis is often convenient, resulting in very intuitive two-dimensional graphs. The most important distortions of ESs of pseudo-octahedral d^3 TMCs arise from an unsymmetric occupation of the e_g* orbitals, namely $(e_g^*)^1$, which is prone to *Jahn-Teller* (*JT*) distortions. These distortions, which dramatically shape the APESs, are discussed in the next section.

III. ADIABATIC POTENTIAL ENERGY SURFACES (APESs), THE JAHN-TELLER EFFECT AND EXCITED STATE DISTORTIONS

SF emission in octahedral d^3 TMCs requires that the $^2T_{1g}/^2E_g$ states are lower in energy than the $^4T_{2g}$ states. This is achieved with $\Delta_o > 20\ B$ at the first crossing point in the *Tanabe-Sugano* diagram [square in Fig. 3]. However, this is only true at fixed nuclear coordinates, i.e. at the GS (*FC*) geometry. Changes in nuclear coordinates (bond lengths and angles), however, can stabilize certain excited states. SF states with $(t_{2g})^3$ electron configurations matching that of the GS will be rather undistorted relative to the GS. Yet, antibonding orbitals are occupied in $^4T_{2g}$ and $^4T_{1g}$ states with $(t_{2g})^2(e_g^*)^1$ electron configurations, which will provoke M–L bond elongation. Furthermore, all states with $(e_g^*)^1$ electron configuration ($^4T_{2g}$ and $^4T_{1g}$ and LMCT states with $(t_{2g})^3(\pi)^1(e_g^*)^1$ electron configuration) fulfill the requirements of the *Jahn-Teller* (*JT*) theorem,[104–107] which states, that "*A nonlinear molecule in an orbitally degenerate electronic state is unstable with respect to spontaneous distortion of the nuclear configuration that removes the degeneracy*". In other words, nonlinear molecules with two or more electronic distributions with the same energy are *JT* active and should distort so that the degeneracy is removed.[105–107] Key for the treatment of the *JT* effect (as well as radiative and nonradiative processes, vide infra) is perturbation theory of degenerate and nondegenerate states, as well as time-dependent perturbation theory. Introductions to perturbation theory can be found in textbooks.[8,108–110] The *JT* effect describes nuclear and electronic motion by vibronic (word contraction of *vibr*ational/electr*onic*) coupling. The *JT* effect is typically introduced in textbooks on octahedral d^9 TMCs (copper(II)), leading to a tetragonally compressed (D_{4h}^c) or elongated (D_{4h}^e) octahedron. Both distortions are energetically equivalent with constant mean orbital energies [Fig. 9(a)–(c)].[64–67] $O_h \rightarrow D_{4h}$ symmetry lowering partially lifts the degeneracy of the t_{2g} and more importantly of the e_g* orbitals with splittings δ_1 and δ_2, respectively [Fig. 9].[111] The δ_1 splitting of the e_g* σ antibonding orbitals with their orbital lobes directly pointing towards the ligands is larger than the δ_2 splitting of the t_{2g} orbitals, which have essentially π nonbonding character [Fig. 2(b), S1, supplementary material]. The symmetry lowering by t_{2g} bending modes exclusively acts on the degeneracy of the t_{2g}(-derived) orbitals, which is depicted in Fig. 9(d) and vide infra. Consequently, an unsymmetric occupation of e_g* orbitals causes a stronger *JT* effect with a larger distortion (e_g stretching modes) than an unsymmetric occupation of t_{2g} orbitals (combination of e_g stretching and t_{2g} bending modes). The latter effect of unsymmetric t_{2g} orbital occupation is hence often neglected. Furthermore, the $3d_{z2}$ orbital (a_{1g}) energy can be lowered by mixing with the 4s orbital (a_{1g}),[64,66] so that tetragonally elongated octahedron geometries are preferred for $3d^9$ $((t_{2g})^6(e_g^*)^3)$ (e.g. copper(II)) and high-spin $3d^4$ $((t_{2g})^3(e_g^*)^1)$ (e.g. chromium(II)) electron configurations.[112–114]

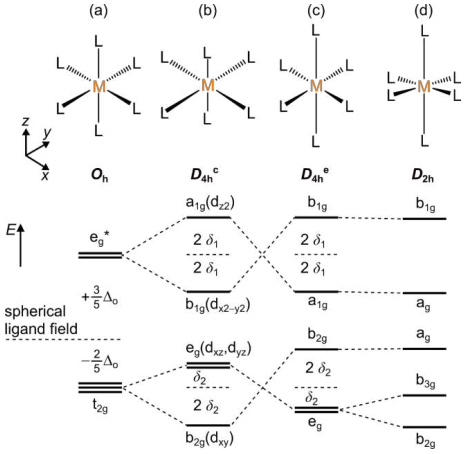

FIG. 9. Schematic energy diagrams of the LF orbitals in (a) an octahedral (O_h), (b) a tetragonally compressed and (c) an elongated TMC (D_{4h} with upper indices c and e indicating compressed and elongated, $T_{2g} \otimes e_g$ coupling) and for (d) a tetragonally elongated octahedral TMC with symmetry lowering by coupling with a t_{2g} (O_h) bending mode (D_{2h}, $T_{2g} \otimes (e_g + t_{2g})$ coupling)). Adapted with permission from Coord. Chem. Rev. 254, 2703 (2010). Copyright 2010, Elsevier.

After this qualitative description of the *JT* effect in octahedral TMCs with unsymmetric occupation of $e_g{}^*$ orbitals, we will now employ perturbation theory and group theory to identify the *JT* active modes that are relevant for states with $(e_g{}^*)^1$ electron configuration and their respective adiabatic potential energy surfaces (APESs) on the basis of the *Born-Oppenheimer* approximation.[105–107] The *Born-Oppenheimer* approximation relies on the assumption that the wavefunctions of nuclei and electrons can be treated separately due to the huge mass differences of the particles. Hence, the positions of nuclei are assumed to be fixed with zero nuclear kinetic energy and constant nuclear-nuclear repulsion.[8,108–110,115,116] The perturbative treatment of this problem is sketched in the supplementary material [Eq. (S1)–(S23)]. The resulting Hamiltonian $\widehat{\boldsymbol{H}}$ of the perturbed system is based on the unperturbed electronic Hamiltonian $\widehat{\boldsymbol{H}}^{(\mathbf{0})} = \widehat{\boldsymbol{H}}(\boldsymbol{Q} = \mathbf{0})$ at reference/equilibrium configuration $\boldsymbol{Q} = \mathbf{0}$, which is corrected by a first-order *Taylor* expansion in $\boldsymbol{Q} = \mathbf{0}$ as the vector of normal coordinates $\boldsymbol{Q} = (Q_1, Q_2, \dots, Q_n)$, weighted by the normal coordinates Q_i [Eq. (9)].[105–107] A concise, didactically well-presented perturbative description of the *Jahn-Teller* effect is provided in ref. [64].

$$\widehat{\boldsymbol{H}} = \widehat{\boldsymbol{H}}^{(\mathbf{0})} + \sum_i \frac{\partial \widehat{\boldsymbol{H}}}{\partial Q_i}\Big|_{\boldsymbol{Q}=\mathbf{0}} Q_i = \widehat{\boldsymbol{H}}^{(\mathbf{0})} + \boldsymbol{Q}\widehat{\boldsymbol{H}}^{(\mathbf{1})} \quad (9)$$

The simplest case is a doubly degenerate state with unperturbed electronic wavefunctions ${\psi_1}^{(0)}$ and ${\psi_2}^{(0)}$ being orthonormal eigenfunctions of $\widehat{\boldsymbol{H}}^{(\mathbf{0})}$ and their corresponding energy eigenvalues set to zero without restriction ${E_1}^{(0)} = {E_2}^{(0)} = 0$. We now consider a single *JT* active vibrational mode of the irreducible representation Γ of a given point group along the corresponding normal coordinate Q_Γ. The resulting perturbed wavefunction is a linear combination of the unperturbed ones $\psi = \chi_1{\psi_1}^{(0)} + \chi_2{\psi_2}^{(0)}$ with the developing coefficients $\chi_i = \chi_i(Q_\Gamma)$ that depend on the nuclear positions (Q_Γ). Solution of the secular determinant set to zero yields a quadratic equation with the solution giving a linear dependence of the energy correction ε on the coupling matrix element ${H_{12}}^{(1)}$. This linear vibronic coupling constant is a volume integral and has the form of a force F_Γ^{12} in the direction of the *JT* active vibrational mode Γ driving the distortion [Eq. (10), (11)].[105–107] Neglecting anharmonicity, the force of distortion F_Γ^{12} is balanced by the harmonic restoring force of the normal vibrational mode Γ in the absence of vibronic coupling with force constant ${k_\Gamma}^{(0)}$ [Fig. 10(a)].[105–107] Eq. (12) gives the energies of the PESs of the two states including vibronic coupling $E_{1,2}(\boldsymbol{Q}_\Gamma)$ [Fig. 10(b)]. The minima of the two PESs are determined from the first derivatives of Eq. (12) being zero at $Q_{\Gamma 0} = \pm\frac{F_\Gamma}{{k_\Gamma}^{(0)}}$ with the *JT* stabilization energy $E_{JT} = -\frac{{F_\Gamma}^2}{2{k_\Gamma}^{(0)}}$.[105–107]. The horizontal (*JT* distortion; $Q_{\Gamma 0}$) and vertical (*JT* stabilization; E_{JT}) displacements of the *JT* distorted PESs

depend on the force constant of $k_\Gamma{}^{(0)}$ of the *JT* mode and on the linear vibronic coupling constant F_Γ as simplified notation of F_Γ^{12}. A large force constant with a steep PES hampers distortion, while a large linear vibronic coupling constant with large slope of the energy correction ε induces a large distortion [Fig. 10].

$$\varepsilon_{1,2} = \pm Q_\Gamma H_{12}{}^{(1)} = \pm Q_\Gamma F_\Gamma{}^{12} \qquad (10)$$

$$H_{12}{}^{(1)} = \langle \psi_1{}^{(0)} | \hat{\boldsymbol{H}}^{(1)} | \psi_2{}^{(0)} \rangle = \int \psi_1{}^{(0)*} \hat{\boldsymbol{H}}^{(1)} \psi_2{}^{(0)} d\tau \quad (11)$$

* Indicates the complex conjugate.

$$E_{1,2}(Q_\Gamma) = \tfrac{1}{2} k_\Gamma{}^{(0)} Q_\Gamma{}^2 \pm F_\Gamma Q_\Gamma \qquad (12)$$

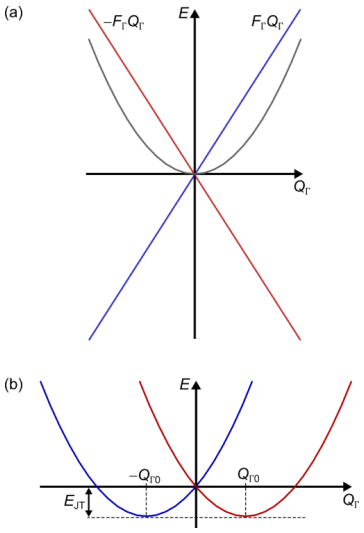

Fig. 10. (a) Schematic representation of the APES of a doubly degenerate state in the absence of vibronic coupling (gray) with linear vibronic coupling functions (red, blue) and (b) after considering the vibronic coupling leading to two (horizontally and vertically shifted) PESs with minima at $\pm Q_{\Gamma 0}$ and *JT* stabilization energy E_{JT} of the distorted system. (b) adapted with permission from Chem. Rev. 121, 1463 (2021). Copyright 2021, American Chemical Society.

Identification of potential *JT* active modes is possible using group theory with the knowledge of the irreducible representation of the degenerate state. In general, the coupling matrix element $H_{mn}{}^{(1)} = F_\Gamma^{mn}$ of two electronic states *m* and *n* is nonzero, only when the direct product $\Gamma_m \times \Gamma \times \Gamma_n$ of the irreducible representations contains the totally symmetric irreducible representation (A_{1g} or equivalent).[8] For the present *JT* case, the two states *m* and *n* are degenerate and belong to the same irreducible representation Γ′. Thus, a vibrational mode can be *JT* active, if the irreducible representation Γ belongs to the direct product of the irreducible representation Γ′ of the degenerate electronic states ($\Gamma \in [\Gamma' \times \Gamma']$).[105–107] To distinguish between electronic states, orbital representations and vibrational modes, large and small italic capitals are used in the following for the respective irreducible representations. The perturbational discussion of a doubly orbitally degenerate electronic state (E) with a vibrational mode (*b*) thus corresponds to the E ⊗ *b JT* problem.[105–107]

We now consider the *JT* active $^4T_{2g}$ state of octahedral d^3 TMCs with a $(t_{2g})^2(e_g{}^*)^1$ electron configuration [Fig. 2]. The symmetric direct product $T_{2g} \times T_{2g}$ of the $^4T_{2g}$ state yields the vibrational modes a_{1g}, e_g and t_{2g} (t_{1g} does not exist in molecules with seven atoms only, i.e. $[ML_6]$). The totally symmetric a_{1g} stretching mode does not remove the degeneracy of the $^4T_{2g}$ state and is thus not *JT* active. However, this mode describes the decreased metal-ligand bond strength in the $^4T_{2g}$ state as compared to the $^4A_{2g}$ GS. The e_g and t_{2g} stretching and bending modes are *JT* active and correspond to tetragonal and trigonal distortions, respectively [Fig. 11].[106,107,111]

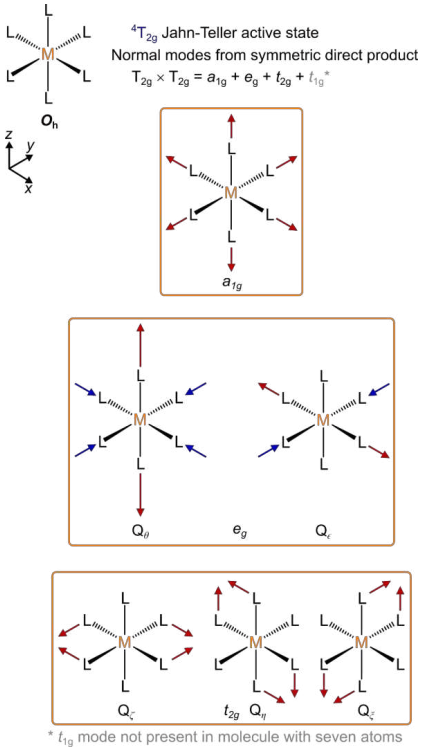

FIG. 11. Vibrational normal modes derived from direct product $T_{2g} \times T_{2g}$ of the *JT* active $^4T_{2g}$ state with *JT* active e_g and t_{2g} modes. The red and blue arrows indicate the displacements of the ligands L in ML_6.

The normal coordinates can be described by deviations of bond lengths (Δa, stretching) and bond angles ($\Delta \alpha$, bending) from the O_h equilibrium geometry values. Plus and minus signs indicate increasing and decreasing bond lengths/angles $\Delta a_i = \Delta a_{-i}$ / $\Delta \alpha_i = \Delta \alpha_{-i}, i = x, y, z$ [Eq (13)–(16)].[106,111] The factor of two in Eq (14) accounts for the doubled bond length change in *z* direction for $Q_{eg(\theta)}$ [Fig. 11].

$$Q_{a1g} = \frac{1}{\sqrt{6}}(\Delta a_z + \Delta a_{-z} + \Delta a_x + \Delta a_{-x} + \Delta a_y + \Delta a_{-y}) \quad (13)$$

$$Q_{eg(\theta)} = \frac{1}{2\sqrt{3}}(2\Delta a_z + 2\Delta a_{-z} - \Delta a_x - \Delta a_{-x} - \Delta a_y - \Delta a_{-y}) \quad (14)$$

$$Q_{eg(\epsilon)} = \frac{1}{2}(\Delta a_x + \Delta a_{-x} - \Delta a_y - \Delta a_{-y}) \quad (15)$$

$$Q_{t2g(\zeta)} = \frac{1}{2}(\Delta \alpha_x + \Delta \alpha_{-x} - \Delta \alpha_y - \Delta \alpha_{-y}) \quad (16)$$

All three modes a_{1g}, e_g and t_{2g} are required to fully describe the distortion of the $^4T_{2g}$ state. However, *FC* factor analyses of $^4A_{2g} \rightarrow {}^4T_{2g}$ absorption and $^4T_{2g} \rightarrow {}^4A_{2g}$ fluorescence spectra of octahedral chromium(III) complexes identified the a_{1g} and e_g stretching modes as main contributors to the ES distortion.[117–121] Consequently, we neglect the t_{2g} bending modes and focus on the a_{1g} and e_g stretching modes [Fig. 11]. Based on Eq. (13)–(15), the vector of the normal coordinates (Q_{a1g},$Q_{eg(\theta)}$,$Q_{eg(\epsilon)}$) of the relevant a_{1g} and e_g modes can be written as product of the coefficient matrix with the vector of total bond length changes (Δa_x, Δa_y, Δa_z) [Eq. (17)]. Matrix inversion then delivers the $^4T_{2g}$ state distortion as metal-ligand bond length changes [Eq. (18)].[111] For example, the hexaammine chromium(III) complex $[Cr(NH_3)_6]^{3+}$ is tetragonally compressed in the $^4T_{2g}$ state with $\Delta a_x = \Delta a_y =$

+0.12 Å and $\Delta a_z = -0.02$ Å relative to the symmetric $^4A_{2g}$ GS, respectively [Fig. 12].[117] The PES of the $^4T_{2g}$ state coupled with the e_g mode indeed corresponds to three equivalent paraboloids. The intersection point is at $\boldsymbol{Q} = \boldsymbol{0}$. The three minima M_i correspond to tetragonally compressed octahedra, which is illustrated on M_1 being on the negative side of the $Q_{eg(\theta)}$ axis [Fig. S4, supplementary material].[106,111]

$$\begin{pmatrix} Q_{a1g} \\ Q_{eg(\theta)} \\ Q_{eg(\epsilon)} \end{pmatrix} = \begin{pmatrix} \frac{2}{\sqrt{6}} & \frac{2}{\sqrt{6}} & \frac{2}{\sqrt{6}} \\ -\frac{1}{\sqrt{3}} & -\frac{1}{\sqrt{3}} & \frac{2}{\sqrt{3}} \\ 1 & -1 & 0 \end{pmatrix} \begin{pmatrix} \Delta a_x \\ \Delta a_y \\ \Delta a_z \end{pmatrix} \quad (17)$$

$$\begin{pmatrix} \Delta a_x \\ \Delta a_y \\ \Delta a_z \end{pmatrix} = \begin{pmatrix} \frac{1}{\sqrt{6}} & -\frac{1}{2\sqrt{3}} & \frac{1}{2} \\ \frac{1}{\sqrt{6}} & -\frac{1}{2\sqrt{3}} & -\frac{1}{2} \\ \frac{1}{\sqrt{6}} & \frac{1}{\sqrt{3}} & 0 \end{pmatrix} \begin{pmatrix} Q_{a1g} \\ Q_{eg(\theta)} \\ Q_{eg(\epsilon)} \end{pmatrix} \quad (18)$$

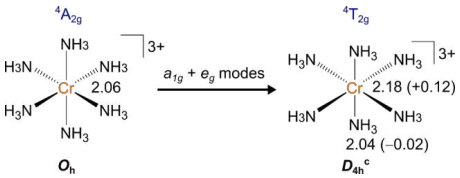

Fig. 12. Equilibrium geometries of $[Cr(NH_3)_6]^{3+}$ in the $^4A_{2g}$ GS (O_h) and tetragonally compressed $^4T_{2g}$ ES (D_{4h}^c), Cr–N bond lengths given in Å and GS-ES bond length changes given in parentheses in Å.

Beyond the strongly *JT* distorted $^4T_{2g}$ states, degenerate doublet states arising from $(t_{2g})^3$ electron configuration should be *JT* active as well. However, these intraconfigurational states are only very weakly *JT* coupled and remain largely undistorted.[122] The essentially nonbonding character of the t_{2g} orbitals can serve as a qualitative explanation for the small *JT* effect. A LF and DFT study on halido model TMCs supports this observation.[111] Indeed, a huge *JT* stabilization energy E_{JT} and *JT* distortion Q_{T0} arise for the high-spin d^4 electron configuration, which is ascribed to the significant reduction of the force constant $k_\Gamma{}^{(0)}$ by occupation of σ antibonding e_g* orbitals. The vibronic coupling of states with an unsymmetric occupation of the e_g* orbitals is determined as approximately three times larger as for *JT* active states with an unsymmetric occupation in the t_{2g} orbital manifold.[111] Consequently, $^4T_{2g}$ and $^4T_{1g}$ states ($(t_{2g})^2(e_g*)^1$) as well as $^{4/2}$LMCT states ($(\pi)^1(t_{2g})^3(e_g*)^1$) can decrease dramatically in energy along *JT* active modes, while the ^2E_g, $^2T_{1g}$ and $^2T_{2g}$ doublet ESs remain essentially undistorted without energy gain.

CASSCF(3,5)-NEVPT2 calculations on the hexahydridochromate(III) model d^3 complex $[CrH_6]^{3-}$ illustrate the energy lowering of ^4T states along the a_{1g} mode with minima at d(Cr−H) ≈ 1.80 Å, while the calculated PESs of the lower-energy intraconfigurational ^2E_g, $^2T_{1g}$ and $^2T_{2g}$ states run essentially parallel to the $^4A_{2g}$ GS PES with minimum at metal-ligand distances of d(Cr−H) = 1.69 Å [Fig. 13(a)] (supplementary material). Hence, the SF states are indeed only very weakly distorted. This situation is described as 'nested potentials' or 'nested states'. The PESs of the $^4T_{2g}$/SF states cross at d(Cr−H) ≈ 2.05 Å with comparably high energy barrier E_a(bISC) ≈ 2.10 eV relative to the SF PES minimum. Consequently, thermally activated SF→$^4T_{2g}$ bISC along the a_{1g} mode alone would require high energies. However, the barriers for bISC E_a(bISC) ≈ 1.26 and 0.96 eV are lowered in compressed (D_{4h}^c) or elongated (D_{4h}^e) octahedral geometries, respectively, after considering the *JT* distortion of the $^4T_{2g}$ state along the $Q_{eg(\theta)}$ stretching vibration of the e_g modes with splitting into $^4B_{2g}$ and ^4E_g states and *JT* stabilization energies E_{JT} of 0.30 and 0.33 eV, respectively [Fig. 13(b)]. Again, the PESs of the SF states run parallel to the GS PES without significant splitting of the states. In the one-electron picture, the large and minor effects on the $^4T_{2g}$ and SF state energies upon a_{1g}/e_g distortion resulting in surface crossings can be traced back to the active space orbital energies with large e_g* and small t_{2g} orbital splittings, respectively [Fig. S5, supplementary material, and Fig. 9].

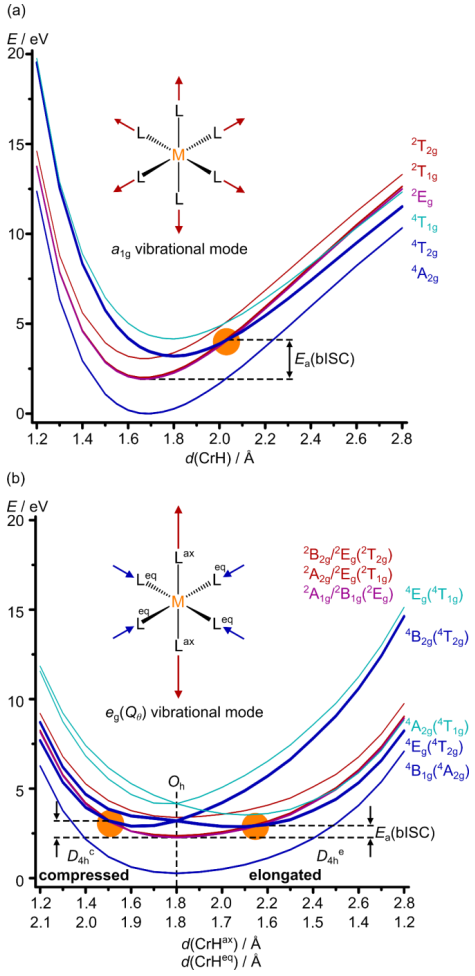

FIG. 13. PES of the model TMC $[CrH_6]^{3-}$ derived from CASSCF(3,5)-NEVPT2 calculations (a) along the a_{1g} normal mode and (b) along the $Q_{eg(\theta)}$ stretching vibration of the e_g normal modes with O_h symmetry at d(Cr−H) = 1.8 Å, corresponding to the $^4T_{2g}$ minimum from the a_{1g} normal mode. $^4T_{2g}/^2E_g/^2T_{1g}$ crossing points highlighted by orange circles.

Strain, as imposed by chelate ligands or a solid-state environment, can influence the PES of *JT* active states.[111] Chelate ligands, such as the tridentate ddpd ligand, induce binding strain. Chelation can hamper large amplitude motions in ESs, for example *JT* active states, which reduces their energy gain due to restricted distortion. This can strongly influence the ES dynamics beyond the *FC* states. To obtain a detailed picture on the distortions of relevant excited states of the parent *Molecular Ruby* $[Cr(ddpd)_2]^{3+}$ beyond the idealized view on octahedral chromium(III) complexes, quartet and doublet LF and LMCT states of $[Cr(ddpd)_2]^{3+}$ were optimized by (TD)DFT calculations [Fig. 14] (supplementary material).[28] As DFT calculated energies of SF states are at odds with the CASSCF results and experimental data, we focus on the structural and electronic features of the optimized ESs, rather than on their relative energies. Hence for *JT* active states, we discuss the *JT* distortion $Q_{\Gamma 0}$ rather than the *JT* stabilization energy E_{JT}. The most important structural differences of the $[CrN_6]$ coordination polyhedron arise from the Cr–N bond lengths to the terminal and central pyridines Cr–N^{term} and Cr–N^{cent}, respectively [Scheme 1].

Due to differences in these bond lengths, a one-dimensional projection, as suitable for $[CrH_6]^{3-}$, is insufficient here. Thus, we project the optimized ESs of $[Cr(ddpd)_2]^{3+}$ onto a two-dimensional representation along the maximum change in $Cr–N^{term}$ and $Cr–N^{cent}$ distances relative to the GS geometry [Fig. 15, Table S4, supplementary material].[28] Expectedly, large distortions are calculated for the interconfigurational $^4T_{2g}(1)$ and $^4T_{2g}(2)$ microstates with elongated Cr–N bonds to a single ddpd ligand and to the four terminal pyridine donors ($Cr–N^{term}$), respectively. In the one-electron picture, these distortions can be traced back to the singly occupied antibonding d_{z2} and d_{x2-y2} orbitals, respectively [Fig. 14, 15, Table S4, supplementary material]. The optimized ^{4}LMCT(1) and ^{4}LMCT(2) states are characterized by a reduced chromium center (Cr^{II}) and a single radical cation $[ddpd]^{\bullet+}$ ligand with the spin density distributed over the central pyridine and the bridging nitrogen atoms [Fig. 14]. The main differences between these two ^{4}LMCT states arise from the d orbital occupation and the magnetic coupling of the ligand radical spin with the d electron spins. ^{4}LMCT(1) and ^{4}LMCT(2) states possess formally low-spin $(t_{2g})^4$ and high-spin $(t_{2g})^3(e_g^*)^1$ chromium(II) centers coupled ferromagnetically and antiferromagnetically to the ligand centered spin, respectively. As the $(t_{2g})^3(e_g^*)^1$ electron configuration is prone to a *JT* distortion, the corresponding ^{4}LMCT(2) state is strongly *JT* distorted due to occupation of the d_{z2} orbital with significant elongation of two $Cr–N^{term}$ bonds [Fig. 15, Table S4, supplementary material]. A fully analogous elongation is observed experimentally and computationally for the high-spin chromium(II) complex $[Cr(ddpd)_2]^{2+}$ with $(t_{2g})^3(e_g^*)^1$ electron configuration, while the low-spin congener ($(t_{2g})^4(e_g^*)^0$) is much more symmetric.[114] Correspondingly, ^{4}LMCT(1) and ^{2}LMCT(1) states with low-spin chromium(II) centers are only weakly distorted [Fig. 14, 15, Table S4, supplementary material]. The LF doublet states $^2T_{1g}(1)$ and $^2E_g(1)$ are much less distorted with slightly contracted $[CrN_6]$ coordination polyhedra [Fig. 15, Table S4, supplementary material]. The Cr–N bonds are slightly more contracted in the $^2T_{1g}(1)$ state than in the $^2E_g(1)$ state. Residual β spin density in the TDDFT geometry optimized molecular structure indicates a multiconfigurational character of the $^2T_{1g}(1)$ state [Fig. 14].[28]

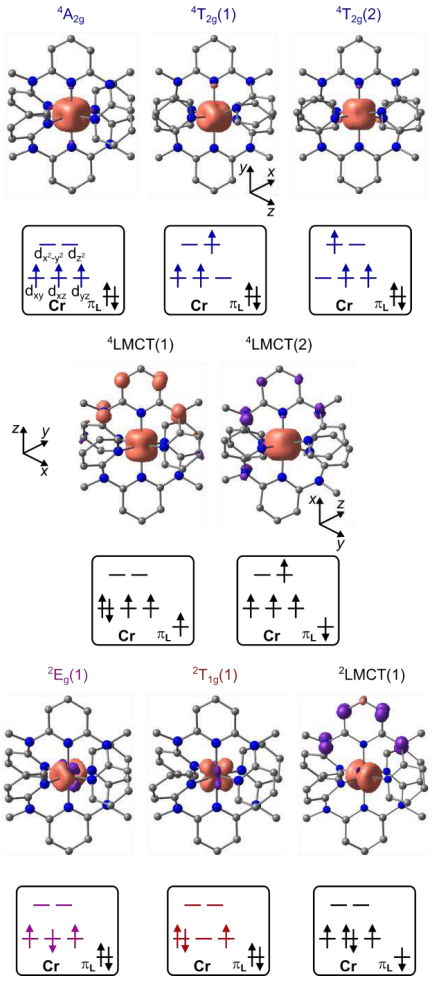

Fig. 14. DFT and TDDFT geometry optimized structures of electronic states of $[Cr(ddpd)_2]^{3+}$ with spin densities. Changes in the Cartesian coordinate system are indicated for the $^4T_{2g}(1)$ and ^{4}LMCT(2) states, determined by the orientation of the d_{z2} orbital (isosurface value 0.01 a.u., α and β spin densities in orange and purple, respectively; supplementary material).

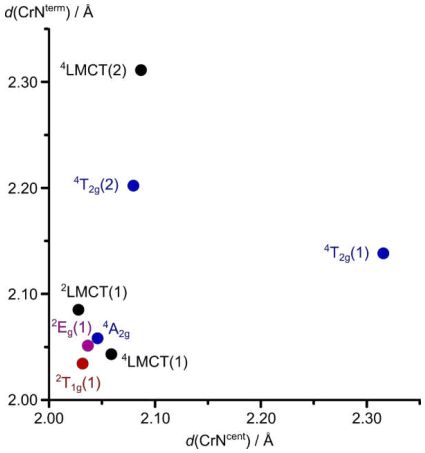

FIG. 15. Projection of (TD)DFT geometry optimized structures of electronic states of $[Cr(ddpd)_2]^{3+}$ on two dimensions spanned by the chromium–nitrogen distances Cr–N^{term} and Cr–N^{cent} in Å, respectively, that display the largest difference to the respective distances in the $^4A_{2g}$ GS geometry (supplementary material).

This section has provided insight into the multidimensional APESs of octahedral chromium(III) complexes in general, and the *Molecular Ruby* $[Cr(ddpd)_2]^{3+}$ in particular. Perturbation theory described the coupling of electron and nuclear motion in *JT* active $^4T_{2g}$ and ^{4}LMCT(2) states with an $(e_g^*)^1$ electron configuration. Similarly, perturbation theory aids to describe transitions between electronic states, including vertical radiative transitions (absorption, emission), horizontal transitions (IC, ISC) and thermally activated transitions involving excited states. This photophysical background for transitions between electronic states will be summarized in the following section and subsequently applied to chromium(III) complexes.

IV. PHOTOPHYSICAL BACKGROUND: VERTICAL, HORIZONTAL AND THERMALLY ACTIVATED TRANSITIONS BETWEEN ELECTRONIC STATES

This section provides a compact overview on the photophysical background, which is required to understand the excited state dynamics of chromium(III) complexes. Quantum mechanics textbooks[8,108,110,115,116,123] and photochemical/-physical textbooks and reviews[9,10,124,125] detail mathematical foundations for the interested reader. Caution is advisable when referring to physical laws from different sources, as different units and unit systems, e.g. SI, cgs or atomic units (a.u.), are employed, which has been stressed previously.[126,127] The following equations refer to SI units, unless noted otherwise.

Experimentally, the photophysics and ES dynamics of molecules can be investigated by time-resolved spectroscopic techniques, such as time-resolved PL and transient absorption (TA) spectroscopy. These techniques allow determining the rate constants for processes occurring on femto- to millisecond timescales. The primary monomolecular photophysical processes after absorption of a photon are divided in radiative (index r) and nonradiative (index nr) processes, which can be described by first-order kinetics and their respective rate constants k_r and k_{nr}.[9,10,124,125] Radiative processes (absorption, PL), occurring with constant nuclear positions, can either be spin-allowed ($\Delta S = 0$; fluorescence, index f) or spin-forbidden ($\Delta S = 1$; phosphorescence, index p) with their respective rate constants k_f and k_p. Similarly, monomolecular nonradiative processes, occurring with constant energy, can be spin-allowed ($\Delta S = 0$; internal conversion, IC) or spin-forbidden ($\Delta S = 1$; intersystem crossing, ISC) with their respective rate constants k_{IC} and k_{ISC}. The fluorescence/phosphorescence and IC/ISC processes are displayed in APES diagrams as vertical and horizontal arrows, accounting for constant geometry and constant energy, respectively. The rates of some excited state processes can be temperature dependent, i.e. occur with an activation barrier. Examples are thermally activated nonradiative and radiative processes $k_{nr}(T)$

and $k_r(T)$, which involve crossings of PESs, such as thermally activated bISC or thermally activated delayed fluorescence (TADF). In many cases, such thermally activated excited state processes can be described by *Arrhenius* or *Eyring* equations.[9,10,124,125]

An ES with a starting population N_0 of molecules being in this state decays with a total rate constant $k = k_r + k_{nr}$ for two processes with first-order rate laws [Eq. (19)].[9,10,124,125] The time evolution of the population of a luminescent ES can be experimentally accessed by recording the PL intensity $I(t)$ over time. $I(t)$ is defined as the number of photons emitted per unit time (s) and unit volume of a solution and is typically given in mol s^{-1} l^{-1} [Eq. (20)].[124] Other spectroscopic techniques, such as TA spectroscopy, allow to observe the evolution of 'dark', i.e. non-luminescent, states over time as well.[128]

$$N(t) = N_0 e^{-(k_r+k_{nr})t} \qquad (19)$$

$$I(t) = I_0 e^{-(k_r+k_{nr})t} \qquad (20)$$

The ES lifetime τ, or PL lifetime τ_{em} for luminescent states, is given by the reciprocal of the total rate constant, which corresponds to the sum over the rate constants of all processes that depopulate the ES [Eq (21)].[9,10,124,125] τ_{em} is the time, in which the PL intensity decreased to $\frac{I(\tau_{em})}{I_0} = e^{-1} \approx 0.37$ of the initial intensity I_0 [Eq. (20), (21)].

$$\tau_{em} = \frac{1}{k_r+k_{nr}} = \frac{1}{\sum_i k_i} \qquad (21)$$

The "efficiency" of a primary process is defined by the quantum yield Φ and is determined by the ratio of the respective rate constant of this primary process and the total rate constant comprising the sum over the rate constants of all deactivating processes. For example, the PL quantum yield Φ_{em} increases with an increasing radiative rate constant k_r and with a decreasing nonradiative rate constant k_{nr} [Eq (22)].[9,10,124,125] Experimentally, the absolute PL quantum yield Φ_{em} can be determined by single-photon counting as the ratio between absorbed to emitted photons [Eq. (23)].[9,10,124,125] Alternatively, PL quantum yields can be determined relative to that of suitable luminescent standards [Table S1, supplementary material].[129–131]

$$\Phi_{em} = \frac{k_r}{k_r+k_{nr}} = k_r \tau_{em} \qquad (22)$$

$$\Phi_{em} = \frac{number\ of\ emitted\ photons}{number\ of\ absorbed\ photons} \qquad (23)$$

Molecules are suitable for photophysical or photochemical applications when the desired process, e.g. PL, is kinetically competitive to all deactivating processes described by k_{nr}. For diffusion controlled bimolecular reactions of an ES (dynamic quenching) as often required for photocatalytic reactions, the lifetime of the reacting ES should be as large as possible, at least in the nanosecond time regime.[132] Hence, nonradiative processes should be retarded for high PL quantum yields for efficient diffusion-controlled bimolecular reactions. A small k_r in addition to a small k_{nr} is required to achieve high ES lifetimes. To achieve high PL quantum yields, a large k_r can be beneficial, but this is not required. For example, the chromium(III) complex $[Cr(tpe)_2]^{3+}$ possesses a high PL quantum yield with a very small k_r, however with a strongly diminished k_{nr} [Table S1, supplementary material].[17,28,57]

Numerous parameters affect the lifetimes of ESs such as selection rules for radiative and nonradiative transitions, the ES ordering, ES distortions and coupling of states. First, we discuss radiative (vertical) transitions, i.e. light absorption and PL including the pertinent selection rules, followed by horizontal transitions (IC, ISC) in the weak and strong coupling limits and finally energy transfer to the environment.

IVA. Vertical radiative transitions: absorption and emission

Absorption of one photon of light with frequency ν_{12} by a molecule induces an electronic transition between an initial (index 1) state, most often the GS, with energy E_1 and a final ES (index 2) with energy E_2, so that the resonance condition of the so-called *Bohr* equation, essentially energy conservation, [Eq. (24)] is fulfilled.[8,10,108] The square of the absolute electric transition dipole moment $|\boldsymbol{\mu_{12}}|^2$ is proportional to the probability of an electronic transition between two electronic states with wavefunctions ψ_1 and ψ_2 and the dipole moment

operator for the electric part $\hat{\boldsymbol{\mu}}$ [Eq. (25), (26)].[8,108,133] We will see that the probability of an electronic transition is linked to the symmetry of the orbital wavefunctions and the spin functions of the initial and final states (selection rules), while the shape of an absorption or emission band is related to the horizontal displacement of the involved PESs. Finally, we will see how vibrational coupling and spin-orbit coupling (SOC) serve to overcome strict selection rules.

$$\Delta E = E_2 - E_1 = h\nu_{12} \qquad (24)$$

$h =$ *Planck* constant

$$\boldsymbol{\mu_{12}} = \langle\psi_2|\hat{\boldsymbol{\mu}}|\psi_1\rangle = \int \psi_2^* \hat{\boldsymbol{\mu}}\, \psi_1 \, d\tau \quad (25)$$

$$\hat{\boldsymbol{\mu}} = -e \sum_i \boldsymbol{r_i} \qquad (26)$$

e is the elementary charge, which is multiplied by the sum over the locations $\boldsymbol{r_i}$ (a vector) of the electrons.

To enable an electronic transition with absorption (state 1→state 2) or emission (state 2→state 1) of radiation, the electric transition dipole moment $\boldsymbol{\mu_{12}}$, must be nonzero.[8,108,133] A transition is called electric dipole allowed ($|\boldsymbol{\mu_{12}}|^2 > 0$) or electric dipole forbidden ($|\boldsymbol{\mu_{12}}|^2 = 0$). Electronic states with their wavefunctions are determined by the quantum numbers (n, l, m_l, m_s in the one-electron scheme), which leads to selection rules for electric dipole allowed transitions.[8,108,133] The orbital angular momentum quantum number l must change by ± 1. In centrosymmetric molecules, this corresponds to a parity change of the wavefunction, i.e. the behavior under an inversion symmetry operation. Consequently, electronic transitions between states of *gerade* g and *ungerade* u symmetry are allowed in centrosymmetric molecules, which is called *parity* selection rule or *Laporte's* selection rule [Table 6].[8,108,133] Hence, LF transitions, i.e. transitions between d orbitals, e.g. $t_{2g} \rightarrow e_g^*$ [Fig. 2], are *Laporte*-forbidden in complexes with O_h symmetry. The *magnetic quantum number* selection rule depends on the polarization of the incident light. These rules can be transferred to many electron systems, described with the *Russel-Saunders* or LS-coupling scheme with total orbital angular momentum L and total spin S combined to the total angular momentum J with respective magnetic quantum numbers ($M_i, i = L,\ S,\ J$).[8,108,133] These magnetic dipole-allowed transitions are ca. 10^5 times less probable than electric dipole-allowed transitions.[8] Yet, magnetic dipole-allowed transitions are of interest in the circularly polarized luminescence of chiral enantioenriched chromium(III) complexes.[46,55,58,88,95,96,134–136] A third type of transitions are electric quadrupole-allowed transitions, which are 10^8 times weaker compared to electric dipole-allowed transitions.[8]

The *spin* selection rule states that the total spin S must be conserved in an electric dipole allowed electronic transition [Table 6].[8,108,133] Hence, electronic transitions are either spin-allowed ($\Delta S = 0$) or spin-forbidden ($\Delta S \neq 0$). Compared to the *parity* and the *magnetic quantum number* selection rules, this *spin* conservation rule is the strictest one, resulting in often very small electric transition dipole moments $\boldsymbol{\mu_{12}}$ for spin-forbidden transitions.[108] However, as the spin S is only well defined in systems with negligible or weak spin-orbit coupling, SOC provides a means to relax the strict *spin* selection rule. The SOC constant ζ for a hydrogen-like atom roughly scales with the effective nuclear charge of an atom to the power of four $\zeta \sim {Z_{eff}}^4$ (vide infra).[8] This inclusion of SOC provided by atoms with high effective nuclear charge, leads to the so-called *heavy-atom effect*, that enables formally spin-forbidden transitions such as optical excitation to an ES with different spin, phosphorescence and also ISC (vide infra). As the total spin S remains well defined in the LS-coupling scheme, an extended selection rule for the change in total angular momentum can be derived for systems that can be described by the LS-coupling scheme [Table 6].[8,108,133]

TABLE 6. Selection rules for electric dipole allowed electronic transitions.[8,108,133]

Parity selection rule/Laporte's selection rule $\Delta l = \pm 1$ $(g \leftrightarrow u)$ (one-electron system) $\Delta L = \pm 1$ (multi-electron system, LS-coupling)
magnetic quantum number selection rule $\Delta m_l = \pm 1$ (circularly polarized light) $\Delta m_l = 0$ (linearly polarized light) (analogous for M_L, multi-electron system)
spin selection rule $\Delta S = 0$
total angular momentum selection rule $\Delta J = 0, \pm 1$ (for $J \neq 0$)

$\Delta J = \pm 1$ (for $J = 0$)

The oscillator strength f_{12} of an absorption connects the probability of an electronic transition $|\boldsymbol{\mu_{12}}|^2$ with the molar absorption coefficient $\varepsilon(\nu)$ in the decadic logarithm representation as experimentally accessible quantity [Eq. (27)].[8,108,126,127] The frequency ν_{12} in this expression is assumed to be constant over the entire absorption band, which is typically fulfilled for sharp bands.[8] Importantly, f_{12} is proportional to the energy difference ΔE_{12} between the initial and final state (most often the GS and an ES), as well as to the square of the absolute electric transition dipole moment $|\boldsymbol{\mu_{12}}|^2$. The oscillator strength approaches $f_{12} \approx 1$ for electric dipole allowed and $f_{12} \ll 1$ for forbidden transitions.[8,108,126,127] In computational chemistry, f_{12} is a common quantity, which can be obtained from TDDFT calculations. Experimentally, the oscillator strength can be obtained from the absorption band by integrating the band over the molar absorption coefficient in decadic logarithm $\varepsilon(\nu)$ or $\varepsilon(\tilde{\nu})$ in $m^2\ mol^{-1}$ and $M^{-1}\ cm^{-1}$, respectively, with frequency in s^{-1} and wavenumbers $\tilde{\nu}$ in cm^{-1} [Eq. (28)].[8] A rectangle given by the molar absorption coefficient at the absorption maximum $\varepsilon_{max}(\tilde{\nu})$ and the full width at half maximum $FWHM(\tilde{\nu})$ [Eq. 29] approximates the integral over a nearly Gaussian shaped absorption band [Fig. S6, supplementary material]. Hence the oscillator strength f_{12} of the underlying transition can be easily estimated from $\varepsilon_{max}(\tilde{\nu})$ and $FWHM(\tilde{\nu})$ of spectrally isolated absorption bands. This useful approximation of an integral over a Gaussian shaped band is also used in the *Marcus-Hush* theory for the analyses of intervalence CT bands,[137–140] as didactically well presented in reference [141]. If absorption bands overlap, the band pattern can be fitted by a suitable number of Gaussian or *Voigt* functions. Integration over the fitted band delivers the respective oscillator strength f_{12} [Eq. (28)].

$$f_{12} = \frac{4\pi m_e \nu_{12}}{3e^2\hbar}|\boldsymbol{\mu_{12}}|^2 = \frac{2m_e}{3e^2\hbar^2}\Delta E_{12}|\boldsymbol{\mu_{12}}|^2 = \frac{4m_e c\varepsilon_0}{N_A e^2}\ln(10)\int \varepsilon(\nu)\, d\nu \quad (27)$$

m_e electron mass, e elementary charge, $\hbar$ reduced *Planck's* constant, c speed of light, N_A *Avogadro's* constant, ε_0 vacuum permittivity.

$$f_{12} = 6.257 \times 10^{-19}\ln(10)\int \varepsilon(\nu)\, d\nu = 1.876 \times 10^{-9}\ln(10)\int \varepsilon(\tilde{\nu})\, d\tilde{\nu} = 4.319 \times 10^{-9}\int \varepsilon(\tilde{\nu})\, d\tilde{\nu} \quad (28)$$

$\varepsilon(\nu)$ is given in $m^2\ mol^{-1}$ and $\varepsilon(\tilde{\nu})$ in $M^{-1}\ cm^{-1}$ with ν in s^{-1} and $\tilde{\nu}$ in cm^{-1}, respectively.

$$f_{12} \approx 4.319 \times 10^{-9}(\varepsilon_{\max}(\tilde{\nu}) \times FWHM(\tilde{\nu})) \quad (29)$$

For the reverse radiative process between states 2 and 1, i.e. PL, a corresponding oscillator strength f_{21} is defined as well.[8,108,126,127] Both oscillator strengths are related by the degeneracies g_1 and g_2 of the lower and upper states, respectively [Eq. (30)].[108,126,127] As an oscillator strength is proportional to the square of the absolute electric transition dipole moment $|\boldsymbol{\mu}|^2$ [Eq. (27)], the transition dipole moments for absorption $|\boldsymbol{\mu_{12}}|^2$ and PL $|\boldsymbol{\mu_{21}}|^2$ are related by the state degeneracies g_1 and g_2 as well [Eq. (31)]. For example, the orbital degeneracies of $^4A_{2g}$ and $^4T_{2g}$ states of octahedral chromium(III) complexes amount to 1 and 3, respectively, which affects the integrated intensities of this LF absorption and the corresponding LF fluorescence band.

$$g_1 f_{12} = -g_2 f_{21} \quad (30)$$

$$g_1|\boldsymbol{\mu_{12}}|^2 = g_2|\boldsymbol{\mu_{21}}|^2 \quad (31)$$

Now, we want to connect $|\boldsymbol{\mu_{21}}|^2$ with the experimentally accessible radiative rate constant k_r for a PL process. Oscillator strengths can be deduced from the *Einstein* coefficients of induced absorption B_{12} and stimulated emission B_{21}, which are proportionality factors of the respective transition rate constants. The descriptions 'induced' and 'stimulated' indicate, that the electronic transitions are "forced" by the interaction, i.e. coupling, of the electronic wavefunction with the oscillating electric field of light [Eq. (32), (33)].[8,108,126,127] Continuous irradiation with light of frequency $\nu_{12} = \nu_{21}$ would populate lower and upper states 1 and 2 equally, which conflicts with the *Boltzmann* distribution.[8,108,126,127] Introducing the *Einstein* coefficient for spontaneous emission A_{21}, which is a transition rate constant, removes this discrepancy. If stimulated emission is negligible, then A_{21} equals the overall radiative rate constant k_r of emission [Eq. (34)].[8,108,126,127] According to the *Strickler-Berg* relation,[142] k_r has to be multiplied with the square of the refractive index n^2 for the experimental determination of the emission rate constants in solution (but not in vacuo).[143] Importantly, k_r depends on the third power of the emission energy ${\Delta E_{21}}^3$ [Eq. (34)]. For example, assuming identical transition dipole moments $\boldsymbol{\mu_{21}}$ for red/NIR

and blue PL, a PL process at 800 nm ($\Delta E_{21} = 12500$ cm^{-1}) is hence eight times slower than a PL process at 400 nm ($\Delta E_{21} = 25000$ cm^{-1}). This assessment clearly highlights one challenge of obtaining chromophores emitting in the NIR spectral region with high PL quantum yields. As the energies of ^2E_g and $^2T_{1g}$ SF states of chromium(III) complexes are typically below 700 nm (14285 cm^{-1}), the respective radiative rate constants k_r will be intrinsically small based on this relationship [Eq. (34)]. The radiative rate constants k_r being diminished by the low PL energy ΔE_{21} represents not the only challenge for SF phosphorescence of chromium(III) complexes, as the *spin selection rule* and *Laporte's selection rule* reduce k_r for the SF PL even further. Circumvention of the *spin selection rule* by SOC will be discussed next.

$$B_{12} = \frac{\pi}{3\varepsilon_0 h^2}|\boldsymbol{\mu_{12}}|^2 = \frac{e^2}{8\pi\varepsilon_0 m_e h \nu_{12}} f_{12} \qquad (32)$$

$$g_1 B_{12} = g_2 B_{21} \quad (33)$$

$$k_r = A_{21} = \frac{8\pi h {\nu_{21}}^3}{c^3} B_{21} = \frac{8\pi^2 {\nu_{21}}^3}{3\varepsilon_0 h c^3}|\boldsymbol{\mu_{21}}|^2 = \frac{{\Delta E_{21}}^3}{3\pi\varepsilon_0 h^4 c^3}|\boldsymbol{\mu_{21}}|^2 \quad (34)$$

Phosphorescence is a spin-forbidden radiative process, leading to a vanishing transition dipole moment (*spin selection rule*) [Table 6].[8,108,133] Without SOC, the radiative rate constant k_r would be zero. A perturbative treatment of the transition dipole moment can take SOC into account.[144,145] Perturbation theory of nondegenerate states as required in this context can be found in textbooks.[8,108–110] The following exemplary discussion of SOC considers phosphorescence from a lowest-energy triplet ES to a singlet GS ($T_1 \rightarrow S_0$). Triplet states consist of three spin sublevels with $M_S = -1, 0, +1$, which are eigenfunctions of the $\widehat{\boldsymbol{S^2}}$ and $\widehat{\boldsymbol{S_z}}$ operators. SOC lifts the degeneracy of these three sublevels of the T_1 state. The triplet spin wavefunctions for the SOC treatment are conveniently expressed by the zero projections onto the Cartesian axes $T_1^\alpha (\alpha = x, y, z)$.[144,145] The wavefunctions of the S_0 and the T_1 states are then perturbed by admixing triplet and singlet state character, respectively.[144,145] The first-order SOC corrected triplet and singlet wavefunctions $\tilde{T}_1^\alpha$ and $\tilde{S}_0$ are described by Eq. (35) and (36), respectively.[144,145] The amount of singlet and triplet mixing to $\tilde{T}_1^\alpha$ and $\tilde{S}_0$ scales with the respective reciprocal energy differences $(E(T_1) - E(S_n))^{-1}$ and $(E(S_0) - E(T_m))^{-1}$ [Eq. (35), (36)]. As the $E(S_0) - E(T_1)$ gap is typically larger than the $E(T_1) - E(S_n)$ gaps with $n \geq 1$ and a higher density of singlet states S_n is present in this energy region, perturbation of T_1 levels is often more pronounced than perturbation of the S_0 GS. The expectation value $\boldsymbol{\mu}_{\tilde{T}_1^\alpha \tilde{S}}$ for the electronic transition dipole moment for the $\tilde{T}_1^\alpha \rightarrow \tilde{S}_0$ transition of the perturbed electronic states is obtained as Eq. (37) [Eq. (S24)–(S26), supplementary material]. Inspection of Eq. 37 indicates that the singlet triplet admixture borrows intensity from the non-vanishing electric transition dipole moments between states of like multiplicity S_0/S_n and T_1/T_m, weighted by SOC and the respective singlet-triplet energy differences $E(T_1) - E(S_n)$ and $E(S_0) - E(T_m)$.[144,145] The radiative rate constant k_r^α [Eq. (34)] for one triplet spin function $\tilde{T}_1^\alpha$ is given by Eq. (38). Provided that zero-field splitting of the triplet state is small, the singlet-triplet energy gap ΔE_{TS} of the unperturbed states can be employed. Then, the radiative rate k_r^α depends on ${\Delta E_{TS}}^3$ and $\left|\boldsymbol{\mu}_{\tilde{T}_1^\alpha \tilde{S}}\right|^2$ [Eq. (38)].[144,145] If the spin-allowed singlet-singlet and triplet-triplet transitions possess small or vanishing electric transition dipole moments $\langle S_0|\hat{\boldsymbol{\mu}}|S_n\rangle$ and $\langle T_m^\alpha|\hat{\boldsymbol{\mu}}|T_1^\alpha\rangle$ themselves [Eq. 25], intensity borrowing will be inefficient. For example, this is the case for spin-allowed, but *Laporte*-forbidden LF transitions in centrosymmetric TMCs (in the absence of vibronic coupling, vide infra).

$$\tilde{T}_1^\alpha = T_1^\alpha + \sum_{n=0}^{\infty} \frac{\langle S_n|\widehat{\boldsymbol{H}}_{\boldsymbol{SO}}|T_1^\alpha\rangle}{E(T_1) - E(S_n)} S_n \quad (35)$$

$$\tilde{S}_0 = S_0 + \sum_{\beta}^{x,y,z} \sum_{m=1}^{\infty} \frac{\langle T_m^\beta|\widehat{\boldsymbol{H}}_{\boldsymbol{SO}}|S_0\rangle}{E(S_0) - E(T_m)} T_m^\beta \qquad (36)$$

$$\beta = x, y, z$$

$$\boldsymbol{\mu}_{\tilde{T}_1^\alpha \tilde{S}} = \langle \tilde{S}_0|\hat{\boldsymbol{\mu}}|\tilde{T}_1^\alpha\rangle = \sum_{n=0}^{\infty} \frac{\langle S_n|\widehat{\boldsymbol{H}}_{\boldsymbol{SO}}|T_1^\alpha\rangle}{E(T_1) - E(S_n)} \langle S_0|\hat{\boldsymbol{\mu}}|S_n\rangle + \sum_{m=1}^{\infty} \frac{\langle T_m^\alpha|\widehat{\boldsymbol{H}}_{\boldsymbol{SO}}|S_0\rangle^*}{E(S_0) - E(T_m)} \langle T_m^\alpha|\hat{\boldsymbol{\mu}}|T_1^\alpha\rangle \qquad (37)$$

* indicates the complex conjugate.

$$k_r^{\alpha} = \frac{\Delta E_{TS}{}^3}{3\pi\varepsilon_0 h^4 c^3} \left|\boldsymbol{\mu}_{\tilde{T}_1^{\alpha}\tilde{S}}\right|^2 \quad (38)$$

In fact, transferring these considerations on the $T_1 \rightarrow S_0$ phosphorescence to the SF PL of centrosymmetric chromium(III) complexes shows that quartet admixture to the doublet SF states solely from quartet LF states ($^4T_{2g}$) has only a minor effect on the intensity borrowing, due to the *Laporte*-forbidden nature of the LF transitions. Symmetry breaking, either static by a non-centrosymmetric coordination environment or dynamic by suitable *ungerade* vibrations, is thus required to enable SF PL. Beyond intensity borrowing from quartet LF transitions via symmetry breaking, intense low-energy parity- and spin-allowed ^{4}CT transitions can in principle provide an intensity borrowing pathway for SF PL.

Now, we describe the possible associated nuclear motion that can follow an electronic transition. Nonlinear molecules with *N* atoms have 3*N*−6 vibrational degrees of freedom (normal modes). Hence, each electronic state consists of 3*N*−6 series of vibrational sublevels, one series for each normal mode. Similarly to the *Born-Oppenheimer* approximation (vide supra for the *JT* effect, supplementary material), the *Franck-Condon* (*FC*) *principle* states that the nuclear configuration of a molecule experiences no change during an electronic transition, thanks to the much larger mass of nuclei compared to that of electrons.[8,108,133] Redistribution of electron density is much faster than the duration of a vibration (nuclear motion). The nuclear kinetic energy remains constant due to the negligible small kinetic momentum of a photon.[133] Transitions with conservation of the nuclear positions are called *vertical transitions* and displayed in PES diagrams as vertical arrows. During an electronic transition, the spatial electron density distribution changes, i.e. the potential energy of the nuclear wavefunction and the nuclei follow the electron density along an energy gradient to the minimum geometry. The resulting nuclear motion *after* an electronic transition can be described by normal modes or a combination thereof. These combinations of electronic transitions with vibrational transitions are called *vibronic transitions*.[8]

We now discuss the situation where a single vibration, either a normal or a combination mode, is activated. Within the *Born-Oppenheimer* approximation, the total wavefunction $\Psi_{n,\upsilon}(\boldsymbol{r},\boldsymbol{R})$ is described as product of the electronic wavefunction $\psi_n(\boldsymbol{r},\boldsymbol{R})$ of the electronic state n and the nuclear wavefunction $\chi_{n,\upsilon}(\boldsymbol{R})$ of the electronic state n and the vibrational state υ [Eq. (39)].[8] For simplification, we abbreviate $\psi_n(\boldsymbol{r},\boldsymbol{R})$ and $\chi_{n,\upsilon}(\boldsymbol{R})$ as ψ_n and $\chi_{n,\upsilon}$, respectively, by omitting the coordinates in the following. The expectation value for the electric transition dipole moment $\boldsymbol{\mu}_{\mathbf{1}(\upsilon)\mathbf{2}(\upsilon')}$ for two electronic states 1 and 2 in their vibrational (sub)levels υ and υ', respectively, is given by Eq. (40) as product of the electronic part $\boldsymbol{\mu}_{\mathbf{12}}$ and the vibrational overlap integral $S(\upsilon',\upsilon)$ of two vibrational states υ and υ' [Eq. (S27), (S28), supplementary material]. As long as the nuclear displacement is small, the electronic part $\boldsymbol{\mu}_{\mathbf{12}}$ does not depend on the nuclear coordinates $\boldsymbol{R}$.[8] The vibrational overlap integral $S(\upsilon',\upsilon)$ describes the influence of the differences of the PESs of states 1 and 2. As the intensity of an electronic transition is proportional to the square of the absolute of the electric transition dipole moment $\left|\boldsymbol{\mu}_{\mathbf{1}(\upsilon)\mathbf{2}(\upsilon')}\right|^2$, the intensity depends on the square of the absolute of the vibrational overlap integrals $|S(\upsilon',\upsilon)|^2$, which are called *Franck-Condon* factors (*FC* factors).[8,108,133]

$$\Psi_{n,\upsilon}(\boldsymbol{r},\boldsymbol{R}) = \psi_n(\boldsymbol{r},\boldsymbol{R})\chi_{n,\upsilon}(\boldsymbol{R}) = \psi_n\chi_{n,\upsilon} \quad (39)$$

$$\boldsymbol{\mu}_{\mathbf{1}(\upsilon)\mathbf{2}(\upsilon')} = \boldsymbol{\mu}_{\mathbf{12}}\langle\chi_{2,\upsilon'}|\chi_{1,\upsilon}\rangle = \boldsymbol{\mu}_{\mathbf{12}}S(\upsilon',\upsilon) \quad (40)$$

For the absorption GS→ES, only the lowest vibrational level of the GS (υ = 0) is populated at ambient temperatures, hence only the *FC* factors $|S(\upsilon',0)|^2$ need to be considered. Likewise, the emission ES→GS occurs primarily from the zero vibrational level ($\upsilon' = 0$) of the electronic ES requiring only the *FC* factors $|S(0,\upsilon)|^2$ for the calculation of the electric transition dipole moment [Fig. 16]. For simplicity, we assume harmonic potentials for GS and ES with identical vibrational frequencies in the following.

A small (zero) ES distortion, i.e. small horizontal displacement of the ES potential or nested states, results in sharp absorption and emission bands as illustrated in Fig. 16(a) as projection on y axes for absorption (blue) and emission (red).[10,124] Only the vibrational overlap integral between the zero vibrational levels $S(0,0)$ ($\upsilon = \upsilon' = 0$) does not vanish, so that absorption and emission energies coincide (E_{00}). The *Stokes* shift is defined as the energy difference between absorption and emission band maximum of transitions between the *same* ES and GS. A weak

(zero) ES distortion leads to a small (zero) *Stokes* shift [Fig. 16(a)]. Hence, the experimentally observable *Stokes* shift is a good indicator for ES distortions, provided that the observed transitions involve the same GS and ES.

For a distorted ES, described by a horizontal displacement of the ES PES, the non-vanishing vibrational overlap integrals $S(v',0)$ and $S(0,v)$ result in *vibrational progressions* [Fig. 16(b)]. These progressions can be experimentally resolved in some cases, for example at lower temperature. However, more frequently broad absorption and emission bands result due to anharmonicity and the presence of more than one activated vibration. As the absorption and emission band maxima are found at higher and lower energy than E_{00}, respectively, a large *Stokes* shift results. One half of the *Stokes* shift arises from the hypsochromically shifted absorption band maximum, and the other half from the bathochromically shifted emission band maximum. The absolute value of the *Stokes* shift thus depends on the degree of the distortion and the frequency of the relevant distortional mode. Provided that the vibrational frequencies of the GS and ES are very similar, absorption and emission bands behave like mirror images [Fig. 16(b)]. This mirror image relationship can assist assignment of the bands.[10,124] The energy difference between the zero vibrational levels E_{00} can be estimated from the intersection of the intensity normalized absorption and emission spectra [Fig. 16(b)].

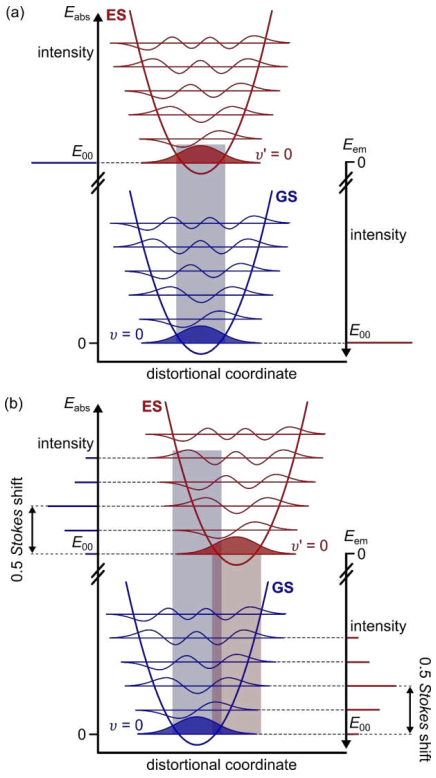

FIG. 16. Schematic PES diagrams along a distortional coordinate with relevant vibrational wavefunctions in a harmonic potential (a) for a nested ES and (b) for a distorted ES with intensities of vibronic transitions as projection for absorption (blue) and emission (red). GS and ES are colored blue and red, respectively.

So far, we had based our discussion merely on a single vibrational mode [Fig. 16]. However, for nonlinear many-atom molecules the *FC* factors of all 3*N*−6 normal modes must be considered. In many cases, the geometric differences between GS and ES can be described by a distortional coordinate as a combination of a small number of normal modes, so that the conclusions made above for a single mode remain valid. For example, a $t_{2g} \rightarrow e_g^*$ LF

transition in an octahedral TMC reduces the formal M–L bond order by depopulation of a rather nonbonding t_{2g} and occupation of a σ antibonding e_g* orbital [Fig. 2, 6, 13(a)]. The geometries at the GS and ES PES minima, with smaller and larger M–L bond lengths, respectively, are connected by the totally symmetric stretching vibration (a_{1g}) [Fig. 11, 13(a)]. Hence, only the *FC* factors of the a_{1g} vibrational mode must be calculated, while neglecting all other 3*N*−6−*1* normal modes. However, in this case, a *JT* distortion is additionally present, and additional modes must be included, for example the e_g modes for a tetragonal distortion of a *JT* active $^4T_{2g}$ state (vide supra, Fig. 11).

The interplay between excited state distortion and *Stokes* shift becomes obvious with the inspection of the absorption and emission spectra of $[Cr(ddpd)_2]^{3+}$. The *JT* distortion $Q_{\Gamma 0}$ and *JT* stabilization energy E_{JT} of the $^4T_{2g}$ state is seen experimentally by the *Stokes* shift of ca. 2400 cm^{-1} between $^4A_2 \rightarrow {}^4T_{2g}$ absorption, determined by MCD spectroscopy and fluorescence band, respectively [Fig. 17(a), S7, supplementary material].[2,21,28,81] Compared to the *JT* induced *Stokes* shift of 14000 cm^{-1} measured for the $^4T_{2g} \rightarrow {}^4A_{2g}$ fluorescence of $[Cr(CN)_6]^{3-}$ lacking chelating ligands,[146] the *Stokes* shift of $[Cr(ddpd)_2]^{3+}$ is substantially smaller. Consequently, both horizontal (*JT* distortion; $Q_{\Gamma 0}$) and vertical (*JT* stabilization; E_{JT}) displacements of the $^4T_{2g}$ PES are reduced in $[Cr(ddpd)_2]^{3+}$ as compared to $[Cr(CN)_6]^{3-}$, very likely due to the chelating nature of the ddpd ligand. In stark contrast, the *Stokes* shifts of the significantly sharper SF bands are much smaller with 80 cm^{-1} and <40 cm^{-1} for the $^2T_{1g}(1)$ and $^2E_g(1)$ state, respectively. These small numbers underpin the nested nature of SF states. The smaller ES distortion of the $^2E_g(1)$ state as determined from DFT calculations (vide supra) [Fig. 15] becomes experimentally obvious from the slightly smaller *Stokes* shift as for the $^2T_{1g}(1)$ state [Fig. 17(a), S7, supplementary material].[21,51] The appearance of three discernable SF absorption bands indicates a deviation of the $[Cr(ddpd)_2]^{3+}$ geometry from O_h symmetry lifting the $^2T_{1g}/^2E_g$ degeneracy. The red-NIR absorption spectrum can be fitted with five *Voigt* functions, representing the five $^2T_{1g}/^2E_g$ microstates [Fig. 17(b)].[51] Scaling of the CASSCF(7,12)-NEVPT2 energies by a factor of 0.88 of a series of (homo- and heteroleptic) *Molecular Rubies* excellently fits the experimental data of the fitted SF absorption bands, allowing the factorization of the *nephelauxetic effect* of ligands.[50,51]

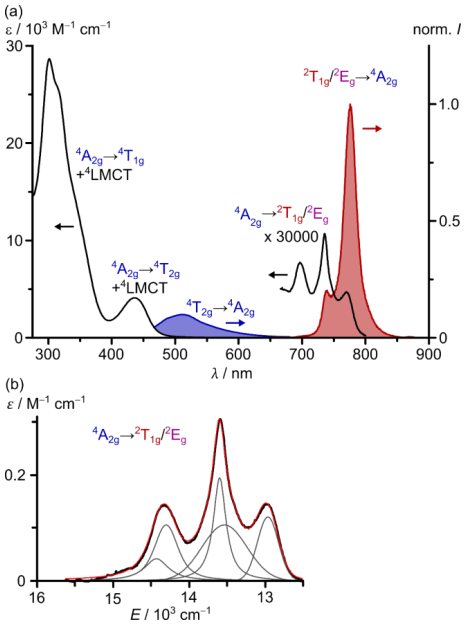

FIG. 17. (a) Absorption (black), fluorescence (blue, scaled to 0.1) and phosphorescence (red) spectra of $[Cr(ddpd)_2]^{3+}$ in solution and (b) baseline corrected NIR absorption spectrum (black) of $[Cr(ddpd)_2]^{3+}$ with sum fit (red) consisting of five *Voigt*

functions (gray). (a) adapted with permission from Advances in Inorganic Chemistry. Photochemistry and Photophysics of Earth-Abundant Transition Metal Complexes, edited by R. van Eldik, Vol. 83, p. 111 (2024). Copyright 2024, Elsevier.

Beyond the vibrational modes, that describe the distortion of ESs [Fig. 16(b)], so-called enabling modes can be required additionally for parity- (*Laporte*-)forbidden transitions. For example, LF transitions in centrosymmetric complexes, e.g. $t_{2g} \rightarrow e_g^*$ (O_h) in $[Cr(CN)_6]^{3-}$, are *Laporte*-forbidden with a vanishing electric transition dipole moment $\boldsymbol{\mu}$ [Eq. (25)].[8,108,133] Breaking the inversion symmetry by vibronic coupling with normal modes of *ungerade* symmetry enables mixing with orbitals (actually states) of *ungerade* symmetry, e.g. a p orbital admixture (u character) to the d orbital wavefunction (g character).[8,66] Hence, beyond the *Born-Oppenheimer* or *Condon* approximation with strict separation of electronic and nuclear degrees of freedom, suitable vibrations can open a path to nonadiabatic coupling or vibronic coupling. High molecular flexibility and the resulting low-energy vibrations favor vibronic coupling.

We now discuss the perturbational treatment of a *Laporte*-forbidden GS→ES absorption process with the two electronic wavefunctions ${\psi_1}^{(0)}$ (GS) and ${\psi_2}^{(0)}$ (ES). Assuming a weak dependence on nuclear coordinates, we employ the Hamiltonian used to describe the vibronic coupling of degenerate states – which in fact represents the *JT* problem [vide supra, Eq (9)]. The perturbation (of nondegenerate states) by vibronic coupling is now only considered for the final state ${\psi_2}^{(0)}$ (ES), which gives the first-order corrected wavefunction ${\psi_2}^{(1)}$ in analogy to Eq. (35) [Eq. (41)].[8] The electric transition dipole moment $\boldsymbol{\mu_{1\tilde{2}}}$ can be calculated between the GS and the vibronically perturbed ES from Eq. 42. [Eq. (S29), supplementary material].[8]

The formerly *Laporte*-forbidden ${\psi_1}^{(0)} \rightarrow {\psi_2}^{(0)}$ transition now gains intensity from allowed transitions ${\psi_1}^{(0)} \rightarrow {\psi_n}^{(0)}$, due to the vibronic admixture of states ${\psi_n}^{(0)}$ to the ES ${\psi_2}^{(0)}$. This admixture is induced by the vibronic coupling matrix element weighted by the electric transition dipole moments ${a_n}^* \boldsymbol{\mu_{1n}}$.[8] The zeroth-order element $\boldsymbol{\mu_{12}}$ refers to the *FC* approximation, when considering the *FC* factors [Eq. (39), (40), (42)] and the first-order elements refer to the vibronic coupling.

$$\psi_2{}^{(1)} = \psi_2{}^{(0)} + \sum_{n\neq 2} \frac{\sum_i Q_i \left\langle \psi_n{}^{(0)} \left| \frac{\partial \hat{\boldsymbol{H}}}{\partial Q_i} \right|_{\boldsymbol{Q}=\boldsymbol{0}} \right| \psi_2{}^{(0)} \right\rangle}{E(\psi_2{}^{(0)}) - E(\psi_n{}^{(0)})} \psi_n{}^{(0)} = \psi_2{}^{(0)} + \sum_{n\neq 2} a_n \psi_n{}^{(0)} \quad (41)$$

with $\boldsymbol{Q}\hat{\boldsymbol{H}}^{(1)} = \sum_i \frac{\partial \hat{\boldsymbol{H}}}{\partial Q_i}\Big|_{\boldsymbol{Q}=\boldsymbol{0}} Q_i$. [Eq. (9)].

$$\boldsymbol{\mu_{1\tilde{2}}} = \langle \psi_2{}^{(1)} | \hat{\boldsymbol{\mu}} | \psi_1{}^{(0)} \rangle = \boldsymbol{\mu_{12}} + \sum_{n\neq 2} {a_n}^* \langle \psi_n{}^{(0)} | \hat{\boldsymbol{\mu}} | \psi_1{}^{(0)} \rangle = \sum_{n\neq 2} {a_n}^* \boldsymbol{\mu_{1n}} \quad (42)$$

with $\boldsymbol{\mu_{12}} = 0$ for parity- or *Laporte*-forbidden transitions.

Symmetry considerations can help to identify the required allowed transitions between ${\psi_1}^{(0)}$ and ${\psi_n}^{(0)}$ and the vibronic coupling of ${\psi_2}^{(0)}$ with ${\psi_n}^{(0)}$. The electric transition dipole moments $\boldsymbol{\mu_{1n}} = \langle \psi_n{}^{(0)} | \hat{\boldsymbol{\mu}} | \psi_1{}^{(0)} \rangle$ are nonzero if the direct product of the irreducible representations $\Gamma_1 \times \Gamma_{\hat{\boldsymbol{\mu}}} \times \Gamma_n$ of the electronic states 1 and *n* and the dipole moment operator $\Gamma_{\hat{\boldsymbol{\mu}}}$ contains the totally symmetric irreducible representation A_{1g} or equivalent. The reader might note the analogy to the *JT* problem (vide supra).[8] The coefficients a_n are nonzero if the matrix elements $\left\langle \psi_n{}^{(0)} \left| \frac{\partial \hat{\boldsymbol{H}}}{\partial Q_i}\right|_{\boldsymbol{Q}=\boldsymbol{0}} \right| \psi_2{}^{(0)} \right\rangle$ in Eq. (41) are nonzero. The Hamiltonian $\hat{\boldsymbol{H}}$ [Eq. (9)] transforms as A_{1g}, so that $\sum_i \frac{\partial \hat{\boldsymbol{H}}}{\partial Q_i}\Big|_{\boldsymbol{Q}=\boldsymbol{0}} Q_i$ transforms as A_{1g} as well. Hence, $\frac{\partial \hat{\boldsymbol{H}}}{\partial Q_i}\Big|_{\boldsymbol{Q}=\boldsymbol{0}}$ belongs to the same irreducible representation Γ_i as the normal mode with normal coordinate Q_i. The direct product of irreducible representations $\Gamma_n \times \Gamma_i \times \Gamma_2$ of the electronic states n and 2 and the normal mode i contains the totally symmetric irreducible representation A_{1g} or equivalent enabling vibronic coupling.

Exemplary, we discuss the ${}^4A_{2g} \rightarrow {}^4T_{2g}$ transitions of a chromium(III) complex in the O_h point group. With the dipole moment operator $\hat{\boldsymbol{\mu}}$ transforming as T_{1u}, these transitions are *Laporte*-forbidden as the product $T_{2g} \times T_{1u} \times A_{2g} = A_{1u} + E_u + T_{1u} + T_{2u}$ does not contain the irreducible representation A_{1g}. Intensity can be borrowed only from states n of *ungerade* parity with nonzero $\boldsymbol{\mu_{1n}}$, according to the *parity* selection rule. Consequently, the ${}^4T_{2g}$ state must vibronically mix with states of *ungerade* parity u, which is only possible for vibrational modes of *ungerade* parity

u according to the matrix elements in Eq. (41). To have a chance of obtaining A_{1g}, the direct product must be of *gerade* parity, following from u(state n) × u(vibrational mode) × g(T_{2g}) = g(A_{1g}). Assuming an ML_6 complex with seven atoms and hence 15 normal modes that transform as a_{1g}, e_g, 2 t_{1u}, t_{2g} and t_{2u} in O_h, the t_{1u} and t_{2u} normal modes enable vibronic coupling and hence LF transitions. The electronic transition is accompanied by a vibrational transition of an *ungerade* normal mode (enabling mode) and the ES wavefunction at the *FC* geometry is no longer of pure d orbital character (g). Typically, only the lowest energy vibrational levels of *ungerade* symmetry have to be considered.[66] The 0-0 transition is not observed and the absorption bands are shifted hypsochromically by the 0-1 vibrational transition energy of the *ungerade* enabling mode(s).

The absorption and emission spectra of the three *Molecular Rubies* $[Cr(tpe)_2]^{3+}$, $[Cr(bpmp)_2]^{3+}$ and $[Cr(ddpd)_2]^{3+}$ [Scheme 1] are instructive: all LF transitions are in principle *Laporte*-forbidden and hence very weak. However, the molar absorption coefficients in the spectral region of the LF transitions increase from $[Cr(tpe)_2]^{3+}$, $[Cr(bpmp)_2]^{3+}$ to $[Cr(ddpd)_2]^{3+}$ [Fig. 17, 18, Scheme 1, Table S1, supplementary material]. $[Cr(tpe)_2]^{3+}$ is centrosymmetric and hence the transitions require intensity borrowing from *ungerade* states, while $[Cr(bpmp)_2]^{3+}$ and $[Cr(ddpd)_2]^{3+}$ possess no center of symmetry, intrinsically mitigating *Laporte's* rule. Additionally, $[Cr(ddpd)_2]^{3+}$ possesses parity-allowed ^{4}LMCT transitions in the spectral region of the LF transitions, further increasing the molar absorption coefficients in this spectral region. Analogous considerations apply to *Laporte*-forbidden emission bands, e.g. the $^2E_g \rightarrow {}^4A_{2g}$ and $^2T_{1g} \rightarrow {}^4A_{2g}$ transitions of octahedral chromium(III) complexes. The centrosymmetric complex $[Cr(tpe)_2]^{3+}$ indeed shows emission bands with a very rich vibrational fine structure that arises from *ungerade* enabling modes [Fig. 18(a)].[17,57] On the other side, the non-centrosymmetric complexes $[Cr(ddpd)_2]^{3+}$ or $[Cr(bpmp)_2]^{3+}$ display sharp (vibrationally unstructured) SF emission bands [Fig. 16(a), 17(b)].[2,17,18,21,51,53] The radiative rate constants for the SF PL observed experimentally for $[Cr(tpe)_2]^{3+}$, $[Cr(bpmp)_2]^{3+}$ and $[Cr(ddpd)_2]^{3+}$ of 19–20, 88–109 and 121–122 s^{-1} reflect the presence and absence of a center of symmetry, respectively [Table S1, supplementary material].[2,17,18,53] The *spin* selection rule is much stricter than *Laporte's* rule, when comparing the molar absorption coefficients of LF bands ($^4A_{2g} \rightarrow {}^4T_{2g}$, only *Laporte*-forbidden) with those of SF bands ($^4A_{2g} \rightarrow {}^2T_{1g}/{}^2E_g$, *Laporte*- and *spin*-forbidden) [Fig. 17(b), 18(a)].

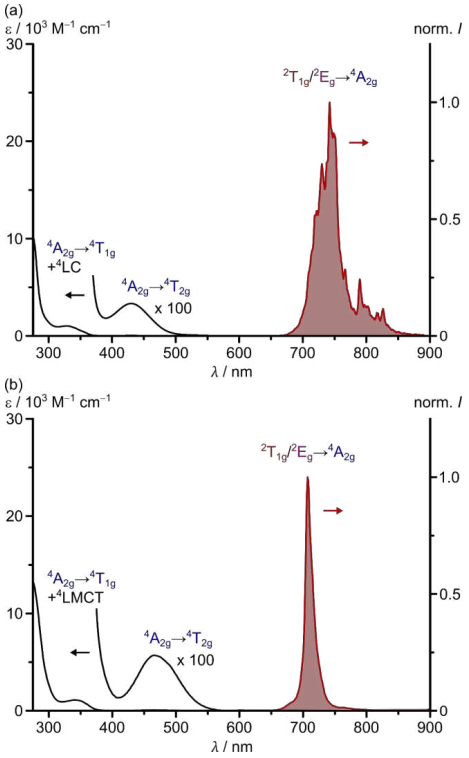

FIG. 18. Absorption (black) and emission spectra (red) of (a) $[Cr(tpe)_2]^{3+}$ and (b) $[Cr(bpmp)_2]^{3+}$ in solution.

IVB. Nonradiative transitions: internal conversion (IC), intersystem crossing (ISC) and multiphonon relaxation

Beside vertical transitions between electronic states, i.e. absorption or emission of a photon at constant nuclear coordinates, nonradiative processes – horizontal processes at constant energy, such as IC and ISC – play an important role in the ES dynamics. The rates of such processes can be obtained in the frame of *Fermi*'s golden rule.[147,148] Its formulation can be found in textbooks of quantum chemistry.[8,108,110,116,123,133] The rate of a nonradiative transition from state 1 to a continuum of states 2 with density of states $\rho(E)$ at energy $E_1 \approx E_2 = E$ can be calculated using *Fermi*'s golden rule. Conservation of energy requires that initial and final states have the same energy as no radiation is emitted. The Hamiltonian $\widehat{\boldsymbol{H}}_{\boldsymbol{1\rightarrow 2}}$ describes the coupling between states 1 and 2 [Eq. (43)]. Vibronic coupling drives IC and the Hamiltonian has the form of a nuclear kinetic operator $\widehat{\boldsymbol{T}}_{\boldsymbol{N}}$ for nuclear motion.[147] SOC drives ISC and the SOC Hamiltonian $\widehat{\boldsymbol{H}}_{\boldsymbol{SO}}$ is applied for ISC processes.[148–150]

This description assumes that the matrix coupling elements are the same for all final states at energy E [Eq. (43)]. A more general expression includes the sum over all final states, allowing for different coupling matrix elements [Eq. (44)]. For a degenerate final state, for example, the sum can be formed over the quantum numbers (index i). The *Dirac* delta function $\delta(E_1 - E_{2,i})$ takes care of the energy conservation [Eq. (44)].[123] The nonradiative rate constant for transitions from state 1 in vibrational level υ can be expressed within the *Condon* approximation, according to Eq. (45) with electron and nuclear wavefunctions $\psi_{n,i}\chi_{n,\upsilon}$ [Eq. (39)]. The last sum over all *FC* factors of final states describes the so-called *FC* weighted density of final states (FCWD) [Eq (45)].[148,149] The following discussion is based on horizontal transitions between an ES and the GS. Fully analogous descriptions pertain to horizontal transitions between two ESs as initial and final states.

$$k_{nr} = \frac{2\pi}{\hbar}\left|\langle\psi_2|\hat{\boldsymbol{H}}_{\mathbf{1\to 2}}|\psi_1\rangle\right|^2\rho(E) \quad (43)$$

$$k_{nr} = \frac{2\pi}{\hbar}\sum_i\left|\langle\psi_{2,i}|\hat{\boldsymbol{H}}_{\mathbf{1\to 2}}|\psi_1\rangle\right|^2\delta(E_1 - E_{2,i}) \quad (44)$$

$$k_{nr} = \frac{2\pi}{\hbar}\sum_i\left|\langle\psi_{2,i}|\hat{\boldsymbol{H}}_{\mathbf{1\to 2}}|\psi_1\rangle\right|^2\sum_{v'}\left|\langle\chi_{2,v'}|\chi_{1,v}\rangle\right|^2\delta(E_{1,v} - E_{2,i,v'}) = \frac{2\pi}{\hbar}\sum_i\left|\langle\psi_{2,i}|\hat{\boldsymbol{H}}_{\mathbf{1\to 2}}|\psi_1\rangle\right|^2 FCWD \quad (45)$$

The FCWD and hence the rate constant for nonradiative transitions k_{nr} depend exponentially on the energy difference ΔE of the adiabatic electronic states. This dependency is expressed by the energy gap law (EGL) by *Englman* and *Jortner*.[148,151] The EGL is valid to describe the nonradiative processes IC and ISC between different ESs and between the GS and ESs.[148,151] For harmonic potentials of the GS and ES with identical vibrational frequencies, two limiting cases of the ES distortion can be defined, namely the weak coupling limit (WCL, weak ES distortion, nested ES) and the strong coupling limit (SCL, strong ES distortion) [Fig. 19].[10,148]

In the WCL, the FCWD and hence k_{nr} scales with $k_{nr} \sim (\Delta E)^{-\frac{1}{2}}e^{-\Delta E}$, with $\Delta E = E_{ES} - E_{GS}$ being the ES-GS energy gap [Eq. (45), (46); Fig. 19(a), (b)].[148,151] Neglecting contributions of low-energy vibrations to k_{nr}, the maximum vibrational angular frequency ω_M of the normal mode with non-vanishing displacement ΔQ_M between GS and ES dominates. A normal mode with no ES-GS displacement leads to vanishing *FC* factors and hence no contribution to k_{nr}. A simplified form for k_{nr} in the WCL assumes the prefactor as constant (C_1) compared to the dominating exponential dependence on the ES energy so that $k_{nr} \sim e^{-\Delta E}$ [Eq. (47)] results.[151,152]

An interesting PES situation is observed for the two lowest-energy SF states $^2T_{1g}(1)$ and $^2E_g(1)$ of $[Cr(ddpd)_2]^{3+}$ (and other *Molecular Rubies*) and the IC process between these states. These states are essentially, but not exactly, nested (WCL) [Fig. 14, 15] and possess a very small energy gap of $\Delta E \approx 650$ cm^{-1}.[2,22] Likely, only one or two vibrational quanta are required to overcome this small energy gap. The DFT-calculated optimized geometries of $^2T_{1g}(1)$ and $^2E_g(1)$ states [Fig. 15] suggest that the combination of the totally symmetric a_{1g} and the e_g modes [cf. Fig. 11] connects these two PES. The small PES displacement ΔQ enables vibronic coupling that drives fast IC between these states [Fig. 19(c)]. Indeed, the $^2T_{1g}\rightarrow{}^2E_g$ IC, corresponding to a one-phonon process in the solid-state material ruby, was determined being in the order of 2.5 ns from $^2T_{1g}$ state pump experiments.[153,154] Hence, an equilibrium between these two ESs is established so that the PL lifetimes of the ESs are identical. The thermal population of these states follows a *Boltzmann* distribution. Consequently, the PL intensities of the two states vary with temperature and ratiometric *Boltzmann* thermometry[155] is realized with this unique PES landscape in ruby and a related oxynitridoborate as well as for the molecular congener $[Cr(ddpd)_2]^{3+}$.[22,156]

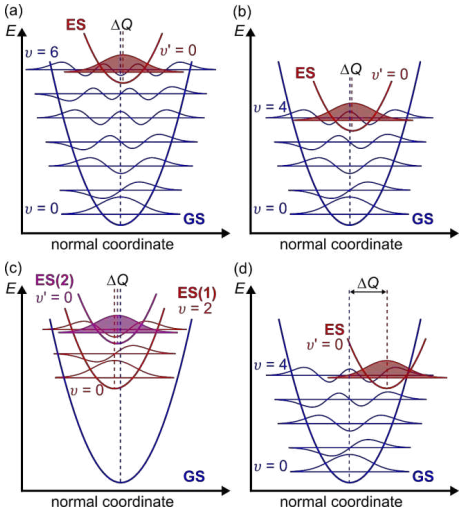

FIG. 19. Harmonic PES diagrams along a normal (distortional) coordinate with relevant vibrational wavefunctions (a) for nested high-energy ES (weak vibrational wavefunction overlap and weak coupling limit), (b) a lower-energy nested ES (strong vibrational wavefunction overlap and weak coupling limit), (c) two nested, close-lying excited states enabling ES(1) → ES(2) IC (strong vibrational wavefunction overlap and weak coupling limit) and (d) a low-energy, strongly distorted ES (strong vibrational wavefunction overlap and strong coupling limit). The GS and ESs are colored blue, red and purple, respectively.

$$FCWD = \frac{1}{\sqrt{2\pi\hbar\omega_M \Delta E}} e^{-\frac{\gamma\Delta E}{\hbar\omega_M}} \qquad (46)\ [\text{WCL}]$$

γ is a positive parameter.[151]

$$k_{nr} = C_1 \cdot e^{-\left(C_2 \cdot \frac{\Delta E}{\hbar\omega_M}\right)} \qquad (47)$$

In the SCL, the pronounced ES distortion ΔQ leads to a larger overlap of the GS and ES vibrational wavefunctions [Fig. 19(d)] and hence a faster nonradiative ES-GS transition.[151] The reorganization energy λ describes the extent of the ES distortion. *Marcus* theory connects λ with the activation barrier E_a for the ES/GS surface crossing [Fig. 20].[139–141] The FCWD for the SCL case is given by Eq. (48) in the low temperature regime, i.e. with the mean vibrational energy being smaller than the thermal energy ($\hbar\langle\omega\rangle < k_B T$, k_B: *Boltzmann* constant).[148,151] Eq. (48) is hence valid at room temperature. The dependence on the mean vibrational angular frequency $\langle\omega\rangle = N^{-1}\sum_i^N \omega_i$ indicates that isotope effects on k_{nr} are expected to be only moderate in the SCL. On the other hand, a single normal mode of maximum frequency dominates k_{nr} in the WCL and isotope effects can be substantial. In the SCL, the maximum rate constant k_{nr} occurs at vanishing E_a at $\lambda = \Delta E$ as $E_a = (\Delta E - \lambda)^2/4\lambda$ (*Marcus* normal region) [Fig. 20(a)].[148,151] At even larger distortions, an increase in the barrier E_a is observed (*Marcus* inverted region) [Fig. 20(b)]. At high temperature ($k_B T \gg \hbar\langle\omega\rangle$), k_{nr} is determined by the thermal energy and a semiclassical *Marcus*-type[139–141] behavior results [Eq. (49)–(53)].[148,151]

$$FCWD = \frac{1}{\sqrt{2\pi\lambda\hbar\langle\omega\rangle}} e^{-\frac{(\Delta E-\lambda)^2}{2\lambda\hbar\langle\omega\rangle}} \qquad (48)\ [\text{SCL}]$$

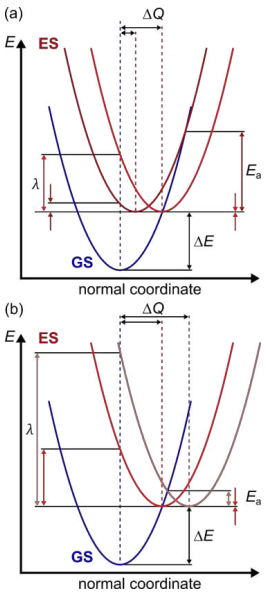

FIG. 20. Harmonic PES diagrams of the GS (blue) and ESs (red) along a normal (distortional) coordinate with increasing ES distortion ΔQ, described by increasing reorganization energy λ, lowering the activation barrier E_a for ES/GS surface crossing (a) in the *Marcus* normal region and (b) in the *Marcus* inverted region.

$$FCWD = \frac{1}{\sqrt{4\pi\lambda k_B T}} e^{-\frac{(\Delta E-\lambda)^2}{4\lambda k_B T}} \qquad (49)$$

In the WCL, the horizontal nonradiative ES to GS transition corresponds to a tunneling process, while in the SCL a direct surface crossing between the PES of ES and GS occurs.[151] Importantly, in the SCL and high temperature limit, k_{nr} depends on temperature and direct surface crossing becomes a thermally activated process. Assuming negligible changes in entropy, $\Delta E = -\Delta G^0$ in Eq. (49) transforms Eq. (45) into Eq (50) with H_{DA} being the electronic coupling matrix element between the two electronic states.[139–141] This *Marcus*-type[139–141] expression can be related to the *Arrhenius* equation [Eq. (51)] by identifying the pre-exponential factor A and the activation energy E_a according to Eq. (52) and (53).[157] Hence, an *Arrhenius* fit of $k_{\mathrm{nr}}(T)$ together with prior knowledge or estimation of ΔG^0 can give valuable information on the reorganization energy λ and the electronic coupling H_{DA} between the involved electronic states. For example, this connection has been exploited for the understanding of horizontal processes of electronically excited iron(II) complexes in the SCL, such as high-spin to low-spin ISC and ^{3}MLCT to ^{3}MC IC transitions.[157,158]

$$k_{nr}(T) = \frac{2\pi}{\hbar} \frac{|H_{DA}|^2}{\sqrt{4\pi\lambda k_B T}} e^{-\frac{(\Delta G^0+\lambda)^2}{4\lambda k_B T}} \qquad (50)$$

$$k_{nr}(T) = A e^{-\frac{E_a}{k_B T}} \qquad (51)$$

$$A = \frac{2\pi}{\hbar} \frac{|H_{DA}|^2}{\sqrt{4\pi\lambda k_B T}} \qquad (52)$$

$$E_a = \frac{(\Delta G^0+\lambda)^2}{4\lambda} \qquad (53)$$

We now inspect deactivating vibrational modes of instructive examples in the WCL. C–H stretching vibrations have been identified as deactivating modes $\hbar\omega_M$ (≈3000 cm^{-1}) for aromatic hydrocarbons with weakly distorted π-π* ESs (WCL). A substantial isotope effect arises upon deuteration with C–D stretching vibrations (≈2200 cm^{-1}) becoming the deactivating modes $\hbar\omega_M$ [Eq. (45), (46)].[151] In contrast, ^{3}MLCT ESs of polypyridine osmium(II) complexes in the WCL deactivate to the GS via ring-breathing modes of the pyridine ligands (≈1300 cm^{-1}) with only small C–H/C–D isotope effects.[159] The intraconfigurational SF states of chromium(III) complexes are very weakly distorted (vide supra) and the WCL for nonradiative deactivation applies. In a series of SF luminescent chromium(III) complexes $[Cr(bpi^{R1/R2})_2]^+$ with anionic pincer-type ligands and varying PL energy ΔE, the experimentally determined nonradiative rate constants k_{nr} [Eq. (22)] correlate with the SF PL energy ΔE giving a low-frequency deactivating mode $\hbar\omega_M$ [Eq. (47), Scheme 1, Table S1, supplementary material].[160,161] The metal-confined nature of the SF state wavefunctions requires deactivating modes $\hbar\omega_M$ that involve the metal-ligand bonds. Hence, the deactivating modes, representing the ES distortion, were tentatively assigned to Cr–N(imido) stretching vibrations (≈560 cm^{-1}).[160] The excited state distortion was attributed to admixture of ^{2}LMCT state character to the nested SF state in the related $[Cr(dpc)_2]^+$ complex [Scheme 1, Table S1, supplementary material].[54] To contribute to k_{nr}, a mode $\hbar\omega_M$ must lead to a non-vanishing displacement ΔQ_M resulting in non-vanishing *FC* factors.[151] In contrast to π-π* ESs of aromatic hydrocarbons, C–H displacement in the ligands of TMCs can be expected to be very weak to negligible for MLCT and MC states (e.g. SF states), respectively. Consequently, ligand deuteration of TMCs with MLCT ESs should lead only to small kinetic isotope effects. Ligand deuteration of TMCs with metal-centered ESs should have essentially no effect on k_{nr}. However, strong C–H/C–D and N–H/N–D isotope effects were observed for k_{nr} of the *Molecular Rubies* $[Cr(ddpd)_2]^{3+}$, $[Cr(bpmp)_2]^{3+}$ and $[Cr(H_2tpda)_2]^{3+}$/$[Cr(D_2tpda)_2]^{3+}$, respectively [Scheme 1, Table S1, supplementary material].[20,53,162] This phenomenon will be discussed below in more detail.

Beyond the *Condon* approximation, vibronic coupling induces nonradiative (IC, ISC) and radiative processes (fluorescence, phosphorescence). Direct vibronic coupling between an initial and a final state can be described by a *Taylor* expansion of the SOC matric element, truncated at first (*Herzberg-Teller*, *HT*) or higher orders.[148–150] A singlet→triplet ISC transition $S_1 \rightarrow T_1^\alpha$, with $\alpha = x, y, z$ denoting the three spin sublevels, serves to demonstrate the vibronic coupling. The spin-orbit coupling matrix element (SOCME) $\langle S_1 | \widehat{\boldsymbol{H}}_{\boldsymbol{SO}} | T_1^\alpha \rangle|_{\boldsymbol{Q}=\boldsymbol{0}}$ at a reference configuration $\boldsymbol{Q} = \boldsymbol{0}$ [Eq. (54)] describes the ISC process and the singlet and triplet wavefunctions S_1 and T_1^α have the form $\psi_n \chi_{n,v}$ with electron and nuclear wavefunctions according to Eq. (39). The first term in

the *Taylor* expansion at $\boldsymbol{Q} = \boldsymbol{0}$ describes the direct SOC (*Condon* approximation, vide supra) and the second term the vibronic spin-orbit interaction (*HT*) [Eq. (54)].[148–150]

$$\langle S_1|\widehat{\boldsymbol{H}}_{\boldsymbol{SO}}|T_1^\alpha\rangle = \langle S_1|\widehat{\boldsymbol{H}}_{\boldsymbol{SO}}|T_1^\alpha\rangle\big|_{\boldsymbol{Q}=\boldsymbol{0}} + \sum_i \frac{\partial\langle S_1|\widehat{\boldsymbol{H}}_{\boldsymbol{SO}}|T_1^\alpha\rangle}{\partial Q_i}\Big|_{\boldsymbol{Q}=\boldsymbol{0}} Q_i \quad (54)$$

Finally, indirect vibronic coupling is achieved by spin-vibronic coupling allowing SOC of S_1 and T_1^α with intermediate triplet T_m^α and singlet S_n states, respectively [Eq. (55)].[148–150] This approach is analogous to the intensity borrowing in phosphorescence processes by replacing the dipole moment operator $\widehat{\boldsymbol{\mu}}$ with the first-order term of the *Taylor* expansion in $\boldsymbol{Q} = \boldsymbol{0}$ of the electronic Hamiltonian $\boldsymbol{Q}\widehat{\boldsymbol{H}}^{(\boldsymbol{1})} = \sum_i \frac{\partial\widehat{\boldsymbol{H}}}{\partial Q_i}\big|_{\boldsymbol{Q}=\boldsymbol{0}} Q_i$ representing the vibronic coupling [Eq. (9)].[149] In this approach, singlet state character S_n is mixed to the triplet state T_1^α via SOC $\langle S_n|\widehat{\boldsymbol{H}}_{\boldsymbol{SO}}|T_1^\alpha\rangle$ with the vibronic coupling between S_n and S_1 states being introduced by $\langle S_1|\boldsymbol{Q}\widehat{\boldsymbol{H}}^{(\boldsymbol{1})}|S_n\rangle$. A direct vibronic coupling between unperturbed S_1 and T_1^α states is impossible as $\langle S_1|\boldsymbol{Q}\widehat{\boldsymbol{H}}^{(\boldsymbol{1})}|T_1^\alpha\rangle = 0$. Hence, T_1^α and S_1 states are indirectly vibronically coupled via intermediate singlet states S_n in the first term and via triplet states T_m^α in the second term [Eq. (55)].[149]

$$\langle\tilde{S}_1|\boldsymbol{Q}\widehat{\boldsymbol{H}}^{(\boldsymbol{1})}|\tilde{T}_1^\alpha\rangle = \sum_n \frac{\langle S_n|\widehat{\boldsymbol{H}}_{\boldsymbol{SO}}|T_1^\alpha\rangle}{E(T_1)-E(S_n)}\langle S_1|\boldsymbol{Q}\widehat{\boldsymbol{H}}^{(\boldsymbol{1})}|S_n\rangle + \sum_m \frac{\langle T_m^\alpha|\widehat{\boldsymbol{H}}_{\boldsymbol{SO}}|S_1\rangle^*}{E(S_1)-E(T_m)}\langle T_m^\alpha|\boldsymbol{Q}\widehat{\boldsymbol{H}}^{(\boldsymbol{1})}|T_1^\alpha\rangle \quad (55)$$

The qualitative *El-Sayed* rules provide a convenient estimation of the nonradiative transition probability between states of different spin multiplicity.[163] These rules have been generalized by *Marian*.[148] In a simple one-electron picture in the *Condon* approximation, ISC will be fast if a change in spin is accompanied by a change in orbital occupation so that the total angular momentum is conserved provided that the conditions given in Table 7 are met.[148] With respect to metal-centered ISC transitions, the generalized *El-Sayed* rules provide combinations of d orbitals that enable couplings and hence fast ISC [Table 8]. Details of this derivation are collected in the supplementary material [Eq. (S30)–(S51)].[144,145,148] The rotation properties of the angular momentum components decide whether SOC is operative between the wavefunctions. These rules from the one-electron picture can be transferred to electronic states using group theory and character tables.[8]

SOC-CASSCF(7,12)-NEVPT2 calculations[28,51] for $[Cr(ddpd)_2]^{3+}$ deliver a large SOC constant (SOCC)[164] of 315 cm^{-1} between $^2T_{1g}(1)$ $[(d_{xy})^1(d_{yz})^2]$ and $^4T_{2g}(2)$ $[(d_{xy})^1(d_{yz})^1(d_{z2})^1]$ states [Table 9]. Indeed, this large SOCC can be rationalized by the generalized *El-Sayed* rules for ISC transitions between MC states [Table 8]. The change in orbital occupation corresponds to a one-electron excitation $d_{yz}\leftrightarrow d_{z2}$ [Fig. 5] with an *El-Sayed*-allowed change in magnetic quantum number $m_l = \pm 1$ [Table 8]. In contrast, $(d_{xy}/d_{yz})\leftrightarrow(d_{x2-y2}/d_{xz})$ double-excitation or retaining orbital occupations $(d_{xy}\leftrightarrow d_{xy})$ lead to small SOCCs for the $^2T_{1g}(1)/^4T_{2g}(1)$ $[(d_{xy})^1(d_{yz})^2]/[(d_{xz})^1(d_{yz})^1(d_{x2\text{-}y2})^1]$ and $^2E_g(1)/^4A_{2g}$ $[(d_{xy})^1(d_{xz})^1(d_{yz})^1]/[(d_{xy})^1(d_{xz})^1(d_{yz})^1]$ state combinations, respectively [Fig. 5, Table 9].

Table 7. Generalized *El-Sayed* rules.

Requirements for a fast ISC process between two states/electron configurations:

1. The transition corresponds to a one-electron excitation, a formal one-electron shift.
2. The transition is local, i.e. between orbitals with coefficients on same atoms.
3. The local angular momentum l must be conserved ($\Delta l = 0$) with change in magnetic quantum number m_l of $\Delta m_l = \begin{cases} 0 \; for \; m_l \neq 0 \\ \pm 1 \end{cases}$.
4. The total Spin S changes by $\Delta S = \pm 1$.

Table 8. Cartesian d orbitals with change in magnetic quantum numbers Δm_l for allowed couplings according to the generalized *El-Sayed* rules.

	d_{xy}	d_{yz}	d_{z2}	d_{xz}	d_{x2-y2}
d_{xy}		±1		±1	0
d_{yz}	±1		±1	0	±1
d_{z2}		±1		±1	
d_{xz}	±1	0	±1		±1
d_{x2-y2}	0	±1		±1	

Table 9. SOC constants (SOCCs) as square root of the sum of the squares of SOC matrix elements (SOCME) in cm^{-1} between doublet states and the $^4T_{2g}$-derived states of $[Cr(ddpd)_2]^{3+}$ from SOC-CASSCF(7,12)-NEVPT2 calculations. Large and medium SOCCs are highlighted in red and orange, respectively.

	$^4A_{2g}$	$^4T_{2g}(1)$	$^4T_{2g}(2)$	$^4T_{2g}(3)$
$^2T_{1g}(1)$	64	46	315	262
$^2T_{1g}(2)$	39	157	111	2
$^2T_{1g}(3)$	31	125	19	198
$^2E_g(1)$	0	336	164	179
$^2E_g(2)$	1	31	169	91
$^2T_{2g}(1)$	331	113	129	2
$^2T_{2g}(2)$	321	141	20	144
$^2T_{2g}(3)$	325	11	81	147

Excitation of $[Cr(ddpd)_2]^{3+}$ at 435 nm initially leads mainly to the population of the ^{4}LMCT state compared to the $^4T_{2g}$ state, according to *Laporte's* rule [Fig. 17(a)]. Several photophysical pathways to the $^2T_{1g}/^2E_g$ state manifold are conceivable [Fig. 21].[28] $^4T_{2g}\leftrightarrow{}^4$LMCT and ^{2}LMCT$\rightarrow{}^2T_{1g/2g}$ IC might be slow and fast, respectively, as these transitions are two- and one-electron transitions, respectively. Again, *El-Sayed* rules give a rationale for the relative rates of ISC processes. ^{4}LMCT$\rightarrow{}^2$LMCT ISC might be rather slow due to the retained orbital occupation. ^{4}LMCT$\rightarrow{}^2T_{1g/2g}/^2E_g$ ISC should be less efficient as well due to violating rule 2 [Table 7].[148]

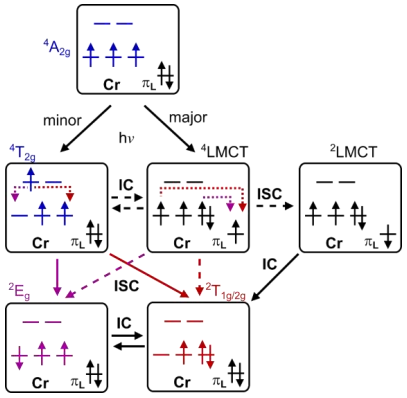

Fig. 21. Possible quartet→doublet ISC and IC pathways with representative microstates. Solid and dashed arrows indicate efficient and less efficient ISC and IC processes, respectively. Dotted arrows indicate the changes in orbital occupations for ISC processes indicated by the respective color. Adapted with permission from Advances in Inorganic Chemistry. Photochemistry and Photophysics of Earth-Abundant Transition Metal Complexes, edited by R. van Eldik, Vol. 83, p. 111 (2024). Copyright 2024, Elsevier.

We now apply group theory to metal-centered ISC transitions in an octahedral chromium(III) complex considering the lowest-energy quartet states $^4A_{2g}$, $^4T_{2g}$ and $^4T_{1g}$. In O_h symmetry, the rotation transforms as T_{1g}. The direct products of the irreducible representation of the rotation with the representations of the lowest quartet states $^4A_{2g}$, $^4T_{2g}$ and $^4T_{1g}$ yields the irreducible representations of doublet states capable of SOC [Table 10]. According to SOC matrices and Table 9,[165,166] SOC can be operative between $^4A_{2g}/^2T_{2g}$, $^4T_{2g}/^2E_g$,$^2T_{1g}$,$^2T_{2g}$ and $^4T_{1g}/(^2E_g)$,$^2T_{1g}$,$^2T_{2g}$ state combinations. SOC between these states mediates both ISC and phosphorescence. This SOC coupling signature in O_h symmetry is retained also for complexes with slightly lower symmetry, such as $[Cr(ddpd)_2]^{3+}$ with strong $^4A_{2g}/^2T_{2g}$ and $^4T_{2g}/^2E_g$,$^2T_{1g}$ (> 300 cm^{-1}) and medium $^4T_{2g}/^2T_{2g}$ (> 150 cm^{-1}) SOC as derived from SOC-CASSCF(7,12)-NEVPT2 calculations [Table 9].[28,51] This finding agrees with the fast quartet-doublet ISC processes $^4T_{2g}$ to $^2T_{2g}$,^2E_g,$^2T_{1g}$ observed in *Molecular Rubies*, which are often faster than the instrument resolution (< 200 fs).[21,28,43] For $[Cr(ddpd)_2]^{3+}$ the $^4T_{2g}$-derived states are close in energy to the $^2T_{2g}$-derived states allowing for fast

ISC already in the *FC* region mediated by SOC [Fig. 3, second quartet-doublet crossing point, highlighted with a circle]. Similarly, fast SOC-mediated $^4T_{2g} \rightarrow {}^2T_{1g}$ ISC is observed for $Cr(acac)_3$ [Scheme 1] due to surface crossing in the *FC* region ($\tau_{ISC} = 50$ fs; $k_{ISC} = 2.0\times10^{13}$ s^{-1}) [Scheme 1, Fig. 3, first quartet-doublet crossing point, highlighted with a square].[167,168] On the other hand, the ISC rate constants for $[Cr(bpmp)_2]^{3+}$ and $[Cr(btmp)_2]^{3+}$ with intermediate ligand field strengths at the *FC* geometry are smaller with $k_{ISC} = 1.9\times10^{12}$ s^{-1} and 1.2×10^{12} s^{-1} ($\tau_{ISC} = 540$ fs and 823 fs), respectively [Scheme 1].[44,169] More data are, however, required to generalize this apparent trend with fast SOC-mediated ISC to doublet states close to the *FC* region providing a high density of states (*Fermi's* golden rule). Yet even with $k_{ISC} = 1.9\times10^{12}$ s^{-1}, $[Cr(bpmp)_2]^{3+}$ achieves a very high ISC quantum yield of >92.5%, possibly because fluorescence from $^4T_{2g}$ states as a potentially competitive process to ISC is slow due to *Laporte's* rule.[44]

Table 10. Direct products between the irreducible representations of the quartet states $^4A_{2g}$, $^4T_{2g}$ and $^4T_{1g}$ of d^3 TMCs with the irreducible representation of rotation (T_{1g}) in the O_h point group.

$A_{2g} \times T_{1g}(rot.) = T_{2g}$
$T_{2g} \times T_{1g}(rot.) = A_{2g} + E_g + T_{1g} + T_{2g}$
$T_{1g} \times T_{1g}(rot.) = A_{1g} + E_g + T_{1g} + T_{2g}$

SOC between the nested SF states (^2E_g, $^2T_{1g}$) and the $^4T_{2g}$ states in principle allows for thermally activated bISC. The SOCCs vary along the *JT* coordinates (Q_Γ) of the $^4T_{2g}$-derived states and in the $^2E_g, {}^2T_{1g} \rightarrow {}^4T_{2g}$ transition states. The nested SF state geometries can be approximated by the *FC* geometry. The resulting $^2E_g, {}^2T_{1g} \rightarrow {}^4T_{2g}$ bISC rate $k_{bISC}(T)$ then depends on the activation barriers $E_a(bISC)$ along the *JT* coordinates Q_Γ in the SCL and the electronic coupling matrix element H_{DA}, with SOC as electronic coupling mechanism in this case [Fig. 20, 22, Eq. (50)–(53)]. The activation barriers $E_a(bISC)$ are determined by the $^4T_{2g}$/SF state energy gaps ΔE and the reorganization energy λ [Fig. 22]. The latter corresponds to the *JT* stabilization energy $\lambda = E_{JT}$, which scales with the degree of the *JT* distortion (ΔQ_{JT}) [Fig. 10, 22]. Large $^4T_{2g}$/SF state energy gaps at the *FC* geometry $\Delta E_{FC} = E_{JT} + \Delta E$ and a small ΔQ_{JT} arising from a large ligand field splitting Δ_o and a rigid environment, respectively, lead to a small E_{JT}, with $\Delta E_{FC} = \Delta E$ as the limiting case. Hence, a large ligand field splitting and a rigidified system can slow down the detrimental bISC process that reduces the SF PL quantum yield. This is perfectly realized in the solid-state material ruby $Al_2O_3:Cr^{3+}$ explaining its high SF PL quantum yield.

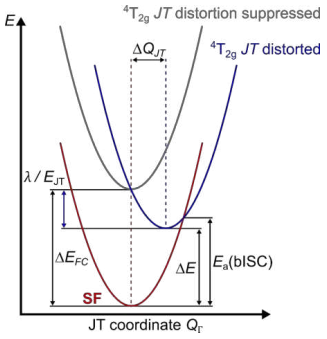

FIG. 22. Harmonic PES diagram of the $^4T_{2g}$ state, *JT* distorted (blue) and undistorted (suppressed *JT* distortion, gray) and of an SF state along the *JT* distortional coordinate Q_Γ with *JT* distortion ΔQ_{JT}, reorganization/*JT* stabilization energy $\lambda = E_{JT}$, bISC barrier $E_a(bISC)$, energy differences ΔE_{FC} and ΔE between SF state and $^4T_{2g}$ state at the *FC* geometry and at the *JT* distorted geometry, respectively.

Interestingly, SOC between the SF states (^2E_g, $^2T_{1g}$) and the GS ($^4A_{2g}$) of octahedral chromium(III) complexes is very small [Tables 9 and 10], suggesting that ISC will be slow also from the SOC perspective, in addition to the parity penalty for k_r of the phosphorescence and the penalty from the almost nested PESs for k_{nr} (vide supra). These effects together account for a large part of the enormous SF state lifetimes of *Molecular Rubies* of up to $\tau = 3.5$ ms.[39]

A heavy atom effect has been observed when bridging oxygen atoms are replaced by bridging sulfur atoms in $[Cr(bpop)_2]^{3+}$ to give $[Cr(bptp)_2]^{3+}$ [Scheme 1]. The nonradiative rate constant k_{nr} dramatically increases by orders of magnitude from 1059 to 606000 s^{-1} and k_r approximately halves from 138 to 61 s^{-1}.[51] An *Arrhenius* study finds that the pre-exponential factor of $[Cr(bptp)_2]^{3+}$ is larger by almost five orders of magnitude. SOC in this complex might be increased by indirect vibronic coupling with low-energy LMCT states that have large orbital contributions from the sulfur atoms. This indirect vibronic coupling with LMCT states might in principle apply to bISC from SF states to $^4T_{2g}$-derived states and to ISC from the SF states to the $^4A_{2g}$ GS. However, as the radiative rate constant for the SF $\rightarrow$ $^4A_{2g}$ process has not increased, the influence of the sulfur atoms on the bISC process is more pronounced.[51] On the other hand, incorporation of four iodine atoms in the ligand periphery in $[Cr(Mebipzp)_2]^{3+}$, yielding $[Cr(IMebipzp)_2]^{3+}$, increases k_r from 74 to 288 s^{-1} (factor of 3.9), and simultaneously increases k_{nr} to a similar extent from 738 to 2900 s^{-1} (factor 3.9) [Scheme 1, Table S1, supplementary material]. This suggests that the four iodine atoms at these positions affect the SF $\rightarrow$ $^4A_{2g}$ ISC and phosphorescence to a similar extent via SOC.[170]

Beyond SOC-mediated ISC and bISC, the low energy of the SF states opens different nonradiative relaxation pathways, namely via the so-called Inductive-Resonant Mechanism (IRM) of nonradiative transitions.[152,171,172] Within this treatment, the ES energy is transferred to overtones of high-energy oscillators (e.g. C–H, N–H, O–H overtones) of the environment, e.g. of the ligands and/or the solvent, via an electric dipole-dipole interaction with multiphonon relaxation.[152,171,172] This mechanism is conceptually similar to the *Förster* Resonance Energy Transfer (FRET)[173] describing the Coulombic nonradiative EnT between different *electronic* states.[9,10] For a single oscillator, the nonradiative rate constant k_{nr} is given by Eq. (56) in the IRM.[152,171,172]

$$k_{nr} = \frac{9000 \cdot ln(10) \kappa^2}{128 \pi^5 N_A} \cdot \frac{k_r}{n^4 r^6} \cdot SOI = 5.857 \cdot 10^{-25} \frac{k_r}{n^4 r^6} \cdot SOI \qquad (56)$$

κ^2 denotes an orientation factor of dipoles amounting to $\frac{2}{3}$ in the dynamic isotropic limit, N_A *Avogadro*'s constant, n the refractive index of the medium and k_r the radiative rate constant of the photoluminescent molecule. The most decisive factors in Eq. 56 are the distance r (in cm) between the central ion (for an ES wavefunction centered on the central ion) and the oscillator (the molecular entity involved in the vibration) and the spectral overlap integral SOI on a wavenumber scale (cm^{-1}) with the unit M^{-1} cm^3 [Eq (57)].[152,171,172]

$$SOI = \int \frac{I_{norm}(\tilde{\nu}) \varepsilon_{vib}(\tilde{\nu})}{\tilde{\nu}^4} d\tilde{\nu} \quad (57)$$

The SOI is given by the integral over the product of the area-normalized emission intensity $I_{norm}(\tilde{\nu})$ [Eq. (58)] and the decadic molar absorption coefficient $\varepsilon_{vib}(\tilde{\nu})$ (in M^{-1} cm^{-1}) of the oscillator scaled by $\tilde{\nu}^{-4}$.[152,171,172] The overall multiphonon relaxation rate k_{nr} is obtained by summation over the contributions of all oscillators.[152,171,172] As the molar absorption coefficient $\varepsilon_{vib}(\tilde{\nu})$ rapidly decreases for higher vibrational overtones and as the SOI depends on $\tilde{\nu}^{-4}$, the SOI and hence IRM become only relevant for low-energy PL.

$$I_{norm} = \frac{I_{em}(\tilde{\nu})}{\int I_{em}(\tilde{\nu}) d\tilde{\nu}} \qquad (58)$$

SF PL from chromium(III) complexes typically occurs at energies below 700 nm (14285 cm^{-1}). Consequently, the SOI with high-energy oscillators and hence IRM can become significant. For $[Cr(ddpd)_2]^{3+}$ with PL at 775 and 738 nm, the inductive-resonant EnT from the SF ($^2T_{1g}/^2E_g$) states to vibrational overtones of C–H groups of the pyridine donors is accidentally not very effective. Rather small SOIs with the third and fourth C–H overtones ν^4 and ν^5 is one reason for its comparably small k_{nr} and the resulting long SF state lifetime $\tau_{RT} = 1.1$ ms [Fig. 23]. Statistical deuteration of the ddpd ligand raises the luminescence lifetime of $[Cr([D_9]\text{-ddpd})_2]^{3+}$ even further to $\tau_{RT} = 2.3$ ms [Scheme 1, Table S1, supplementary material].[20] With the deuterated ddpd ligand, the only significant, but even smaller SOI of the $^2T_{1g}/^2E_g$ emission bands arises with the fifth C–D overtone ν^6, which has a much smaller molar absorption coefficient $\varepsilon_{vib}(\tilde{\nu})$ [Fig. 23].[20] By reducing k_{nr} via the IRM, the PL quantum yield increases from $\Phi_{em} = 13.7\%$ to 30.1% in acetonitrile and d_3-acetonitrile, respectively (factor ≈2.2).[18,20] Similarly, the PL lifetime and PL quantum yield of $[Cr(bpmp)_2]^{3+}$ increase by deuteration of the α-positions of the bpmp ligand from 1.8 ms to 2.5 ms and from 19.6% to 24.6%, respectively (factor ≈1.3) [Scheme 1, Table S1, supplementary material].[53] The smaller isotope effect for $[Cr(bpmp)_2]^{3+}$ likely arises from the higher PL energy (709 nm, 14100 cm^{-1}) and the resulting smaller SOI with the third C–H overtone ν^4, so that the gain from

deuteration is less prominent.[53] Deuteration of the CH_2 bridges of the bpmp ligand to CD_2 moieties also increases the PL lifetime and quantum yield, but merely from 1.55 ms to 1.8 ms and from 15.8% to 19.6%, respectively (factor ≈1.2). A small solvent isotope effect (H_2O/D_2O) might also contribute to the observed overall effect here.[53] In addition to the higher PL energy of $[Cr(bpmp)_2]^{3+}$, the larger distance r of this C–H oscillator at the bridge to the chromium center might explain the rather small effect. The C–H overtone energies for CH, CH_2 and CH_3 units have been estimated so that "C–H overtone-free" spectral regions with minor nonradiative decay via IRM can be identified.[48]

Only small solvent isotope effects on PL lifetimes and PL quantum yields are typically observed for the SF PL of chromium(III) complexes. The strong distance dependence of $k_{nr} \sim r^{-6}$ [Eq. (56)] might account for this weak effect, as the metal center is well shielded from solvent molecules by the coordinating ligands. Similar to the CH→CD isotope exchange, NH→ND deuteration of the bridge in $[Cr(H_2tpda)_2]^{3+}/[Cr(D_2tpda)_2]^{3+}$ including a significant solvent isotope effect (H_2O/D_2O) increases the PL lifetime and quantum yield from 0.67 ms to 1.5 ms and from 6.3% to 15.2%, respectively (factor ≈2) [Scheme 1, Table S1, supplementary material].[162]

This significant enhancement highlights the high quenching efficiency of N–H oscillators (free N–H: 3400 cm^{-1}) that arises from the very broad and intense vibrational N–H bands that can give rise to large SOIs.[162] k_{nr} decreases dramatically upon deuteration for amine and heteroleptic ammine-aqua chromium(III) complexes, e.g. $[Cr(NH_3)_6]^{3+}/[Cr(ND_3)_6]^{3+}$ (factor ≈600), $[Cr(en)_3]^{3+}/[Cr([D_4]\text{-}en)_3]^{3+}$ (factor ≈600), $[Cr(ND_3)_{6-n}(H_2O)_n]^{3+}$ and $[Cr(NH_3)_{6-n}(D_2O)_n]^{3+}$, underpinning the detrimental influence of a high number of high-energy NH and OH oscillators in very close proximity to the central ion on ES lifetimes.[174,175] These findings parallel the observation that radiative low-energy 4f-4f transitions of lanthanide(III) ions can be strongly quenched by the presence of coordinated water (O–H vibrations, free OH: 3600 cm^{-1}).[176]

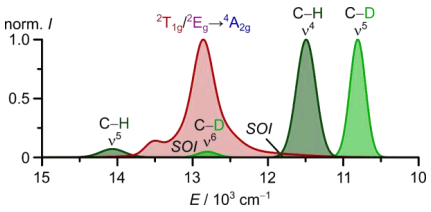

Fig. 23. Normalized C–H and C–D vibrational overtone spectra of model pyridine ligands (orange, green, blue) and qualitative indication of their spectral overlap integrals (SOIs) with the SF PL bands of $[Cr(ddpd)_2]^{3+}$.

The nonradiative decay of SF states, which are split by lower symmetry, via IRM can also be thermally activated. The splitting of SF states due to lower symmetry can reach a few hundred wavenumbers in polypyridine chromium(III) complexes and the SF lifetime is long enough to allow establishing a *Boltzmann* distribution between the lowest-energy SF states (vide supra).[22] Hence, at higher temperature, emission occurs from the two lowest SF states, while at lower temperature emission occurs only from the lowest-energy SF state. This change of PL band pattern has been shown to reduce the SOI and hence k_{nr} at lower temperature.[51] Similarly, spectral narrowing of the PL band of $[Cr(dgpy)_2]^{3+}$ [Scheme 1] at lower temperature in a frozen matrix reduces the SOI with C–H overtone bands and hence k_{nr}.[48]

V. CONCLUSION

This tutorial review comprehensively discussed the photophysics of molecular chromium(III) complexes in relation to solid chromium(III) materials such as ruby with an emphasis on the understanding of the unique photophysical properties of *Molecular Rubies*. The review covers fundamental theories for transition metal complexes, namely crystal field, ligand field and molecular orbital theory, the perturbational treatment of *Jahn-Teller* effects as well as vertical, horizontal and thermally activated processes and multiphonon relaxation that are relevant for the description and understanding of the photophysics and light-induced dynamics of chromium(III) complexes. Required physical concepts and mathematical relations and equations, such as ligand field term energies, selection rules, vibronic and spin-orbit coupling are introduced, explained and applied to the *Molecular Rubies*.

The high photoluminescence lifetime and quantum yield of the solid-state material ruby Al_2O_3:Cr^{3+} relies on the following key features: a) despite the weak oxido ligands, the interconfigurational $^4T_{2g}$ ligand field states are higher in energy than the nested $^2E_g/^2T_{1g}$ spin-flip states at the $^4A_{2g}$ ground state geometry thanks to a large ligand field splitting Δ_o in the small trigonally distorted octahedral void of the Al_2O_3 lattice; b) intersystem crossing from $^4T_{2g}$ to $^2E_g/^2T_{1g}$ states is fast and efficient; c) *Jahn-Teller* distortions cannot strongly stabilize the $^4T_{2g}$ states as the crystal lattice enforces a rigid environment, so that back-intersystem crossing from SF to $^4T_{2g}$ states is thermodynamically unfeasible; d) high-energy C–H, N–H or O–H oscillators are absent in the vicinity of the chromium(III) center so that multiphonon relaxation from spin-flip states to vibrational modes is impossible and e) the radiative rate constant $k_r = 210\ s^{-1}$ is comparably large due to the trigonal, non-centrosymmetric crystal environment.[3,5,6]

This review has discussed that *Molecular Ruby* $[Cr(ddpd)_2]^{3+}$ and its siblings feature similar features, but sometimes for different underlying reasons: a) strong pyridine donor ligands arranged to give a local close-to-octahedral $[CrN_6]$ coordination sphere gives a large ligand field splitting, so that $^4T_{2g}$ ligand field states are much higher in energy than the nested $^2E_g/^2T_{1g}$ spin-flip states at the $^4A_{2g}$ geometry (close to the $^4T_{2g}/^2T_{2g}$ crossing point in the *Tanabe-Sugano* diagram); b) intersystem crossing from $^4T_{2g}$ to $^2E_g/^2T_{1g}/^2T_{2g}$ states is efficient and fast at the *Franck-Condon* geometry with $k_{ISC} > 5.0\times10^{12}\ s^{-1}$; c) the quite rigid tridentate chelate ligands do not allow large-amplitude *Jahn-Teller* distortions (as compared to mono- and bidentate ligands), so that thermally activated back-intersystem crossing from spin-flip to $^4T_{2g}$ states is kinetically retarded; d) only four C–H oscillators are close to the chromium(III) center and their overtone energies (accidentally) do not match the photoluminescence energy, so that quite inefficient multiphonon relaxation results; e) thanks to the absence of a center of symmetry the radiative rate constant $k_r = 122\ s^{-1}$ [2,17,18] is large as compared to truly centrosymmetric complexes with $k_r < 1\ s^{-1}$ for $[Cr(CN)_6]^{3-}$ [177] or $k_r = 20\ s^{-1}$ $[Cr(tpe)_2]^{3+}$,[17,39,57] respectively.

In addition to the excellent photoluminescence properties of $[Cr(ddpd)_2]^{3+}$, its visible light absorption is boosted by productive LMCT states, so that a very high brightness B(436 nm) = $\Phi\,\varepsilon$(436 nm) = 516 $M^{-1}\,cm^{-1}$ results. These unique features of the *Molecular Rubies* and other chromium(III) complexes enable a multitude of applications, ranging from sensing,[7,22,35,36] lighting,[45,46] upconversion,[178] circularly polarized emission[46,55,58,88,95,96,134–136] to photocatalysis.[17,37–43,179–183]

Supplementary material

Appendix and details of the computational methods and Cartesian coordinates of all optimized geometries, including additional references.[184–218]

Acknowledgments

The authors would like to thank Phillip Sikora, Dr. Robert Naumann, Prof. Dr. Christian Reber and Prof. Dr. Gregor Diezemann for constructive criticism of the manuscript. They also thank Prof. Dr. Mihail Atanasov for resolving discrepancies between formulas used in refs. [111] and [117] and Dr. Jan Klett for providing the photographs of ruby. Parts of this article were conducted using the supercomputer Elwetritsch and advisory services offered by the University of Kaiserslautern-Landau (https://hpc.rz.rptu.de), which is a member of the AHRP. Financial support from the Deutsche Forschungsgemeinschaft [DFG, Priority Program SPP 2102 "Light-controlled reactivity of metal complexes", HE 2778/18-1] is gratefully acknowledged.

Conflict of Interest

The authors have no conflicts to disclose

Author contributions

C.F. performed all DFT and CASSCF calculations. C.F. and K.H. conceptualized the project and wrote the manuscript.

Data availability statement

The data that support the findings of this study are available in the main article and/or the supplementary material.

Ligand Abbreviations

acac$^-$	acetylacetonato(1−)
bpi$^-$	1,3-bis(pyridin-2-ylimino)isoindolinato(1−)
bpi$^{Me/H-}$	1,3-bis((4-methylpyridin-2-yl)imino)isoindolinato(1−)
bpi$^{Et/H-}$	1,3-bis((4-ethylpyridin-2-yl)imino)isoindolinato(1−)
bpi$^{OMe/H-}$	1,3-bis((4-methoxypyridin-2-yl)imino)isoindolinato(1−)
bpi$^{NMe2/H-}$	1,3-bis((4-(dimethylamino)pyridin-2-yl)imino)isoindolinato(1−)
bpi$^{H/OMe-}$	1,3-bis((5-methoxypyridin-2-yl)imino)isoindolinato(1−)
bpmp	2,6-bis(pyridin-2-ylmethyl)pyridine
bpop	2,6-bis(pyridin-2-yloxy)pyridine
bptp	2,6-bis(pyridin-2-ylthio)pyridine
bpy	2,2'-bipyridine
btmp	2,6-bis((4-phenyl-1H-1,2,3-triazol-1-yl)methyl)pyridine
ddpd	*N*^{2},*N*^{6}-dimethyl-*N*^{2},*N*^{6}-di(pyridin-2-yl)pyridine-2,6-diamine
ddpd^{Me}	*N*^{2},*N*^{6}-dimethyl-N^2,N^6-bis(5-methylpyridin-2-yl)pyridine-2,6-diamine
ddpd^{Mes}	*N*^{2},*N*^{6}-dimethyl-N^2,N^6-bis(5-mesitylpyridin-2-yl)pyridine-2,6-diamine
ddpd^{Tripp}	*N*^{2},*N*^{6}-dimethyl-N^2,N^6-bis(5-(2,4,6-triisopopylphenyl)pyridin-2-yl)pyridine-2,6-diamine
dgpy	2,6-diguanidylpyridine
dpc$^-$	3,6-di-*tert*-butyl-1,8-di(pyridin-2-yl)-carbazolato(1−)
dqp	2,6-di(quinolin-8-yl)pyridine
dqp^{Br}	8,8'-(4-bromopyridine-2,6-diyl)diquinoline
dqp$^{C\equiv CH}$	8,8'-(4-ethynylpyridine-2,6-diyl)diquinoline
dqp^{OMe}	8,8'-(4-methoxypyridine-2,6-diyl)diquinoline
en	ethylenediamine
H_2tpda	*N*^{2},*N*^{6}-di(pyridin-2-yl)pyridine-2,6-diamine
Mebipzp	2,6-bis((3,5-dimethyl-1H-pyrazol-1-yl)methyl)pyridine
IMebipzp	2,6-bis((4-iodo-3,5-dimethyl-1H-pyrazol-1-yl)methyl)pyridine
phen	1,10-phenanthroline
py	pyridine
tpe	2,2',2''-(ethane-1,1,1-triyl)tripyridine
tpy	2,2':6',2''-terpyridine

References

[1]J. Lewis, D. Schwarzenbach, and H. D. Flack, Acta Crystallogr., Sect. A **38**, 733 (1982).
[2]S. Otto, M. Grabolle, C. Förster, C. Kreitner, U. Resch-Genger, and K. Heinze, Angew. Chem. Int. Ed. **54**, 11572 (2015).
[3]T. H. Maiman, Nature **187**, 493 (1960).
[4]D. F. Nelson and M. D. Sturge, Phys. Rev. **137**, A1117-A1130 (1965).
[5]R. S. Quimby and W. M. Yen, J. Appl. Phys. **51**, 1780 (1980).
[6]C. Degli Esposti and L. Bizzocchi, J. Chem. Educ. **84**, 1316 (2007).
[7]S. Otto, J. P. Harris, K. Heinze, and C. Reber, Angew. Chem. Int. Ed. Engl. **57**, 11069 (2018).
[8]P. W. Atkins and R. Friedman, *Molecular quantum mechanics*, 5th ed. (Oxford Univ. Press, Oxford, 2011).
[9]V. Balzani, G. Bergamini, S. Campagna, and F. Puntoriero in *Photochemistry and Photophysics of Coordination Compounds I*, edited by V. Balzani and S. Campagna (Springer, Berlin, Heidelberg, 2007), Vol. 280, p. 1.
[10]V. Balzani, P. Ceroni, and A. Juris, *Photochemistry and Photophysics*. *Concepts, Research, Applications*, 2nd ed. (Wiley-VCH, Weinheim, 2024).
[11]P. S. Wagenknecht and P. C. Ford, Coord. Chem. Rev. **255**, 591 (2011).
[12]N. A. P. Kane-Maguire in *Photochemistry and Photophysics of Coordination Compounds I*, edited by V. Balzani and S. Campagna (Springer, Berlin, Heidelberg, 2007), Vol. 280, p. 37.
[13]L. S. Forster, Coord. Chem. Rev. **227**, 59 (2002).
[14]A. D. Kirk, Chem. Rev. **99**, 1607 (1999).
[15]L. S. Forster, Chem. Rev. **90**, 331 (1990).
[16]W. R. Kitzmann, J. Moll, and K. Heinze, Photochem. Photobiol. Sci. **21**, 1309 (2022).
[17]S. Sittel, R. Naumann, and K. Heinze, Front. Chem. **10**, 887439 (2022).
[18]C. Wang, W. R. Kitzmann, F. Weigert, C. Förster, X. Wang, K. Heinze, and U. Resch-Genger, ChemPhotoChem **6**, e202100296 (2022).
[19]S. Otto, M. Dorn, C. Förster, M. Bauer, M. Seitz, and K. Heinze, Coord. Chem. Rev. **359**, 102 (2018).
[20]C. Wang, S. Otto, M. Dorn, E. Kreidt, J. Lebon, L. Sršan, P. Di Martino-Fumo, M. Gerhards, U. Resch-Genger, M. Seitz, and K. Heinze, Angew. Chem. Int. Ed. **57**, 1112 (2018).
[21]W. R. Kitzmann, C. Ramanan, R. Naumann, and K. Heinze, Dalton Trans. **51**, 6519 (2022).
[22]S. Otto, N. Scholz, T. Behnke, U. Resch-Genger, and K. Heinze, Chemistry **23**, 12131 (2017).
[23]T.-H. Huang, C.-C. Hsu, C.-T. Kuo, P. Lu, W.-S. Tse, D. P. Wang, T. C. Chou, and A. Y. G. Fuh, J. Appl. Phys. **75**, 3599 (1994).
[24]R. A. Forman, G. J. Piermarini, J. D. Barnett, and S. Block, Science **176**, 284 (1972).
[25]G. J. Piermarini, S. Block, J. D. Barnett, and R. A. Forman, J. Appl. Phys. **46**, 2774 (1975).
[26]H. K. Mao, P. M. Bell, J. W. Shaner, and D. J. Steinberg, J. Appl. Phys. **49**, 3276 (1978).
[27]R. G. Munro, G. J. Piermarini, S. Block, and W. B. Holzapfel, J. Appl. Phys. **57**, 165 (1985).
[28]C. Förster and K. Heinze in *Advances in Inorganic Chemistry*. *Photochemistry and Photophysics of Earth-Abundant Transition Metal Complexes*, edited by R. van Eldik (Elsevier Science & Technology, San Diego, 2024), Vol. 83, p. 111.
[29]C. Förster and K. Heinze, Chem. Soc. Rev. **49**, 1057 (2020).
[30]M. Dorn, N. R. East, C. Förster, W. R. Kitzmann, J. Moll, F. Reichenauer, T. Reuter, L. Stein, and K. Heinze in *Comprehensive inorganic chemistry III*, edited by J. Reedijk and K. R. Poeppelmeier (Elsevier, Amsterdam, Boston, Heidelberg, London, New York, 2023), p. 707.
[31]C. Förster and K. Heinze, Chem. Phys. Rev. **3**, 41302 (2022).
[32]J.-R. Jiménez, B. Doistau, M. Poncet, and C. Piguet, Coord. Chem. Rev. **434**, 213750 (2021).
[33]P. A. Scattergood in *Organometallic Chemistry*, edited by N. J. Patmore and P. I. P. Elliott (Royal Society of Chemistry, Cambridge, 2020), Vol. 43, p. 1.
[34]L. A. Büldt and O. S. Wenger, Chem. Sci. **8**, 7359 (2017).
[35]C. Wang, S. Otto, M. Dorn, K. Heinze, and U. Resch-Genger, Anal. Chem. **91**, 2337 (2019).
[36]C. Förster, H. Osthues, D. Schwab, N. L. Doltsinis, and K. Heinze, ChemPhysChem **24**, e202300165 (2023).
[37]Z. Shen and J.-L. Tu, Eur. J. Org. Chem. **28**, e202401016 (2025).
[38]G. Morselli, T. H. Eggenweiler, M. Villa, A. Prescimone, and O. S. Wenger, J. Am. Chem. Soc. **147**, 28226 (2025).
[39]S. Sittel, J. Neuner, J. M. Grenz, C. Förster, R. Naumann, and K. Heinze, Adv. Synth. Catal. **367**, e202500075 (2025).
[40]T. H. Bürgin, F. Glaser, and O. S. Wenger, J. Am. Chem. Soc. **144**, 14181 (2022).
[41]C. Wang, H. Li, T. H. Bürgin, and O. S. Wenger, Nat. Chem. **16**, 1151 (2024).
[42]S. Sittel, A. C. Sell, K. Hofmann, C. Wiedemann, J. P. Nau, C. Kerzig, G. Manolikakes, and K. Heinze, ChemCatChem **15**, e202201562 (2023).
[43]S. Otto, A. M. Nauth, E. Ermilov, N. Scholz, A. Friedrich, U. Resch-Genger, S. Lochbrunner, T. Opatz, and K. Heinze, ChemPhotoChem **1**, 344 (2017).
[44]C. Wang, F. Reichenauer, W. R. Kitzmann, C. Kerzig, K. Heinze, and U. Resch-Genger, Angew. Chem. Int. Ed. **61**, e202202238 (2022).
[45]W.-Y. Huang, E. Meßmer, S.-M. Ho, Y.-R. Li, C.-W. Lu, K. Heinze, and H.-C. Su, J. Mater. Chem. C, accepted (2026).
[46]M. Poncet, J.-R. Jiménez, F. Zinna, C. Piguet, L. Di Bari, C. Botta, and U. Giovanella, Small, e12638 (2025).
[47]S. Sittel, D. Zorn, A. König, J. M. Grenz, C. Förster, R. Naumann, and K. Heinze, Chemistry, e02668 (2025).
[48]S. Sittel, R. Naumann, C. Förster, M. E. Huber, J. Meyer, and K. Heinze, Inorg. Chem. **64**, 20404 (2025).
[49]J. Sander, F. Gauder, S. J. Schicktanz, T. Maulbetsch, J. Kalmbach, D. Zorn, R. Naumann, C. Förster, D. Kunz, and K. Heinze, Z. Anorg. Allg. Chem. **651** (2025).
[50]F. Reichenauer, D. Zorn, R. Naumann, C. Förster, and K. Heinze, Inorg. Chem. **63**, 23487 (2024).

[51]F. Reichenauer, R. Naumann, C. Förster, W. R. Kitzmann, A.-P. M. Reponen, S. Feldmann, and K. Heinze, Chem. Sci. **15**, 20251 (2024).
[52]L. Stein, C. Wang, C. Förster, U. Resch-Genger, and K. Heinze, Dalton Trans. **51**, 17664 (2022).
[53]F. Reichenauer, C. Wang, C. Förster, P. Boden, N. Ugur, R. Báez-Cruz, J. Kalmbach, L. M. Carrella, E. Rentschler, C. Ramanan, G. Niedner-Schatteburg, M. Gerhards, M. Seitz, U. Resch-Genger, and K. Heinze, J. Am. Chem. Soc. **143**, 11843 (2021).
[54]N. Sinha, J.-R. Jiménez, B. Pfund, A. Prescimone, C. Piguet, and O. S. Wenger, Angew. Chem. Int. Ed. Engl. **60**, 23722 (2021).
[55]J.-R. Jiménez, M. Poncet, S. Míguez-Lago, S. Grass, J. Lacour, C. Besnard, J. M. Cuerva, A. G. Campaña, and C. Piguet, Angew. Chem. Int. Ed. Engl. **60**, 10095 (2021).
[56]J.-R. Jiménez, M. Poncet, B. Doistau, C. Besnard, and C. Piguet, Dalton Trans. **49**, 13528 (2020).
[57]S. Treiling, C. Wang, C. Förster, F. Reichenauer, J. Kalmbach, P. Boden, J. P. Harris, L. M. Carrella, E. Rentschler, U. Resch-Genger, C. Reber, M. Seitz, M. Gerhards, and K. Heinze, Angew. Chem. Int. Ed. Engl. **58**, 18075 (2019).
[58]J.-R. Jiménez, B. Doistau, C. M. Cruz, C. Besnard, J. M. Cuerva, A. G. Campaña, and C. Piguet, J. Am. Chem. Soc. **141**, 13244 (2019).
[59]I. Widmann, G. Kinik, M. Jähnig, R. Glaum, M. Schwarz, C. Wüstefeld, D. Johrendt, M. Tribus, C. Hejny, L. Bayarjargal, L. Dubrovinsky, G. Heymann, M. Suta, and H. Huppertz, Adv. Funct. Mater. **34** (2024).
[60]B. N. Figgis and M. A. Hitchman, *Ligand field theory and its applications*, 1st ed. (Wiley-VCH, New York, N.Y., Chichester, 2000).
[61]A. B. P. Lever, *Inorganic Electronic Spectroscopy*, 2nd ed. (Elsevier, Amsterdam, 1984).
[62]H. L. Schläfer and G. Gliemann, *Einführung in die Ligandenfeldtheorie*, 2nd ed. (Akad. Verl.-Ges, Wiesbaden, 1980).
[63]C. J. Ballhausen, *Introduction to ligand field theory*, 1st ed. (McGraw-Hill, New York, NY u.a., 1962).
[64]A. L. Odom, R. Beaulac, and A. R. Johnson, *Inorganic chemistry*. *An integrated approach*, 1st ed. (Oxford University Press, Oxford, UK, New York, NY, 2026).
[65]J. E. Huheey, E. A. Keiter, and R. L. Keiter, *Anorganische Chemie*. *Prinzipien von Struktur und Reaktivität*, 5th ed. (De Gruyter, 2014).
[66]L. H. Gade, *Koordinationschemie*, 1st ed. (Wiley-VCH, Weinheim, 2010).
[67]D. F. a. A. P. W. Shriver, *Inorganic Chemistry*, 5th ed. (Oxford Univ. Press, Oxford University Press, 2009).
[68]Y. Tanabe and S. Sugano, J. Phys. Soc. Jpn. **9**, 766 (1954).
[69]Y. Tanabe and S. Sugano, J. Phys. Soc. Jpn. **9**, 753 (1954).
[70]R. D. Shannon, Acta Cryst A **32**, 751 (1976).
[71]M. G. Brik, N. M. Avram, and C. N. Avram, Solid State Commun. **132**, 831 (2004).
[72]M. G. Brik, N. M. Avram, and C. N. Avram, Solid State Commun. **134**, 233 (2005).
[73]H. Yersin, P. Huber, G. Gietl, and D. Trümbach, Chem. Phys. Lett. **199**, 1 (1992).
[74]M. Kaupp, J. Comput. Chem. **28**, 320 (2007).
[75]P. Pyykkö, Chem. Rev. **88**, 563 (1988).
[76]C. K. Jørgensen in *Progress in Inorganic Chemistry*, edited by F. A. Cotton (Wiley, 1962), Vol. 4, p. 73.
[77]C. K. Jørgensen in *Advances in Chemical Physics*, edited by I. Prigogine (Wiley, 1963), Vol. 5, p. 33.
[78]L. G. Vanquickenborne, L. Haspeslagh, M. Hendrickx, and J. Verhulst, Inorg. Chem. **23**, 1677 (1984).
[79]K.-W. Lee and P. E. Hoggard, Chem. Phys. **135**, 219 (1989).
[80]J.-R. Jiménez, B. Doistau, C. Besnard, and C. Piguet, Chem. Commun. **54**, 13228 (2018).
[81]S. Lenz, H. Bamberger, P. P. Hallmen, Y. Thiebes, S. Otto, K. Heinze, and J. van Slageren, Phys. Chem. Chem. Phys. **21**, 6976 (2019).
[82]R. Stranger, G. Moran, E. Krausz, H. Güdel, and N. Furer, Mol. Phys. **69**, 11 (1990).
[83]H.-H. Schmidtke in *Optical spectra and chemical bonding in inorganic compounds*, edited by D. M. P. Mingos, T. Schönherr, and N. Amstutz (Springer, Berlin, 2004), Vol. 106, p. 19.
[84]C. Förster, M. Dorn, T. Reuter, S. Otto, G. Davarci, T. Reich, L. Carrella, E. Rentschler, and K. Heinze, Inorganics **6**, 86 (2018).
[85]C. C. Scarborough, K. M. Lancaster, S. DeBeer, T. Weyhermüller, S. Sproules, and K. Wieghardt, Inorg. Chem. **51**, 3718 (2012).
[86]E. C. Constable, C. E. Housecroft, M. Neuburger, J. Schönle, and J. A. Zampese, Dalton Trans. **43**, 7227 (2014).
[87]M. O. J. Y. Hunault, Y. Harada, J. Miyawaki, J. Wang, A. Meijerink, F. M. F. de Groot, and M. M. van Schooneveld, J. Phys. Chem. A. **122**, 4399 (2018).
[88]A. Gabbani, M. Poncet, G. Pescitelli, L. Carbonaro, J. Krzystek, E. Colacio, C. Piguet, F. Pineider, L. Di Bari, J.-R. Jiménez, and F. Zinna, Chem. Sci. **15**, 17217 (2024).
[89]P. J. Stephens in *Advances in Chemical Physics*, edited by I. Prigogine and S. A. Rice (Wiley, 1976), Vol. 35, p. 197.
[90]L. J. P. Ament, M. van Veenendaal, T. P. Devereaux, J. P. Hill, and J. van den Brink, Rev. Mod. Phys. **83**, 705 (2011).
[91]B. O. Roos, *Multiconfigurational Quantum Chemistry*, 1st ed. (Wiley, Somerset, 2016).
[92]S. K. Singh, J. Eng, M. Atanasov, and F. Neese, Coord. Chem. Rev. **344**, 2 (2017).
[93]M. Atanasov, D. Ganyushin, K. Sivalingam, and F. Neese in *Molecular Electronic Structures of Transition Metal Complexes II*, edited by D. M. P. Mingos, P. Day, and J. P. Dahl (Springer Berlin Heidelberg, Berlin, Heidelberg, 2012), Vol. 143, p. 149.
[94]V. Veryazov, P. Å. Malmqvist, and B. O. Roos, Int. J. Quantum Chem. **111**, 3329 (2011).
[95]M. Poncet, C. Besnard, L. Guénée, J.-R. Jiménez, and C. Piguet, Front. Chem. **12**, 1472943 (2024).
[96]M. Poncet, L. Cuevas-Contreras, Y. Ye, L. Guénée, C. M. Cruz, C. Piguet, and J.-R. Jiménez, J. Am. Chem. Soc. **147**, 23827 (2025).
[97]R. N. Perutz, O. Torres, and A. Vlček in *Comprehensive inorganic chemistry II*. *From elements to applications*, edited by J. Reedijk and K. R. Poeppelmeier (Elsevier, Amsterdam, 2013), p. 229.

[98]F. Puntoriero, F. Nastasi, M. Galletta, and S. Campagna in *Comprehensive inorganic chemistry II*. *From elements to applications*, edited by J. Reedijk and K. R. Poeppelmeier (Elsevier, Amsterdam, 2013), p. 255.
[99]D. Zare, B. Doistau, H. Nozary, C. Besnard, L. Guénée, Y. Suffren, A.-L. Pelé, A. Hauser, and C. Piguet, Dalton Trans. **46**, 8992 (2017).
[100]M. Dorn, D. Hunger, C. Förster, R. Naumann, J. van Slageren, and K. Heinze, Chemistry **29**, e202202898 (2023).
[101]W. R. Kitzmann, D. Hunger, A.-P. M. Reponen, C. Förster, R. Schoch, M. Bauer, S. Feldmann, J. van Slageren, and K. Heinze, Inorg. Chem. **62**, 15797 (2023).
[102]N. R. East, C. Förster, L. M. Carrella, E. Rentschler, and K. Heinze, Inorg. Chem. **61**, 14616 (2022).
[103]N. R. East, R. Naumann, C. Förster, C. Ramanan, G. Diezemann, and K. Heinze, Nat. Chem. **16**, 827 (2024).
[104]Proc. R. Soc. Lond. A **161**, 220 (1937).
[105]I. B. Bersuker, Chem. Rev. **121**, 1463 (2021).
[106]I. B. Bersuker, *The Jahn-Teller effect*, 1st ed. (Cambridge University Press, Cambridge, 2010).
[107]I. B. Bersuker, Chem. Rev. **101**, 1067 (2001).
[108]G. Franz, *Quantenphysik*. *Quantenmechanik*, 1st ed. (Walter de Gruyter GmbH, Basel/Berlin/Boston, 2024).
[109]J. Reinhold, *Quantentheorie der Moleküle*. *Eine Einführung*, 5th ed. (Springer Spektrum, Wiesbaden, 2015).
[110]N. Zettili, *Quantum mechanics*. *Concepts and applications*, 3rd ed. (Wiley, Hoboken, NJ, Chichester, West Sussex, 2022).
[111]D. Reinen, M. Atanasov, P. Köhler, and D. Babel, Coord. Chem. Rev. **254**, 2703 (2010).
[112]M. A. Halcrow, Chem. Soc. Rev. **42**, 1784 (2013).
[113]A. Thangavel, M. Wieliczko, C. Scarborough, B. Dittrich, and J. Bacsa, Acta Crystallogr., Sect. C **71**, 936 (2015).
[114]P. M. Becker, C. Förster, L. M. Carrella, P. Boden, D. Hunger, J. van Slageren, M. Gerhards, E. Rentschler, and K. Heinze, Chem. Eur. J. **26**, 7199 (2020).
[115]D. J. Tannor, *Introduction to quantum mechanics*. *A time-dependent perspective*, 1st ed. (University Science Books, Sausalito, Calif., 2007).
[116]H. J. Kupka, *Transitions in Molecular Systems*, 1st ed. (John Wiley & Sons Incorporated, Hoboken, 2011).
[117]R. B. Wilson and E. I. Solomon, Inorg. Chem. **17**, 1729 (1978).
[118]H. U. Guedel and T. R. Snellgrove, Inorg. Chem. **17**, 1617 (1978).
[119]R. Knochenmuss, C. Reber, M. V. Rajasekharan, and H. U. Güdel, J. Chem. Phys. **85**, 4280 (1986).
[120]O. S. Wenger and H. U. Güdel, J. Chem. Phys. **114**, 5832 (2001).
[121]O. S. Wenger, R. Valiente, and H. U. Güdel, J. Chem. Phys. **115**, 3819 (2001).
[122]A. Ceulemans, D. Beyens, and L. G. Vanquickenborne, J. Am. Chem. Soc. **104**, 2988 (1982).
[123]H. Haken, *Molecular Physics and Elements of Quantum Chemistry*. *Introduction to Experiments and Theory*, 2nd ed. (Springer, Berlin, Heidelberg, 2004).
[124]B. Valeur and M. N. Berberan-Santos, *Molecular fluorescence*. *Principles and applications*, 2nd ed. (Wiley-VCH, Weinheim, 2012).
[125]J. R. Lakowicz, *Principles of Fluorescence Spectroscopy*, 3rd ed. (Springer US, Boston, MA, 2006).
[126]R. C. Hilborn, Am. J. Phys. **50**, 982 (1982).
[127]R. C. Hilborn, Am. J. Phys. **51**, 471 (1983).
[128]R. Berera, R. van Grondelle, and J. T. M. Kennis, Photosynth. Res. **101**, 105 (2009).
[129]U. Resch-Genger and K. Rurack, Pure Appl. Chem. **85**, 2005 (2013).
[130]A. M. Brouwer, Pure Appl. Chem. **83**, 2213 (2011).
[131]U. Resch-Genger and P. C. DeRose, Pure Appl. Chem. **82**, 2315 (2010).
[132]D. M. Arias-Rotondo and J. K. McCusker, Chem. Soc. Rev. **45**, 5803 (2016).
[133]W. Demtröder, *Atoms, Molecules and Photons*. *An Introduction to Atomic-, Molecular- and Quantum Physics*, 3rd ed. (Springer, Berlin, 2018).
[134]C. Dee, F. Zinna, W. R. Kitzmann, G. Pescitelli, K. Heinze, L. Di Bari, and M. Seitz, Chem. Commun. **55**, 13078 (2019).
[135]M. Poncet, A. Benchohra, J.-R. Jiménez, and C. Piguet, ChemPhotoChem **5**, 880 (2021).
[136]J.-R. Jiménez, S. Míguez-Lago, M. Poncet, Y. Ye, C. L. Ruiz, C. M. Cruz, A. G. Campaña, E. Colacio, C. Piguet, and J. M. Herrera, J. Mater. Chem. C **11**, 2582 (2023).
[137]N. S. Hush in *Progress in Inorganic Chemistry*, edited by F. A. Cotton (Wiley, 1967), Vol. 8, p. 391.
[138]N. S. Hush, Coord. Chem. Rev. **64**, 135 (1985).
[139]R. A. Marcus and N. Sutin, Biochem. Biophys. Acta, Bioenerg. **811**, 265 (1985).
[140]R. A. Marcus, Angew. Chem. Int. Ed. Engl. **32**, 1111 (1993).
[141]E. J. Piechota and G. J. Meyer, J. Chem. Educ. **96**, 2450 (2019).
[142]S. J. Strickler and R. A. Berg, J. Chem. Phys. **37**, 814 (1962).
[143]B. de Souza, F. Neese, and R. Izsák, J. Chem. Phys. **148**, 34104 (2018).
[144]G. Baryshnikov, B. Minaev, and H. Ågren, Chem. Rev. **117**, 6500 (2017).
[145]B. Minaev, G. Baryshnikov, and H. Agren, Phys. Chem. Chem. Phys. **16**, 1719 (2014).
[146]S.-N. Chen and G. B. Porter, J. Am. Chem. Soc. **92**, 2189 (1970).
[147]X. Zheng, M. C. Drummer, T. A. Russell, S. Gozem, and K. D. Glusac, J. Chem. Educ. (2024).
[148]C. M. Marian, Annu. Rev. Phys. Chem. **72**, 617 (2021).
[149]T. J. Penfold, E. Gindensperger, C. Daniel, and C. M. Marian, Chem. Rev. **118**, 6975 (2018).
[150]C. M. Marian, WIREs Comput. Mol. Sci. **2**, 187 (2012).
[151]R. Englman and J. Jortner, Mol. Phys. **18**, 145 (1970).
[152]E. Kreidt, C. Kruck, and M. Seitz in *Handbook on the physics and chemistry of rare earths*. *Including actinides*, edited by J.-C. G. Bünzli, V. K. Pecharsky, G.-Y. Adachi, K. A. Gschneidner, and E. LeRoy (NH North-Holland an imprint of Elsevier, Amsterdam, Oxford, 2018), Vol. 53, p. 35.
[153]B. Champagnon, E. Duval, A. Monteil, and R. Englman, Physics Letters A **93**, 241 (1983).
[154]R. Englman, B. Champagnon, E. Duval, and A. Monteil, J. Lumin. **28**, 337 (1983).

[155]M. Suta and A. Meijerink, Adv. Theory Simul. **3** (2020).
[156]G. Kinik, I. Widmann, B. Bendel, H. Huppertz, A. Meijerink, and M. Suta, Light, science & applications **14**, 388 (2025).
[157]M. C. Carey, S. L. Adelman, and J. K. McCusker, Chem. Sci. **10**, 134 (2019).
[158]T. Reuter, D. Zorn, R. Naumann, J. Klett, C. Förster, and K. Heinze, Angew. Chem. Int. Ed. Engl. **63**, e202406438 (2024).
[159]E. M. Kober, J. V. Caspar, R. S. Lumpkin, and T. J. Meyer, J. Phys. Chem. **90**, 3722 (1986).
[160]Y. Cheng, Q. Yang, J. He, W. Zou, K. Liao, X. Chang, C. Zou, and W. Lu, Dalton Trans. **52**, 2561 (2023).
[161]N. Sawicka, C. J. Craze, P. N. Horton, S. J. Coles, E. Richards, and S. J. A. Pope, Chem. Commun. **58**, 5733 (2022).
[162]S. Otto, C. Förster, C. Wang, U. Resch-Genger, and K. Heinze, Chemistry **24**, 12555 (2018).
[163]M. A. El-Sayed, J. Chem. Phys. **38**, 2834 (1963).
[164]P. Pokhilko, E. Epifanovsky, and A. I. Krylov, J. Chem. Phys. **151**, 34106 (2019).
[165]W. A. Runciman, K. A. Schroeder, Proc. R. Soc. Lond. A **265**, 489 (1962).
[166]J. S. Griffith, Trans. Faraday Soc. **56**, 193 (1960).
[167]E. A. Juban and J. K. McCusker, J. Am. Chem. Soc. **127**, 6857 (2005).
[168]H. Ando, S. Iuchi, and H. Sato, Chem. Phys. Lett. **535**, 177 (2012).
[169]R. W. Jones, A. J. Auty, G. Wu, P. Persson, M. V. Appleby, D. Chekulaev, C. R. Rice, J. A. Weinstein, P. I. P. Elliott, and P. A. Scattergood, J. Am. Chem. Soc. **145**, 12081 (2023).
[170]Y. Ye, M. Poncet, P. Yaltseva, P. Salcedo-Abraira, A. Rodríguez-Diéguez, J. H. Martín, L. Cuevas-Contreras, C. M. Cruz, B. Doistau, C. Piguet, O. S. Wenger, J. M. Herrera, and J.-R. Jiménez, Chem. Sci. **16**, 5205 (2025).
[171]V. L. Ermolaev and E. B. Sveshnikova, Russ. Chem. Rev. **63**, 905 (1994).
[172]V. L. Ermolaev and E. B. Sveshnikova, J. Lumin. **20**, 387 (1979).
[173]T. Förster, Ann. Phys. (Berlin, Ger.) **437**, 55 (1948).
[174]A. Ditze and F. Wasgestian, Ber. Bunsenges. Phys. Chem. **90**, 111 (1986).
[175]M. Mvele and F. Wasgestian, Inorg. Chim. Acta **119**, 25 (1986).
[176]J.-C. G. Bünzli and S. V. Eliseeva in *Lanthanide Luminescence*, edited by P. Hänninen and H. Härmä (Springer Berlin Heidelberg, Berlin, Heidelberg, 2011), Vol. 7, p. 1.
[177]A. D. Kirk and G. B. Porter, J. Phys. Chem. **84**, 887 (1980).
[178]J. Kalmbach, C. Wang, Y. You, C. Förster, H. Schubert, K. Heinze, U. Resch-Genger, and M. Seitz, Angew. Chem. Int. Ed. **59**, 18804 (2020).
[179]S. M. Stevenson, M. P. Shores, and E. M. Ferreira, Angew. Chem. Int. Ed. **54**, 6506 (2015).
[180]R. F. Higgins, S. M. Fatur, S. G. Shepard, S. M. Stevenson, D. J. Boston, E. M. Ferreira, N. H. Damrauer, A. K. Rappé, and M. P. Shores, J. Am. Chem. Soc. **138**, 5451 (2016).
[181]S. M. Stevenson, R. F. Higgins, M. P. Shores, and E. M. Ferreira, Chem. Sci. **8**, 654 (2017).
[182]R. F. Higgins, S. M. Fatur, N. H. Damrauer, E. M. Ferreira, A. K. Rappé, and M. P. Shores, ACS Catal. **8**, 9216 (2018).
[183]F. J. Sarabia, Q. Li, and E. M. Ferreira, Angew. Chem. Int. Ed. Engl. **57**, 11015 (2018).
[184]F. Neese, WIREs Comput. Mol. Sci. **12**, e1606 (2022).
[185]F. Neese, WIREs Comput. Mol. Sci. **2**, 73 (2012).
[186]A. D. Becke, J. Chem. Phys. **98**, 5648 (1993).
[187]C. Lee, W. Yang, and R. G. Parr, Phys. Rev. B **37**, 785 (1988).
[188]B. Miehlich, A. Savin, H. Stoll, and H. Preuss, Chem. Phys. Lett. **157**, 200 (1989).
[189]D. A. Pantazis, X.-Y. Chen, C. R. Landis, and F. Neese, J. Chem. Theory Comput. **4**, 908 (2008).
[190]D. A. Pantazis and F. Neese, J. Chem. Theory Comput. **5**, 2229 (2009).
[191]F. Weigend and R. Ahlrichs, Phys. Chem. Chem. Phys. **7**, 3297 (2005).
[192]D. A. Pantazis and F. Neese, Theor. Chem. Acc. **131**, 1292 (2012).
[193]D. A. Pantazis and F. Neese, J. Chem. Theory Comput. **7**, 677 (2011).
[194]J. D. Rolfes, F. Neese, and D. A. Pantazis, J. Comput. Chem. **41**, 1842 (2020).
[195]F. Weigend, Phys. Chem. Chem. Phys. **8**, 1057 (2006).
[196]E. van Lenthe, E. J. Baerends, and J. G. Snijders, J. Chem. Phys. **99**, 4597 (1993).
[197]C. van Wüllen, J. Chem. Phys. **109**, 392 (1998).
[198]F. Neese, J. Comput. Chem. **24**, 1740 (2003).
[199]F. Neese, F. Wennmohs, A. Hansen, and U. Becker, Chem. Phys. **356**, 98 (2009).
[200]R. Izsák and F. Neese, J. Chem. Phys. **135**, 144105 (2011).
[201]B. Helmich-Paris, B. de Souza, F. Neese, and R. Izsák, J. Chem. Phys. **155**, 104109 (2021).
[202]S. Miertuš, E. Scrocco, and J. Tomasi, Chem. Phys. **55**, 117 (1981).
[203]V. Barone and M. Cossi, J. Phys. Chem. A **102**, 1995 (1998).
[204]S. Grimme, J. Antony, S. Ehrlich, and H. Krieg, J. Chem. Phys. **132**, 154104 (2010).
[205]S. Grimme, S. Ehrlich, and L. Goerigk, J. Comput. Chem. **32**, 1456 (2011).
[206]F. Plasser, J. Chem. Phys. **152**, 84108 (2020).
[207]G. L. Stoychev, A. A. Auer, and F. Neese, J. Chem. Theory Comput. **13**, 554 (2017).
[208]C. Angeli, R. Cimiraglia, S. Evangelisti, T. Leininger, and J.-P. Malrieu, J. Chem. Phys. **114**, 10252 (2001).
[209]C. Angeli, R. Cimiraglia, and J.-P. Malrieu, J. Chem. Phys. **117**, 9138 (2002).
[210]L. Lang and F. Neese, J. Chem. Phys. **150**, 104104 (2019).
[211]Y. Guo, K. Sivalingam, and F. Neese, J. Chem. Phys. **154**, 214111 (2021).
[212]C. Kollmar, K. Sivalingam, Y. Guo, and F. Neese, J. Chem. Phys. **155**, 234104 (2021).
[213]B. A. Heß, C. M. Marian, U. Wahlgren, and O. Gropen, Chem. Phys. Lett. **251**, 365 (1996).
[214]F. Neese, J. Chem. Phys. **122**, 34107 (2005).
[215]D. Ganyushin and F. Neese, J. Chem. Phys. **128**, 114117 (2008).
[216]A. M. McDaniel, H.-W. Tseng, N. H. Damrauer, and M. P. Shores, Inorg. Chem. **49**, 7981 (2010).

[217]J. C. Barbour, A. J. I. Kim, E. deVries, S. E. Shaner, and B. M. Lovaasen, Inorg. Chem. **56**, 8212 (2017).
[218]I. B. Bersuker, Chem. Rev. **113**, 1351 (2013).